University of Nevada, Reno

Applications and examination of techniques used to determine magma storage and ascent timescales in arc volcanoes

A dissertation submitted in partial fulfillment of the requirements for the degree of

Doctor of Philosophy in Geology

by

Ellyn G. Huggins

Dr. Philipp Ruprecht/Dissertation Advisor

December, 2023

Copyright by Ellyn G. Huggins 2023

THE GRADUATE SCHOOL

We recommend that the dissertation
prepared under our supervision by

entitled

be accepted in partial fulfillment of the
requirements for the degree of

Advisor

Committee Member

Committee Member

Committee Member

Graduate School Representative

Markus Kemmelmeier, Ph.D., Dean
Graduate School

ABSTRACT

Magmatic volatile elements and compounds in magmas (i.e., H_2O, CO_2, S, F, and Cl) are linked to the processes that control magma storage and decompression during an eruption. Because of their pressure dependent solubilities, measurements of volatile concentrations in melt can be used to infer storage conditions of the magma. In addition, the fractionation and exsolution of these volatiles during magma decompression have a direct influence on the transportation of magma and explosivity of an eruption. Using crystal-scale analyses and thermodynamic models, I explore how pre-eruptive volatile contents affect the evolution of crystal cargo and how volatile exsolution drives eruption dynamics as recorded in the eruptive history. In the first chapter, I explore thermodynamic drivers of disequilibrium dissolution and growth of plagioclase microlites during ascent by modeling the chemical affinity (the degree of disequilibrium) between plagioclase at set compositions and an evolving silicate melt due to ascent driven exsolution of H_2O. The lack of microlites in volcanic samples is often suggested to form due to kinetic limitations of microlite growth during fast magmatic ascent; however, many magmatic systems are disrupted thermally prior to eruption. Such systems may also lack extensive microlite crystallization. Through this work, I show that reheating and ascent significantly reduces any kinetic limitation on microlite formation and that microlite-free eruptions do not require the fast ascent rates imposed by kinetics alone. Next, I leverage olivine hosted melt inclusions (MI) from the 2018 eruption

at Mount Veniaminof, Alaska, to unravel the storage history preceding the eruption. Volatile measurements correspond to minimum entrapment pressures of 400 MPa and entrapment depths <15 km. Our estimates of magma storage depths are supported by relatively deep precursory long period earthquakes (16-20 km). In the third chapter, I examine a chronometer for magma ascent based on measurements of volatile gradients in melt embayments (ME), open pockets of melt that remain in contact with the host magma. Past uses of this methodology have been restricted to small (<10) sample sizes because of the rigid requirements for diffusion modeling (i.e., simple, 1-D geometry). Not accounting for more complicated geometry can lead to under or overestimates of magma ascent rates. I perform an in-depth analysis of textures of melt embayments from the 2018 eruption via 3-D volumes derived from micro-computed tomography data to expand the usage of melt embayments to non-conventional samples.

ACKNOWLEDGMENTS

Instead of being like the nesosilicate group, being in grad school is like being a part of the tectosilicates. An infinite network of Si tetrahedrons, an infinite network of support. I am extremely fortunate and appreciative for this support I have had throughout my Ph.D. at UNR.

First, I would like to thank my advisor, Dr. Philipp Ruprecht. Whatever I write will not do justice to the years of guidance, mentorship, and patience. I am forever grateful for his dedication to my development as a scientist through advice and encouragement. Through his reassurance, I have become a more confident scientist. I would also like to thank my committee members Drs. Stacia Gordon, Wenrong Cao, Scott McCoy, and Deena Schmidt for their guidance, interest, and reassurance through the years. Not only did they provide valuable feedback through meticulous comments and advice, but I had the honor of learning from many of them through coursework at UNR.

In addition to my committee members, I am extremely grateful for Dr. Matt Loewen at the Alaskan Volcano Observatory for the collaboration throughout the years. I am thankful for the chance to work on samples from Veniaminof and for every conference meetup to discuss and enthuse about Veniaminof. I am fortunate to have been awarded a Kleinman Award in 2018 for initial work on melt inclusions at Mount Veniaminof that evolved into the project in this dissertation. During this time, I had the honor of using samples from multiple scientists at the USGS and Alaska Volcano Observatory, such as Drs. Kristi

Wallace, Tom Sisson, and Charlie Bacon. I am also thankful for support from Dr. Jessica Larsen about navigating working with USGS samples.

Throughout graduate school, I have been fortunate to work with brilliant scientists in the lab. First and foremost, I am extremely grateful for Dr. Joel DesOrmeau, a wizard of microanalytical techniques. Joel is the kingpin of the Department of Geological Sciences and Engineering at UNR, and I am so fortunate to have learned more about SEM, laser, and microprobe techniques from him. I am so thankful for his support and friendship. I also had the pleasure of learning the ins and outs of SIMS from Dr. Rick Hervig at Arizona State University through workshops and instrument time. I am thankful for the time and interest throughout the years.

I am fortunate to have worked with so many amazing researchers in the magma group at UNR, such as Max Gavrilenko, Heather Winslow. I have gained so much from group meetings through the years. Specifically, I would like to thank Heather Winslow for her friendship, encouragement, and for being an excellent office mate. I am so proud of us! I would also like to thank Pooja Sheevam, Drew Levy, Scott Feehan, Luz Lim, Alex Hoinville, Mara Nutt, Emily Dektar, Lizzie (Langdone-Lassagne) Sheridan, Ziva Shulaker, Lauren Sankovitch, and Ethan Leuchter (among many others) for their friendship and encouragement throughout the years. I am so thankful for you all. I am also grateful for both Tessa Carlson and Jiaming Yang for their friendship, as well as Caitlin McHugh and Stefani Lukashov.

Most of all, I would like to thank my family. This dissertation would not have been possible without support from my parents, Barbara and Mike; my sister, Jennie; and my dog, Geyser. But, most of all, I am so thankful for my partner, Kurt Kraal, for his unwavering support and love.

TABLE OF CONTENTS

LIST OF TABLES

LIST OF FIGURES

CHAPTER 1: Introduction

Introduction

Volatiles in magmas (H_2O, CO_2, S, Cl, F) are significant to numerous processes in igneous systems, from the generation to the eruption of magma. The solubility of volatiles is highly pressure dependent, so in magma reservoirs, volatiles can be dissolved within the silicate melt. As magma ascends during an eruption, volatiles become saturated in the magma and exsolve into a vapor phase, with the growth of transportation of bubbles modulating the eruption style. Furthermore, the stability of mineral phases can be influenced by volatile contents, with the exsolution of volatiles driving the nucleation of microlites and growth of crystals further impacting the rheologic properties of magma and possibly leading to more explosive eruptions. Thus, determining the depth of magma storage and quantifying ascent are key variables for hazard forecasting and mitigation. This dissertation aims to examine techniques applied for quantifying ascent rates (Chapters 2 and 4) and apply methods used to determine magma storage (Chapter 3).

In chapter two, I explore thermodynamic drivers of disequilibrium dissolution and growth of plagioclase microlites during ascent by modeling the chemical affinity (the degree of disequilibrium) between plagioclase at set compositions and an evolving silicate melt due to exsolution of H_2O during ascent using Python-based MELTS in the ENabling Knowledge Integration (ENKI) server. The lack of microlites in volcanic samples is often suggested to form due to kinetic limitations of microlite growth during fast magmatic ascent. However, many magmatic systems are disrupted thermally due to recharge prior

to eruption and such systems may also lack extensive microlite crystallization. Through this work, I was able to show that reheating and ascent significantly reduces any kinetic limitation on microlite formation. Microlite-free eruptions do not require the high ascent rates imposed by kinetics alone.

Chapter three characterizes the pre-eruptive storage and volatile budget using melt inclusions from the 2018 eruption at Mount Veniaminof, a large, open-vent stratovolcano in the western Alaskan Peninsula. Melt inclusions are small aliquots of silicate melt that are trapped within growing mineral host. The host crystal acts as a pressure capsule for the silicate melt, preserving a record of the composition of the magma and concentration of volatiles at the time of entrapment. The Aleutian Arc has been the locus of a multitude of studies about the role of water in arc magmatism (Wei et al., 2021; Zimmer et al., 2010), but many of these studies have overlooked the Alaskan Peninsula. The Alaskan Peninsula represents the most western segment of oceanic-continental crust subduction before the transition to oceanic-oceanic crust subduction. Specifically, this dataset expands the volatile record to a section of the Aleutian arc that is lacking volatile data and presents the first direct volatile measurements for Mount Veniaminof. Different geochemical trends and models developed in the Aleutian arc predict a moderately hydrous source, and the melt inclusion record at Mount Veniaminof is in agreement with this hypothesis. I observe minor variation in volatile concentration through time during the eruption.

In chapter four, I evaluate the usage of the melt embayment geospeedometer as an ascent chromometer for magma during eruptions. Like

melt inclusions, melt embayments (ME) are pockets of melt that are trapped within a crystal during growth, but are never fully closed off and remained connected to the external melt (Liu et al., 2007). During magma ascent, volatiles respond to the changes in pressure forming a compositional gradient from the interior of the melt embayment to the outlet. A diffusion profile can be fitted to these compositional gradients leading to characterization of ascent rates. Previous studies have been limited to ME with a simple geometry to simplify characterization of diffusive fluxes, leading to potential biases in data collection from studies with small (>10) sample sizes. This chapter aims to explore the use of non-conventional ME, including necked and complex shapes. Opening measurements to ME with more complex geometries can expand the usage of embayments to more eruptions and show variability in ascent rates recorded in larger populations. Melt embayments in olivine phenocrysts from the 2018 Mount Veniaminof eruption are highly abundant and vary in geometry from classic 1-D channel shapes to highly necked, thin straw channels. I characterized the large variation in embayment geometry via 3D visualization from computed X-ray computed tomography (micro-CT) of 26 olivine grains. Detailed analyses of these grains reveal complex growth histories and highlights textural relationships between melt embayments and the growth of clusters of olivine crystals that would have been lost during sample preparation without the usage of micro-CT. This research calls into question what exactly previous melt embayment studies were measuring.

Chapter 2: Using Chemical Affinities to Understand Disequilibrium Textures of Plagioclase Preserved in Magmatic Systems

Published: Geophysical Research Letters

Ellyn G. Huggins[1], Philipp Ruprecht[1], and Mark S. Ghiorso[2]

[1] Department of Geological Sciences and Engineering, University of Nevada, Reno, MS-172, 1664 N. Virginia St., Reno, NV 89557, United States of America.

[2] OFM Research, Seattle, WA, USA

.

Huggins, E. G., Ruprecht, P., & Ghiorso, M. S. (2021). Using chemical affinities to understand disequilibrium textures of plagioclase preserved in magmatic systems. *Geophysical Research Letters*, *48*(10), e2021GL092884.

ABSTRACT

Volcanic textures are strongly related to magma ascent histories. Degassing of a volatile-rich magma can drive plagioclase microlite growth on eruptive timescales, but such growth can be inhibited when ascent is sufficiently fast. Thus, the absence of microlites is used to determine minimum ascent rates. However, open-system processes, such as magma recharge, prior to decompression can also suppress microlite growth, possibly extending the timescales for ascent. Here, we explore the trade-offs between degassing-driven growth and reheating-driven suppression of microlite formation. We develop a quantitative model on the basis of the chemical affinity that accounts for disequilibrium driving crystal growth or dissolution. We test decompression scenarios to understand how net-crystallization varies with different pressure-temperature ascent histories for the 2008 Chaitén eruption. Degassing-driven growth and reheating-driven dissolution are balanced for ascent rates of 0.002-0.006 MPa/s (~0.08-0.25 m/s) from 200 MPa storage depth and reheating by 50-70 ˚C, significantly reducing minimum ascent rates.

PLAIN LANGUAGE SUMMARY

Understanding how fast magma ascends during an eruption is critical for volcanic hazard mitigation. One way to determine the speed comes from the minerals carried in the volcanic rocks. As magmas ascend to the surface, pressure

decreases, and gasses such as H_2O or CO_2 are released that were initially dissolved in the magma. This process can drive the growth of small crystals, known as microlites. The lack of microlites in rocks that formed from explosive silicic eruption is commonly interpreted to represent magma ascent so fast that there is insufficient time to form microlites. Alternatively, if the magma is disturbed prior to eruption by the addition of hotter magma (also known as recharge), microlite formation can also be suppressed. Thus, any model that uses the lack of microlites to determine magma speed needs to consider effects by hot recharge. Here, we present a method that calculates the effect that hot recharge may have on the formation of microlites during an eruption. We present a range of alternative scenarios that can suppress microlites, many of those extending to much slower magmatic ascent speeds. Thus, these results may provide new insights on how magmas ascend during an eruption.

1. Introduction

Magmatic systems are susceptible to changes in their equilibrium state through mass and energy exchange. The implication of open-system behavior manifests in changes in rheologic properties of magma, affecting magma ascent and eruption style (Métrich et al., 2010; Ruprecht & Bachmann, 2010; Cassidy et al., 2018). The perturbation away from chemical equilibrium during the course of magma evolution is most pronounced during syn-eruptive ascent, where rapid changes in dissolved volatiles have large effects on the equilibrium phase assemblage (Lange et al., 2009; Waters & Lange, 2015; Waters et al., 2015). In addition to changes in volatile content, further disruptions of equilibrium conditions occur during magma recharge, mixing, crustal-interactions, and/or reheating (La Spina et al., 2016; Mollo et al., 2011; Ruprecht & Bachmann, 2010). Because open system processes can only partly be observed following eruption, our understanding comes from thermodynamic models (Berman, 1988; Ghiorso & Sack, 1995; Gualda et al., 2012; Ghiorso & Gualda, 2015), mineral chemistry (Davidson et al., 2005; Ginibre et al., 2007; Ruprecht & Wörner, 2007), and interpretation of textures in rock samples (e.g., Streck, 2008; Castro & Dingwell, 2009; Brugger & Hammer, 2010; Mollard et al., 2012; Arzilli & Carroll, 2013; Befus & Andrews, 2018).

Plagioclase is widely used as a recorder of these shallow open-system magmatic processes, as it preserves compositional variance (Grove et al., 1984; Morse, 1984), is stable over wide P-T-X conditions, and is sensitive to changes in intensive variables as well as melt and volatile concentration (Error! Bookmark

not defined.; Sisson & Grove 1993; Ginibre et al., 2002; Humphreys et al., 2007; Ruprecht & Wörner, 2007). Experimental studies demonstrate that degassing of fluid-saturated magmas produce large degrees of undercooling; thus, overall net-growth should increase on eruptive timescales (Hammer & Rutherford, 2002; Mollo & Hammer, 2017). So, a paradox emerges when the decompression and subsequent eruption of a fluid-saturated magma produces microlite-poor rocks with little increases in net-growth of phenocrysts.

Glassy, microlite-free or -poor tephra is common in volcanic systems (Hammer et al. 1999; Castro & Dingwell, 2009; Ruprecht et al., 2012; First et al., 2021). Lack of microlites with little textural or chemical modification of phenocrysts is commonly attributed to rapid ascent of magma, where plagioclase growth and microlite nucleation is kinetically suppressed (Hammer & Rutherford, 2002; Martel, 2012; Waters et al., 2015). However, the formation of such textures may be influenced by additional disequilibrium processes. Reheating of magma following recharge can drive mineral dissolution along the liquidus, hindering the growth of microlites during ascent (Ruprecht & Bachmann, 2010). If reheating is followed by decompression and degassing-driven crystallization, microlite formation can be impeded. Ignoring such disequilibrium processes can result in an overestimation of ascent rates if disequilibrium processes are not accounted for.

Here, we develop a method to quantify the degree of disequilibrium associated with a chosen P-T-X path. This model approximates the saturation state of plagioclase when compared to a melt phase at set P-T-X conditions,

using a thermodynamic parameter, the chemical affinity. The chemical affinity is a constructed value based on the chemical potentials of endmember components in the mineral phase relative to an omnicomponent phase, a meta-stable phase that contains all of the thermodynamic components of the mineral phase (i.e., a silicate melt). Our modeling approach tracks the chemical disequilibrium between plagioclase of fixed composition (see supplementary text) and a decompression-driven degassing melt. We calculate chemical affinity maps that provide a quantitative framework to explore unique magma pathways linked to perturbations in intensive parameters from an initial stage of (near-equilibrium) magma storage. Specific time-dependent scenarios can be tested and connected to emerging magmatic textures. We apply this model to understand if plagioclase dissolution/crystallization in response to reheating caused by magma recharge can be an alternative to rapid ascent suppressing microlites in a crystal poor, silica rich system. Our model uses Python-based MELTS, through the Enabling Knowledge Integration (ENKI) Project (Ghiorso & Sack, 1995; https://gitlab.com/ENKI-portal/ThermoEngine).

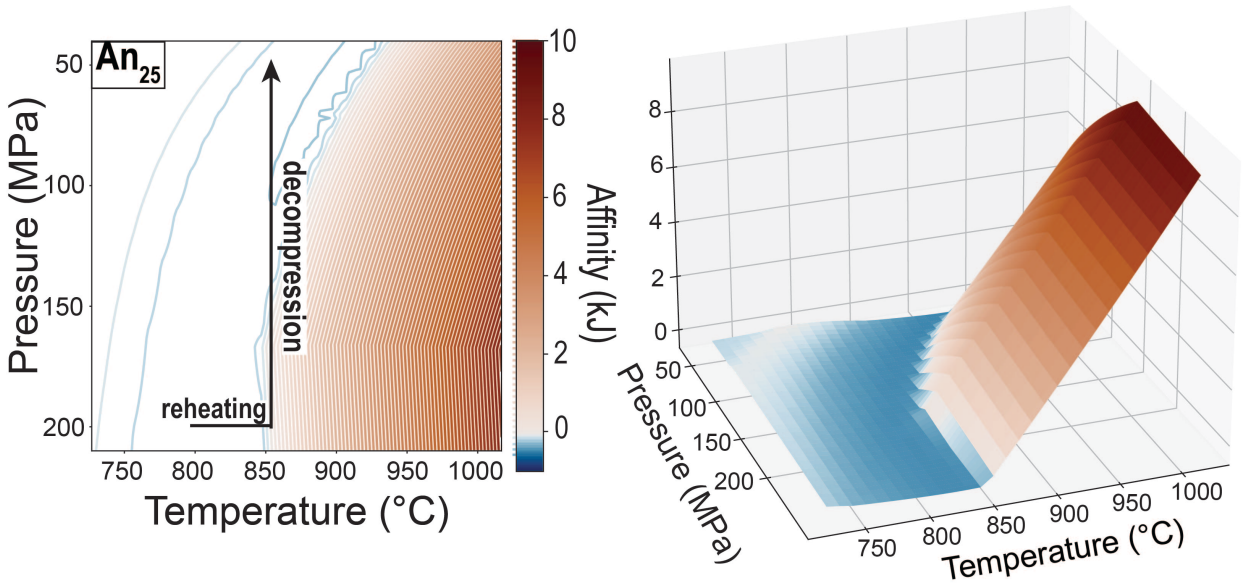

Figure 2.1. Contour maps of the chemical affinity of plagioclase and an evolving melt**.**

Left: Contour map of the chemical affinity for plagioclase (An25) with respect to a silicic melt as a function of pressure and temperature. Positive affinities (red) result in crystal dissolution, while negative affinities (blue) drive crystallization. Right: 3D representation of the chemical affinity showing the increasing affinities with increasing phase instability compared to little changes in the affinities within the stability field. The scientific colormap vik (Crameri, 2018a; Crameri et al., 2020) is used in this figure to improve accessibility for readers.

2. Methods

Whether a mineral crystallizes or dissolves under specific P-T-X conditions is governed by the minimization of the Gibbs free energy of the liquid+solid(s) assemblage (e.g., Ghiorso & Sack,1995). Thermodynamic modeling software packages, such as MELTS, are frequently used to track magma evolution, however such approaches intrinsically assume equilibrium. While a thermodynamic equilibrium approach approximates the general pathway that

magma may take during decompression and the response to the magmatic system after cooling, reheating, or change in composition, it does not consider the degree of disequilibrium a phase may experience during those changes in intensive parameters along the decompression path. However, thermodynamically, the stability of an individual phase can be estimated using its chemical affinity (Ghiorso,1987; Edwards & Russell,1998).

The chemical affinity is based on comparisons of the partial molar Gibbs free energy of a phase when compared to an omnicomponent phase—such as an aqueous phase or silicate melt. It provides a quantitative estimate of the saturation state of the phase in question and, thus, is a measurement of the degree of disequilibrium in the system (Ghiorso,2013). Because the chemical affinity represents the stability of a mineral phase in a multicomponent silicate melt, it is the thermodynamic driver for crystal nucleation, growth, and dissolution (Turnbull & Cohen, 1960; Dowty, 1980; Lasaga, 1982; Ghiorso, 1987; Edwards & Russel, 1998; Alexander, 2011).

We calculate the chemical affinities in P-T space for a given melt and fixed mineral composition (Figure 1) using the thermodynamic modeling software MELTS (Ghiorso & Sack, 1995) and a mineral database of thermodynamic properties (Berman, 1988, see Text S1 for details about the modeling approach). The latter is used to calculate the chemical potential of plagioclase endmembers. The chemical affinity is calculated by the summation of the stoichiometric coefficient (v) of the component in the solid (s) and melt phase (m), respectively,

multiplied by the chemical potential (μ) of each component at each temperature and pressure step.

$$A = \sum_i v_{i,s}\,\mu_{i,s} - \sum_i v_{i,m}\,\mu_{i,m}$$

For plagioclase, the total affinity of the phase is equal to the sum of the mole fraction of each endmember multiplied by the affinity of each end-member (Ghiorso, 1987). When the affinity is positive, plagioclase at a chosen composition is undersaturated and unstable, and has a higher free energy than the omnicomponent phase. At an affinity of zero, plagioclase is in equilibrium, and plagioclase is supersaturated and stable when the affinity is negative (**Figure 2.1**).

MELTS software (Ghiorso & Sack, 1995; Gualda et al., 2012; Ghiorso & Gualda, 2015) already returns the chemical affinities of undersaturated phases during equilibrium calculations. However, standard MELTS calculations neither provide the chemical affinities of supersaturated phases nor the chemical affinities of specific compositions (An) of a phase. However, to explore the response of existing crystals of known composition, their affinity needs to be determined when the melt composition and equilibrium conditions change. Our model enables the calculation of such phases and therefore provides flexibility to understand how specific phases react (grow or dissolve) as intensive variables change (Huggins et al, 2021).

3. Model Conditions for the 2008 Chaitén eruption

We apply our model to the 2008 Chaitén eruption, which lacks microlites. This absence of microlites was studied experimentally to explore kinetic limits and to infer rapid ascent of rhyolite (Castro & Dingwell, 2009). We explore how reheating preceding decompression may reduce the need for rapid ascent to suppress the formation of microlites. The 2008 Chaitén eruption is a good test case, because 1) it produced crystal-poor high-silica (~75.6 %) rhyolite and therefore can be modeled well with MELTS-based methods, 2) existing experiments on the Chaitén compositions constrain pre-eruptive phase equilibria and storage/crystallization conditions, and 3) the presence of plagioclase resorption textures suggest that some disruption of the long-term storage conditions preceded ascent. While we present the model using these specific compositions, our disequilibrium model can calculate disequilibrium behavior for a range of melt and mineral compositions as well as different P-T paths.

Starting plagioclase and silicate melt compositions were taken from Castro and Dingwell (2009, Table 1 in Castro & Dingwell), based on representative matrix glass and plagioclase compositions of the rhyolite pumice from the 2008 eruption. The natural plagioclase anorthite contents of the Chaitén pumice range from An_{40} to An_{45}, with rare calcic cores (An_{68}). In contrast, MELTS predicts more sodic plagioclase compositions to be in equilibrium with the given melt composition. Thus, we model two additional anorthite contents (An_{14}, An_{25}) that are in equilibrium with the 2008 Chaitén melt compositions according to MELTS and are typical for rhyolitic systems. Pre-eruptive magma storage conditions of

150–200 MPa and 780–825 °C were determined from equilibrium phase assemblage experiments. Measured water concentrations in plagioclase-hosted glass inclusions range from 1.3–2.3 wt%. The explosive nature of the 2008 Chaitén eruption and low CO_2 concentrations led Castro and Dingwell (2009) to assume that a water-saturated rhyolite magma degassed prior to or during eruption. Measured water concentrations in melt inclusions can be unreliable, as they are susceptible to diffusive re-equilibration and rapid loss of H^+ (Gaetani et al., 2012; Lloyd et al., 2013) as well as post-entrapment crystallization (Kent, 2008). Our model runs assume pre-eruptive water concentrations (~5.8±0.35 wt% H_2O) calculated using plagioclase hygrometry (Waters & Lange, 2015), an experimentally-determined average storage temperature of 800 °C for the 2008 Chaitén eruption and a storage pressure of 200 MPa and to simulate the maximum decompression path consistent with equilibrium experiments (Castro & Dingwell, 2009). We explore in less detail shallower storage (150 MPa, Figure S3) to provide constraints on the effect of pressure.

For each anorthite content (An_{14}, An_{25}, An_{40}), chemical affinities were calculated over a P-T grid with temperatures ranging from 726 to 1026°C (10 °C steps) and pressures from 40 to 200 MPa (1 MPa steps), respectively (**Figure 2.1**). Co-existing melt compositions and dissolved volatile contents were updated for each P-T condition, thus neglecting any effects of supersaturation. Given that heating and decompression-driven degassing may have a compensating effect on the stable plagioclase composition and the control over dissolution or growth, we can explore the partial suppression of microlite growth using a scenario of

reheating and decompression. We explore this balancing effect of decompression and reheating on plagioclase composition by using the dependency between H_2O solubility and pressure (Newman & Lowenstern, 2002; Liu et al., 2007), calculated using the Waters and Lange (2015) hygrometer (**Figure 2.S1**). There is a quasi-linear relationship between the change in water content and change in temperature needed to keep plagioclase at a set anorthite content, further explored in the supplemental text. Due to this balancing effect and for simplicity, we assume that plagioclase composition does not change for all P-T conditions. If decompression is not compensated by a reheating event prior or during decompression, a wide range of plagioclase compositions can crystallize from the melt during ascent (Waters et al., 2015).

4. Results

Affinity maps were created for each anorthite content (**Figure 2.1a, 2.S2**). Each map represents the chemical affinity for a given anorthite content and an evolving melt composition with respect to the dissolved volatile content. These affinity maps are not showing the equilibrium plagioclase composition; instead, they demonstrate whether plagioclase of known composition is thermodynamically stable ($A<0$) or unstable ($A>0$). For our three different plagioclase compositions (An_{14}, An_{25}, An_{40}), the two low anorthite contents are stable across a range of pressures and temperatures. As noted above, the An_{40} case never reaches permissible growth conditions; thus, the An_{40} case is not discussed further. Stable plagioclase compositions typically show only small

variations in the chemical affinity within their stability region (**Figure 2.1b**). In contrast, as conditions change towards dissolution, the chemical affinity increases rapidly. The further away the plagioclase composition is from stable P-T conditions, the larger the associated chemical affinity. This translates into distinct responses of growth and dissolution as the system moves further in or out of the region of stability. Underlying is the assumption that growth and dissolution rates are proportional to the chemical affinities (Ghiorso, 1987). Thus, while large positive affinities drive rapid dissolution rates, near-constant negative affinities drive less variable growth rates.

Once affinities are calculated, the potential plagioclase response to any pressure-temperature-time path can be modeled (**Figure 2.2a, b**). We focus on the simple case of reheating followed by isothermal decompression. Thermal pulses may vary depending on the thermal contrast, the physical and dynamic interaction, the respective compositions, and the relative proportions of the host and recharge magma (Ruprecht & Bachmann, 2010; Ruprecht et al., 2012). We choose a reheating of 50, 60, and 70 °C from a storage temperature of 800 °C. Such thermal pulses have been proposed for several silicic systems (Quizapu, >50 °C for the 1846-1847 lava flow, Ruprecht & Bachmann, 2010; Degruyter et al., 2017; Santorini, 40 °C; Degruyter et al., 2016; Long Valley Caldera, Evans & Bachmann, 2013). As a reference for the effect of reheating, we compare the cases of reheating plus decompression to the case of decompression without reheating.

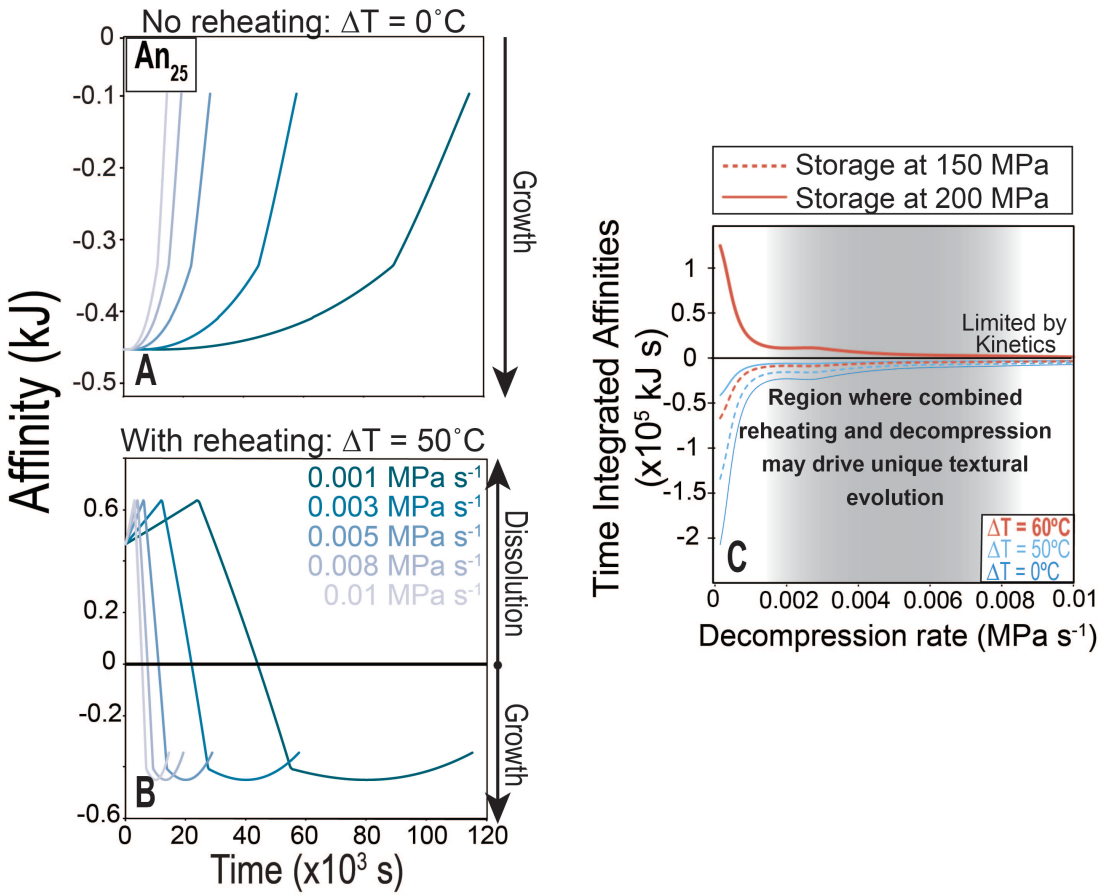

Figure 2.2. Changing chemical affinities along a decompression pathway**.**

Changing chemical affinities of plagioclase (An_{25}) along a defined reheating-decompression path and with varying decompression rates. Decompression rates range from fast (0.01 MPa s^{-1}) to slow (0.001 MPa s^{-1}). A) The decompression-only, no reheating case shows negative affinities throughout ascent. B) The 50 °C-reheating plus decompression case demonstrates that during ascent, shallow/late growth follows a deep/early stage of dissolution. Different constant decompression rates lead to stretching of the affinity-time curve without change in topology. Thus, relative proportions of dissolution and growth during ascent are constant. Decompression and any reheating start from storage conditions of 200 MPa and 800 °C. C) The time integrated chemical affinity for different decompression rates at An_{25}. Solid lines represent storage at 200 MPa and dashed lines represent storage at 150 MPa. Also shown are variable degrees of reheating ranging from no reheating (thin blue), 50 °C (light blue), and 60 °C reheating (thick orange). Increasing decompression rates minimize syn-eruptive changes in crystallinity which approaches a kinetic limit at high decompression rates. Large degrees of reheating lead to net crystal dissolution irrespective of decompression rate.

We explore a range of decompression rates. Recent studies estimated decompression rates from melt inclusions and embayments (e.g., Humphreys et al., 2008, Liu et al. 2007, Lloyd et al., 2014, Barth et al., 2019) on the order of 10^{-3} to 10^{0} MPa s^{-1}. However, most of these studies explore more mafic compositions. Castro and Dingwell (2009) suggested for the 2008 Chaiten eruption a rate of 0.5 m/s (0.01 MPa s^{-1}), using a density of 2300 kg m^{-3} for the overlying rock mass, representing a kinetic limit above which syn-eruptive growth and dissolution were suppressed. Taken this density, our modelled decompression rates from 0.001 MPa s^{-1} to 0.01 MPa s^{-1} correspond to ascent velocities of 0.06, 0.18, 0.24, 0.35, 0.5 m s^{-1}, which are reasonable for natural silicic systems (Rutherford, 2008; Castro & Dingwell, 2009). Decompression starts from storage pressures of 200 MPa, which represent a common magma storage depth of 8.8 km, and chemical affinities along each path are extracted at 1 MPa intervals. Decompression rates from past eruptions are typically discussed in the context of constant rates. However, feedback between degassing and magma buoyancy, as well as changes to the conduit shape, may lead to ascent rates that vary along the decompression pathway (Gonnermann & Manga, 2007; Lloyd et al., 2014). This concept is further discussed below.

The chemical affinities along each decompression path are calculated for the two plagioclase compositions that are stable (An_{25} and An_{15}) with and without 50 °C pre-ascent reheating (**Figure 2.2a, b; 2.S3a, b**). For the case of no reheating, affinities are always negative, which is consistent with crystallization caused by decompression-driven degassing (e.g. Blundy & Cashman, 2001). However, after

50 °C of reheating, our plagioclase compositions are unstable at the storage pressures, and remain unstable for the first part along the decompression path. In the case of An_{25}, a longer section of the decompression path is spent in the unstable regime. As decompression and degassing continues, plagioclase re-enters the field of stability and crystallization may resume. It should be noted that a plagioclase-bearing mineral assemblage may not respond to reheating with the overgrowth of more calcic plagioclase rims. Instead, partial equilibrium experiments have shown that the system is sluggish with respect to crystallization during small degrees of reheating (First et al., 2021).

5. Discussion

Our model demonstrates and quantifies the potential changing regimes of growth or dissolution during ascent. Thus, we can explore potential changes in conduit dynamics that are strongly controlled by changes in viscosity (Gonnermann & Manga, 2007). For constant decompression rates, the degree of reheating and the starting pressure control whether growth or dissolution dominates. Any change in decompression rate only stretches the chemical affinity-time relationship (**Figure 2.2a, b**). By integrating the affinities over the entire decompression path with respect to time, we can estimate whether growth or dissolution dominates during ascent. In the case of pre-eruptive reheating, we quantify the importance of deep/early dissolution (where heating dominates) relative to shallow/later growth (where degassing dominates; **Figure 2.2c**). Depending on the ascent rate and specific P-T path, a variety of plagioclase

responses may occur. Ascent without reheating always leads to negative chemical affinities and crystallization (e.g. Blundy & Cashman, 2001). For constant decompression rates and small degrees of reheating prior to ascent, shallow/late crystallization always dominates the net affinity budget. In this simple model, the transition to positive time-integrated chemical affinities occurs between 50-70 °C of reheating (depending on the considered plagioclase composition). Thus, net crystallinity reduction during reheating and decompression may be the result and the transition occurs over a narrow temperature range, which is below the resolution of many mineral-based thermometers (e.g. Blundy & Cashman, 2008). If decompression is assumed to start at 150 MPa, the relative contribution of shallow/late growth increases. Nonetheless, with increasing decompression rate, the time integrated affinity approaches zero and any syn-eruptive changes in crystallinity become increasingly negligible.

While our main model focused on a simple case of isothermal decompression with a constant decompression rate, more complex processes could also limit the net growth of plagioclase during ascent. First, the assumption of a constant decompression rate for the full decompression pathway is an oversimplification. Exsolution of volatile species in the melt changes viscosity and bulk density on ascent, facilitating magma acceleration. A slower starting decompression rate (0.001 MPa s^{-1}) followed by faster decompression (0.01 MPa s^{-1}) may inhibit degassing-driven later growth of plagioclase microlites. To assess the effect of changing decompression rate and plagioclase stability during mobilization, we

tested various cases of changing decompression rate (**Figure 2.3**). Instead of correlating a decompression rate with changes in density of the melt during ascent, we look at different cases of changing decompression rate after 50°C reheating in a four hour window: 1. a linearly accelerating decompression rate; 2. an exponentially increasing decompression rate; and, 3. decompression that is initially slower (0.001 MPa s^{-1}) and then changes to a faster decompression rate (0.01 MPa s^{-1}) at the third hour. Plagioclase growth is inhibited for all three cases presented for the An_{25} ($\int A\ dt>0$). For An_{15}, plagioclase growth is inhibited only for case three (not shown).

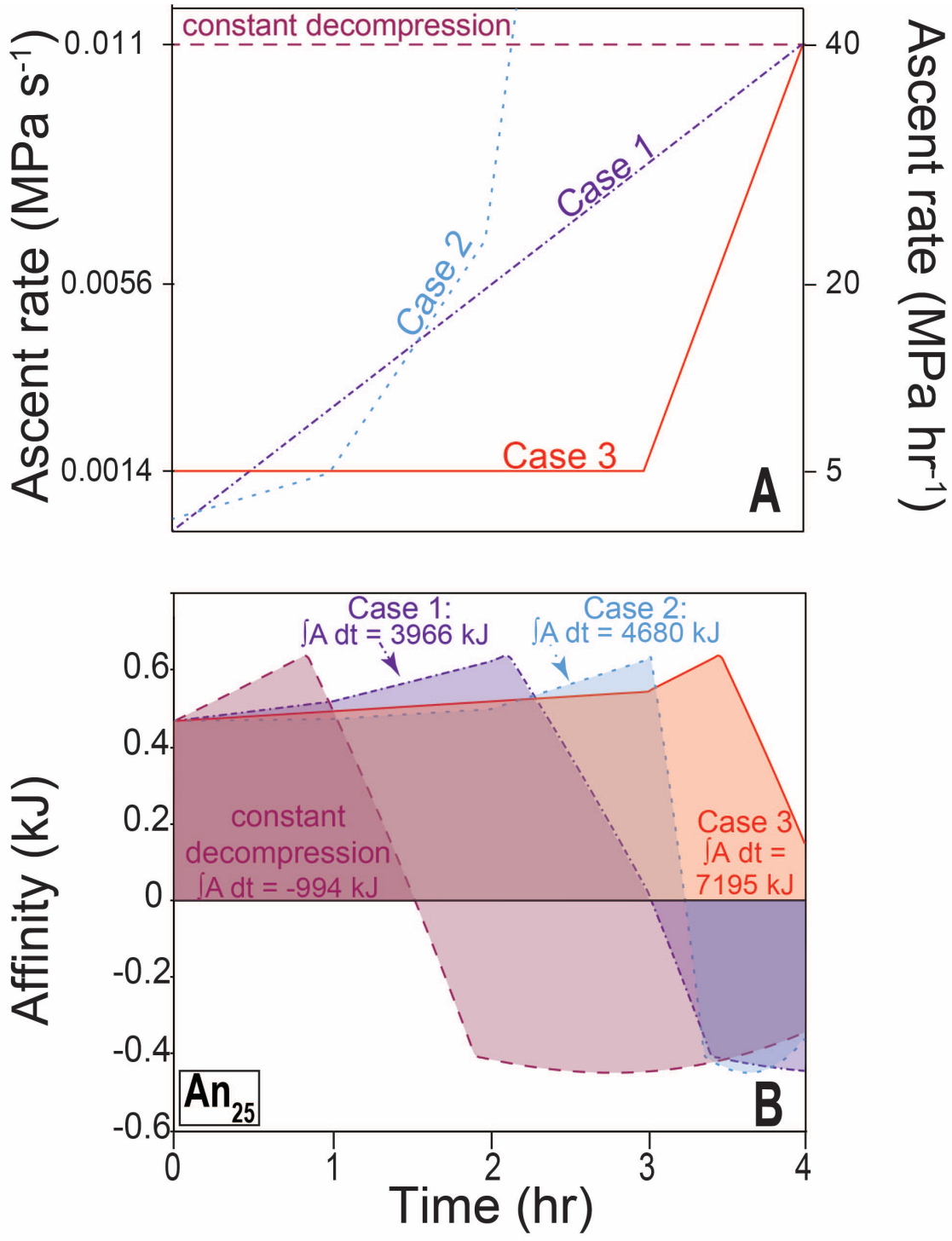

Figure 2.3. Changing affinities with non-continuous decompression.

A) Three different cases of non-continuous decompression rate after 50 °C of reheating compared again a case of constant decompression rate (scenario 0).

Scenario 1: Linear acceleration of decompression rate; Scenario 2: Step wise linear increase of the decompression rate approaching an exponential; Scenario 3: Initial slow constant decompression (0.0014 MPa s^{-1}) transitions into a linear increasing decompression rate (0.011 MPa s^{-1}). B) Affinity-time curves for the different decompression scenarios highlighting the changes of time spent in the growth or dissolution regime. Each curve is labeled with the time-integrated chemical affinity. Only scenario 0 leads to net growth, scenarios 1-3 which all incorporate acceleration on ascent lead to net dissolution.

Secondly, cooling due to adiabatic decompression could lead to increases in net growth along the ascent pathway. Exsolution of H_2O from a water saturated melt during decompression could increase the liquidus temperature for crystallizing plagioclase, increasing the effective undercooling ($T_{liquidus}$-T_{melt}), and driving nucleation. However, in a shallow system like Chaitén, the changes in pressure are small and so are adiabatic cooling effects. Reheating has also been proposed during degassing-induced syn-eruptive crystallization and the associated release of latent heat (Blundy et al., 2006). While previous studies have shown that per 1% crystallization of plagioclase yields temperature rise of 3.2 °C, and crystallization at Shiveluch and Mount Saint Helens raised the temperature of the system by 100 °C during ascent (Couch et al., 2003; Blundy et al., 2006), such models invoke crystallization itself as the agent for the heating. However, here we want to explain eruptions that lack syn-eruptive crystallization, specifically microlites. Nonetheless, if growth is limited to existing crystals, the release of latent heat may also provide a mechanism to delay microlite formation if growth on existing crystals exceeds 10-20 % and heating reaches ~60–70 °C, as required in our models. However, in the case of crystal poor systems, not

enough thermal energy is released to move the system back into an unstable state.

While textures interpreted from Chaitén have been interpreted to be suppressed kinetically (Castro & Dingwell, 2009), we present that a balance of reheating and degassing could be an alternative method for inhibiting microlite growth. Recently, Andrews and Befus (2020) replicated Castro and Dingwell's decompression experiments through their model Supersaturation Nucleation and Growth of Plagioclase (SNGPlag) to model crystallinity and number density. SNGPlag models the time dependent relationship between nucleation and crystallization of plagioclase during decompression. At a decompression rate of 40 MPa h^{-1}, SNGPlag predicts a higher crystal number density than what was reported in Castro and Dingwell. Andrews and Befus (2020) suggest that this is due to their model not accounting for nucleation delays. Given that the natural plagioclase phenocrysts lack euhedral rims, indicating that they were resorbing prior to or during the eruption (Castro & Dingwell, 2009), microlite suppression could also be caused by reheating of magma prior to ascent. This could account for the lower crystal number density in the natural samples compared to the model outcomes of SNGPlag, and, therefore, potentially reconcile their model outcomes with observations.

Discerning between the different mechanisms of crystal growth (and dissolution) is important for understanding the development of textures on and prior to ascent, and our model can be used in future studies to estimate the degrees of effective undercooling or superheating, while connecting that to

textures and rates of crystallization or dissolution. For example, at fast decompression rates and associated large degrees of effective undercooling, phenocrysts continue to crystallize disequilibrium textures (swallowtails, melt hollows, venniform, etc.). Our model would identify where such conditions exist during ascent. Also, in the case of microlite formation that is not impeded by diffusive limitation during fast decompression, the model may inform why acicular habits prevail (Mollo & Hammer, 2017). Similarly for slower decompression rates, more euhedral crystal habits can be produced as the mineral components have sufficient time to diffuse to the growth site, and our model can be used to quantify the degree of undercooling along the entire length of the ascent pathway (Sunagawa, 1992; Mollo & Hammer, 2017). Lastly, our model is versatile to explore any P-T-t path and, therefore, can also help quantify the cumulative thermodynamic driving forces associated with thermal histories of melts prior to decompression. In particular, previous experiments have shown that the presence of crystals prior to decompression can influence the number density of plagioclase and the morphology of plagioclase crystals, where pre-decompression crystallization could decrease the energy barrier required for nucleation during decompression (Martel, 2012). Other experiments have shown that reheating of magmas past the liquidus prior to eruption can influence texture development (Tsuchiyama, 1983; First et al., 2020). Superheating melt above the liquidus prior to decompression reduces the amount of nucleation sites where microlites can grow (Waters et al., 2015; Mollo & Hammer, 2017) and can delay nucleation with increasing initial superheating (Tsuchiyama, 1983). Thus, using

chemical affinity estimates extracted via P-T-t paths from our model with crystallization and nucleation models may further help to link textures from experimental results and natural systems with thermodynamic constraints.

6. Conclusion

Understanding the stability of mineral phases is critical when interpreting the textural evolution of samples. With python-based MELTS, we are able to explore the role of disequilibrium in dynamic magmatic systems by using the chemical affinity. We are able to track these changes in equilibrium state during periods of unrest, either through decompression or reheating, by mapping the chemical affinity of plagioclase in in P-T-X space. Because the chemical affinity represents the degree of disequilibrium of a mineral phase in a multicomponent silicate melt, it is a proxy for crystal nucleation, growth, and dissolution. During these periods of unrest, understanding kinetic timescales is important for interpretations of textures. Our calculations show that there is a range in decompression rates where plagioclase growth response is sensitive to changes in temperature and pressure. If recharge events are closely followed by decompression, the textural evolution may be balanced, leading to hindered microlite growth, a texture commonly attributed to kinetic limitations due to rapid ascent.

While subject to limitations, our model nonetheless demonstrates that fast ascent timescales may not be the only mechanism hindering microlite growth during decompression. Instead, timescales for ascent may be lengthened. Future

iterations of the model will discern between nucleation versus bulk crystallization and account for equilibrium versus existing plagioclase compositions during growth and dissolution periods, respectively. In addition, the model will track changes to melt chemistry due to growth and dissolution

Acknowledgements

PR acknowledges US National Science Foundation grants EAR-1347880 & EAR-1717288. The source code is accessible at http://doi.org/10.5281/zenodo.4723866. We would like to acknowledge the supportive and constructive comments of our reviewers, Silvio Mollo and David Neave, for the improvement of our manuscript.

.

Appendix

Introduction

The supporting information includes a more detailed description of the basis of the chemical affinities model, and supplementary figures on plagioclase stability and affinity maps and decompression calculations for the other anorthite contents.

Text S1. Thermodynamic Basis for Modeling Conditions

The MELTS model includes internally consistent thermodynamic properties of silicate melt and plagioclase. The plagioclase and silicate melt phase models are both based on known thermodynamic databases (i.e., Berman, 1988) that are built into the Enabling Knowledge Integration Project (ENKI) framework. In our model we first find the equilibrium state of the omni-component phase at a set bulk composition using MELTS. Omni-component phases are (meta)stable and contain all the thermodynamic components in the system that can determine the saturation state conditions (Ghiorso, 2013). We use Rhyolite-MELTS version 1.2.0, which is suited for volatile-rich silicic phases (Ghiorso & Gualda, 2015), to calculate the changing composition of the co-existing melt phase due to decompression driven degassing. Recent versions of Rhyolite-MELTS allow for mixed fluid (H_2O +CO_2) phases (Ghiorso & Gualda, 2015), but other MELTS models can be employed if needed. Plagioclase compositions remain constant

for each P-T case. For each pressure and temperature step, the thermodynamic properties of both the melt and plagioclase phase are calculated, where the Gibbs free energy of the melt and plagioclase of fixed composition is updated using published thermodynamic properties (Berman, 1988).

We record the chemical potential of this omni-component phase. In a second step, we calculate the chemical potentials for the endmember components of the mineral of interest, e.g., a plagioclase of a specific major element composition via the ENKI project (https://gitlab.com/ENKI-portal/ThermoEngine). Lastly, we calculate the chemical affinity, referred to as the affinity in the text, for the mineral phase in question and the silicate melt at the set bulk composition. We then compute the chemical affinity with this three-step algorithm over a pressure and temperature grid using steps sizes of 1 MPa and 10 ºC, respectively.

The difference to conventional MELTS modeling is the use of a specific plagioclase composition, instead of calculating the equilibrium plagioclase composition. We use this approach to reconcile that natural systems, which experience changes in P and T, the existing plagioclase has a fixed composition (i.e., it does re-equilibrate diffusively on relevant timescales) while the melt stays near the equilibrium (i.e., volatile exsolution). Thus, the chemical affinity of the existing plagioclase crystal is continuously changing. As a result, this model addresses the questions whether the existing crystal can dissolve or crystallize in the changing melt composition. We note that the focus here is more specifically on dissolution of the existing crystal. Is there any driving force for this? We

recognize that crystallization would probably promote growth of a “new” composition, not the fixed one chosen here. However, given that changes to the chemical affinity in the growth regime are small (Figure 1) compared to changes to the chemical affinity associated with the dissolution regime, we make this simplification here. Moreover, the difference between the chemical affinity of the plagioclase in equilibrium with the evolving melt and the chemical affinity of the set plagioclase is small. For a dissolving crystal, the assumption of a constant plagioclase composition over the P-T is justified due to the slow response time of existing crystals.

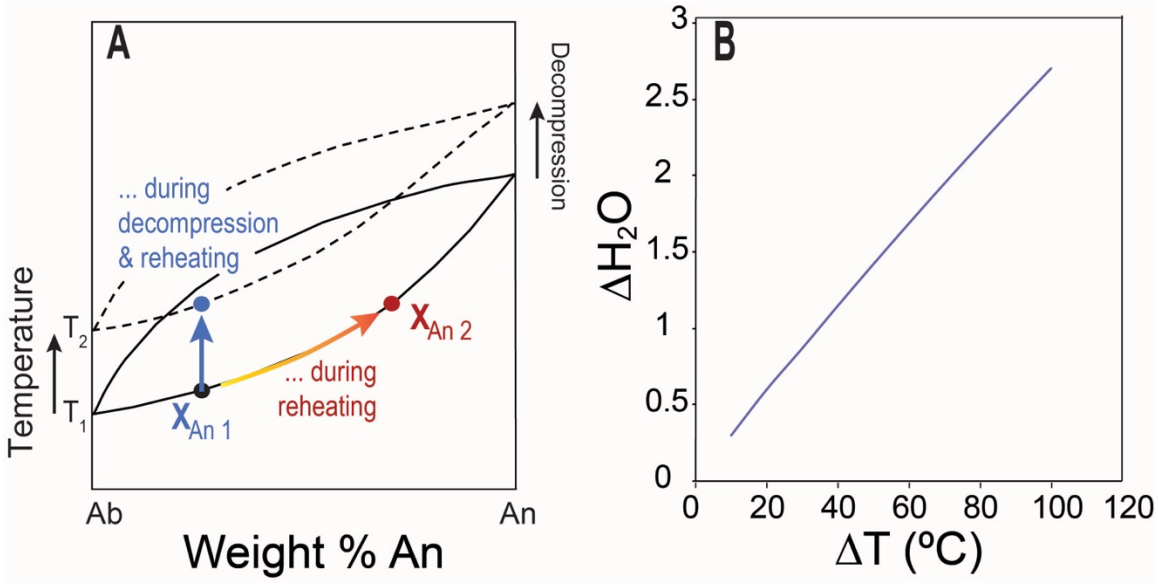

Figure 2S.4. Schematic plagioclase solid solution phase diagram**.**

A) Schematic plagioclase solid solution phase diagram. The dashed line shows the effect of decompression on plagioclase phase relationships. Plagioclase composition does not change considerably with decompression if it is compensated by reheating. B) Quantification of the water (ΔH_2O) and temperature (ΔT) effect for a fixed anorthite content using the Waters & Lange (2015) hygrometer. The change in water content is linked to the changes in pressure.

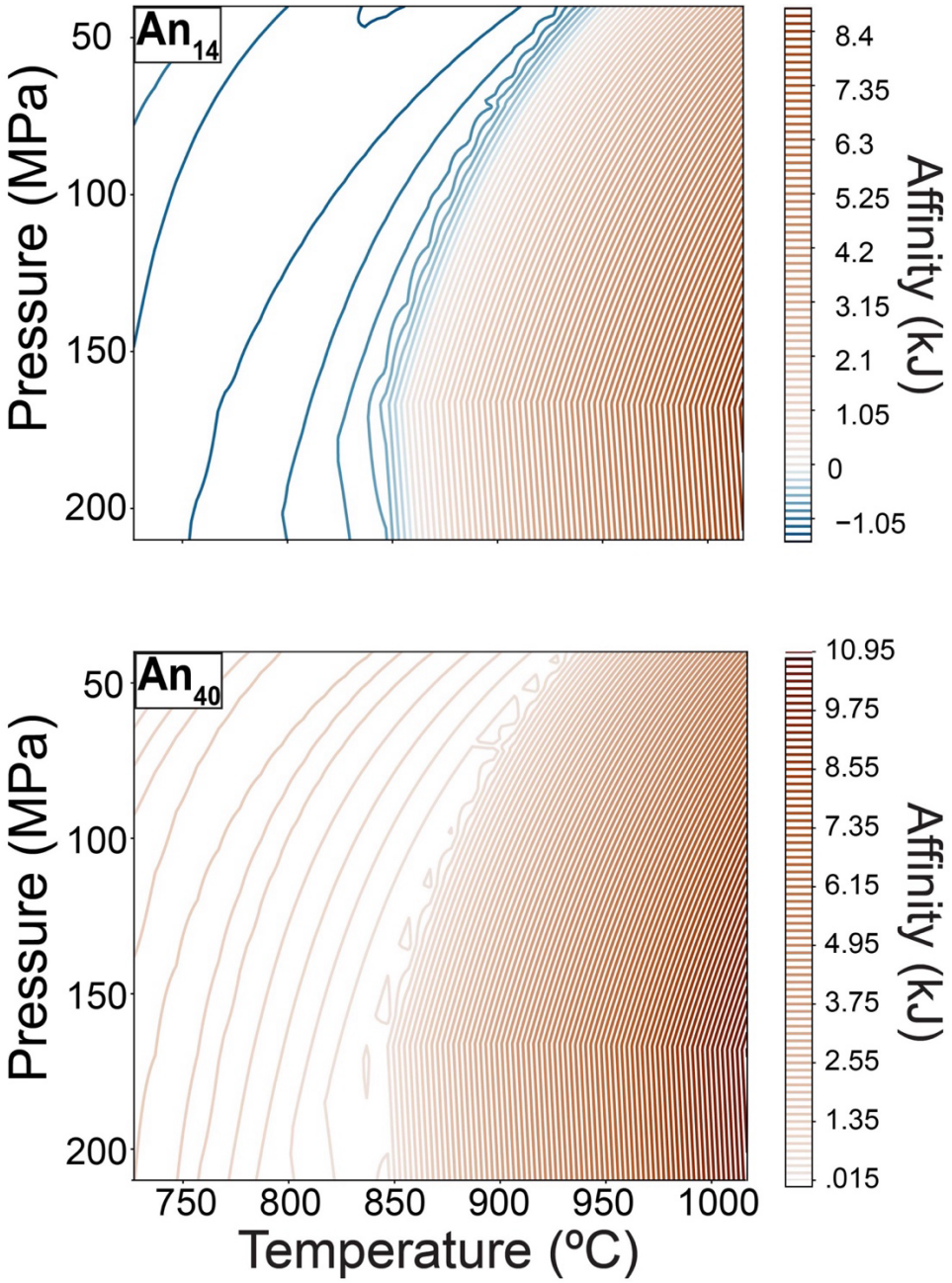

Figure 2S.5. Affinity contour maps for An_{25} and An_{40}**.**

The co-existing melt is identical to Figure 1. The scientific colormap vik (Crameri, 2018; Crameri et al., 2020) is used in this figure to improve accessibility for readers.

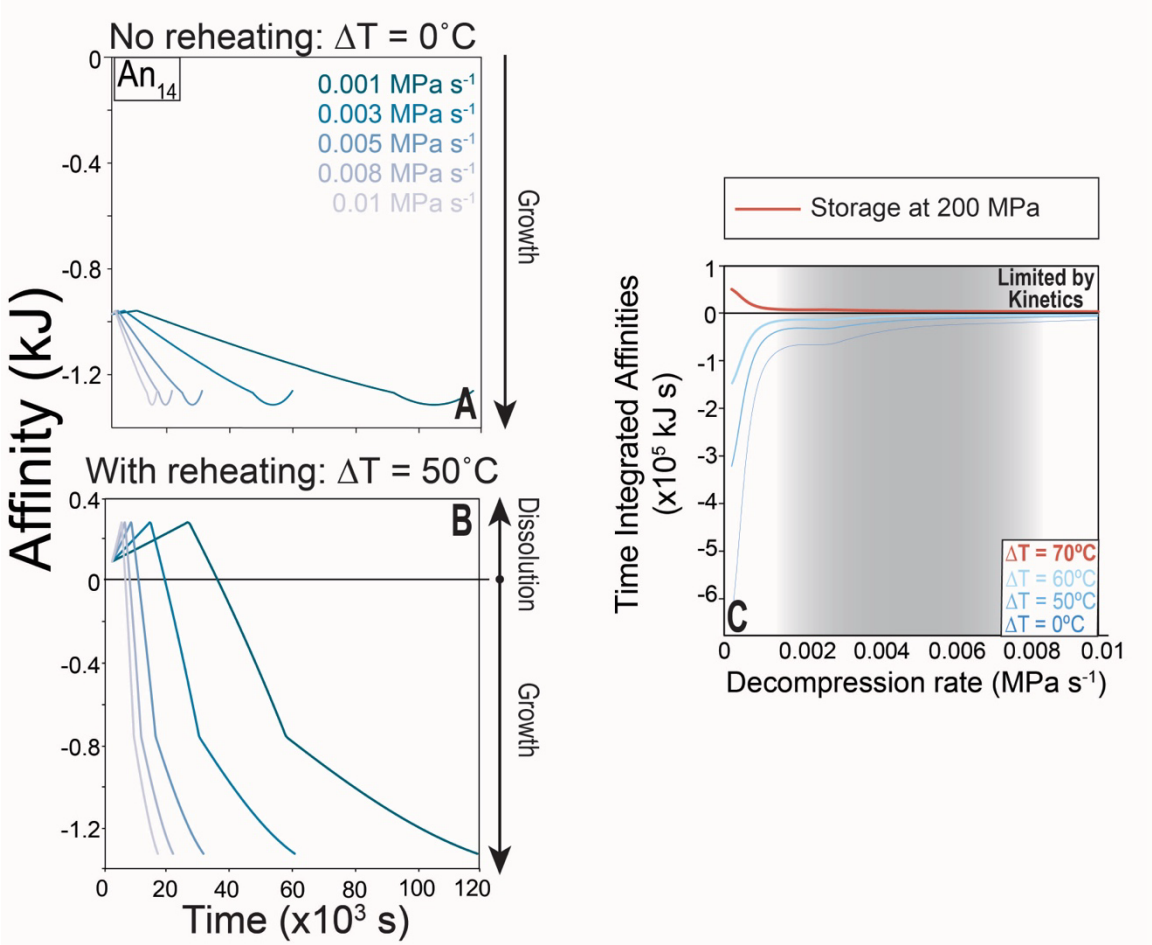

Figure 2S.6. Changing chemical affinities of plagioclase (An_{14}) along a defined reheating-decompression path and with varying decompression rates**.** . Decompression rates range from fast (~0.01 MPa s^{-1}) to slow (~0.001 MPa s^{-1}). A) The decompression-only, no reheating case shows negative affinities throughout ascent. B) The 50ºC-reheating plus decompression case demonstrates that during ascent, shallow/late growth follows a deep/early stage of dissolution. Decompression and any reheating start from storage conditions of 200 MPa and 800 ºC. C)The time-integrated chemical affinity for different decompression rates at An_{14}. Solid lines represent storage at 200 MPa. Also shown are variable degrees of reheating with no reheating (thin dark blue), 50 ºC (medium blue), 60 ºC (light blue), and 70 ºC (the thick brick orange) reheating. Increasing decompression rates minimize syn-eruptive changes in crystallinity which approach a kinetic limit at high decompression rates. Large degrees of reheating lead to net crystal dissolution irrespective of decompression rate

CHAPTER 3: Using olivine-hosted melt inclusions to assess pre-eruptive magma storage depth for the 2018 eruption at Mt Veniaminof, Alaska.

In preparation for submission to G-cubed

Huggins, E.G, Ruprecht, P., Loewen, M., Gavrilenko, M., Harlaux, M., Bodnar, R.

ABSTRACT

Mount Veniaminof is a frequently active, open-vent, tholeiitic arc volcano on the western Alaska Peninsula. One of the most recent eruptions (September–December 2018) began with small lava flows and culminated in a larger explosive event in November that produced a 450 km-long continuous ash plume—one of the most significant ash-producing events in recently observed eruptions at Veniaminof. A temporarily constrained tephra record was sampled post-eruption by exposing tephra layers preserved in a snow pit and correlating them with deposits imaged by satellite during the eruption. Bulk compositions are basaltic andesites (58 wt% SiO_2) with olivine ranging from Fo_{64-79}.

We present volatile element concentrations (H, C, S, Cl, F) from a total of 65 olivine-hosted melt inclusions (MI) from 6 separate tephra layers to assess potential syn-eruptive changes to the volatile budget. H_2O concentrations within MI suggest moderately hydrous magmas, ranging from 0.3-2.4 wt% H_2O, higher than expected from regional geochemical trends. H_2O contents can be reconciled with MND estimates from Loewen et al (2021) using a polybaric storage history. The large range in CO_2 concentrations in the MI (8-2180 ppm) also is supportive of this history. Moderately heavy δD values (-38-277) and the presence of mineral precipitates along the circumference of some shrinkage bubbles suggest that reported concentrations of both H_2O and CO_2 are minimum estimates. H_2O and CO_2 measurements correspond to minimum entrapment pressures of 400

MPa and entrapment depths <15 km. Our estimates of magma storage depths are supported by relatively deep precursory long period earthquakes (16-20 km). There is no variation observed in volatile concentration through each tephra layer correlated with the November explosive event.

1. Introduction

The Aleutian–Alaska subduction zone (AASZ) has been a natural laboratory to develop a variety of models for the petrogenesis in subduction zones, specifically exploring the role of slab inputs and water contents in primitive magmas and their links to arc magma genesis (Jicha & Kay, 2018; Kay & Kay, 1985; Plank, 2005; Singer et al., 2007; Wei et al., 2021; Yogodzinski et al., 2015). Current models of the AASZ propose a connection between eruption dynamics, magma storage, and magma chemistry with underlying plate structure and local tectonics (Kay et al., 1982; Larsen, 2016). These models are consistent with recent melt inclusions results that argue that magma storage depth and the formation of crustal magma reservoirs is controlled by magmatic water content, with higher magmatic water contents leading to deeper magma storage (Rasmussen et al., 2022).

Within the AASZ, the Alaskan Peninsula segment constitutes a transitional segment from convergence of the Pacific and North American plates in the east and convergence between the Bering and Pacific plates farther west (**Figure 3.1a**; Buurman et al., 2014; Larsen, 2016). Geographically, this extends from

Douglas in the east to Dutton in the west. Along this east-to-west transect the magma chemistry changes from more calc-alkaline magma compositions with deeper storage to more tholeiitic compositions and shallower storage depths (Buurman et al., 2014; Larsen, 2016; Ryan et al., 2012; Shillington et al., 2015). While there is an abundance of volatile element data (H_2O, CO_2, S) for other sections of the AASZ, studies that focus on edifices in the western Alaskan Peninsula are scarce even though it encompasses frequently active, open-vent volcanoes, such as Mount Veniaminof, that also have a history of large caldera-forming eruptions (Bacon, 2007). This paucity in data is the target of this study to shed light on a volcanic system and its volatile budget driving the frequent eruptions and to understand magma storage in a tectonic transitional zone.

Mount Veniaminof is one of the most active centers in the AASZ (Loewen et al., 2021; Waythomas et al., 2022) and represents the easternmost volcanic center in the Alaskan Peninsula. Here we focus on the 2018 eruption that was among the largest and longest eruptive events in Veniaminof's recent history. The beginning of the 2018 eruption had little precursory warning and minor ash deposition and lava flows. However, there was an increase in seismic tremor leading to a minor paroxysm with an increase in ash emission in November, 2018 before volcanic activity declined with minor ash fall and lava flows in December 7, 2018 before ending by December 27 (Loewen et al., 2021). The November explosive event marked the most explosive phase in Mount Veniaminof's recent history. Initial analyses of glass and whole rock chemistry, microlite density, and groundmass componentry show that there were minor changes in groundmass

componentry prior to the late November minor paroxysmal event and slight increases in MgO content in whole rock data after (see figure 7 in Loewen et al., 2021). The roles of volatiles during this eruption have not been studied. This eruption lends itself to a detailed analysis of the volatile budget compared to other eruptions in the Alaska Peninsula because of the well-linked temporal eruptive activity and tephra record.

To understand the volatile budget driving the more explosive section of the 2018 eruption at Mount Veniaminof, we utilize olivine hosted melt inclusions (MI) from different tephra sections during this eruption. Melt inclusions are aliquots of silicate melt that are sequestered inside host crystals during mineral growth (Roeder, 1979; P. J. Wallace et al., 2021). After entrapment, melt inclusions are assumed to be sealed and thus protected by the host mineral from compositional changes of the initial magma composition due to differentiation and degassing. By targeting host phases from initial crystallizing phases, such as olivine, melt inclusions can retain chemical information about the magma driving eruptions when the inclusion was captured (Welsch et al., 2013, Ruprecht and Welsch 2023). Melt inclusions are trapped at depth prior to or during the degassing of volatile species with pressure-dependent solubilities (e.g., references). MI are thus a powerful tool for understanding the pre-eruptive volatile concentrations, such as H_2O, CO_2, S, Cl, and F, that have pressure dependent solubility.

We present volatile contents, major elements, trace elements, and D/H isotope data from melt inclusions from the different time-integrated tephra data from the 2018 eruption at Mount Veniaminof to understand pre-eruptive storage

conditions and the roles of volatiles in changes in eruption dynamics during the eruption. Using these datasets, we explore how Mount Veniaminof fits into arc wide trends and can further inform storage of tholeiitic magma in the AASZ.

2. Geologic Setting

Mount Veniaminof has a prolific Holocene history of explosive and effusive volcanic activity, with caldera forming eruptions in the Holocene. The most recent eruption was ~3700 years ago and is associated with a near-surface variably solidified crystal mush column (Bacon et al., 2007). The post-caldera eruptions have been more primitive with a low Volcanic Explosivity Index (VEI<3) suggesting that the deeper-seated magmas can pass through this mush system unaffected. The historic volcanism continues to be dominantly basaltic andesite with frequent strombolian eruptions. Veniaminof has erupted at least 15 times in the past 200 years, with the most recent volcanic activity in 2018 and 2021.

The 2018 eruption at Mount Veniaminof started in one of the central cones in the larger ice-filled caldera in September 2018. Little precursory seismic warning or deflation preceded the eruption (Bennington et al., 2018; Loewen et al., 2021; Pesicek et al., 2018; Waythomas et al., 2022). Only two long period earthquakes at 16 and 19 km depths and harmonic tremor comprise the precursor activity on September 3rd, 2018 a day prior to the onset of ash emissions that lasted until December 2018 (Loewen et al, 2021; Waythomas et al., 2022). Intermittent lava extrusion commenced three days after the first ash emissions. The 2018 eruption

was dominated by Hawaiian – unsteady Strombolian activity, with lava flows and minor ashfall, which is typical for its recent eruptive history (Loewen et al., 2021). By November 19th, there was an increase in seismic tremor, and on November 21st, ash emissions increased for several hours leading to a 450 km long ash plume heading 400 km SSE of the vent. Seismic tremors had subsided by the next day (Loewen et al., 2021). The increase in explosivity marked one of the most significant ash-producing events in Veniaminof's recent observed volcanic activity. After the late November explosive event, volcanic activity subsided until a final explosive (December 13th to 20th) and effusive event. Veniaminof erupted again in 2021, but that eruption is not included in this study.

3. Samples

Periods of the 2018 eruption of Mount Veniaminof were accompanied by syn-eruptive snow fall, preserving tephra layers in the snowpack. Samples of these layers were collected by the Alaska Volcano Observatory in 2019 and correlated to different stages of the eruption using satellite imaging (**Figure 3.1**; AT-4598 and AT-4597: Initial September to October ash fall; AT-4596: 10/18/18 – 11/3/18; AT-4595: 11/4/2018 – 11/12/2018; AT-4593: 11/20/2018 – 12/1/18, AT-4591:12/13/2018-12/20/2018).

An aliquot of each bulk tephra sample was manually sieved into different size fractions without crushing. Following recent melt inclusion studies (Lloyd et al., 2013; Rose-Koga et al., 2021), olivine was separated using lithium

heteropolytungstate heavy liquid (LST; density of 2.85 g/ml) and manually picked from the heavy mineral separate, targeting the 200-800 micron fraction. Olivine grains were then immersed in mineral oil to inspect them for melt inclusions and to document their growth textures and crystal dimensions. Olivine-hosted melt inclusions are abundant in the 2018 Veniaminof eruption, with a total of 65 olivine grains. They can be divided into vapor bubble-bearing (n=22) and vapor bubble free melt inclusions (n=43), and they range from 25 to 30 microns in diameter. Melt inclusions span the entirety of the eruption--AT-4591 (n=1), AT-4593 (n = 22), AT-4595 (n=3), AT-4596 (n = 15), AT-4597 (n = 1), and AT-4598 (n = 23); however, we predominantly targeted the beginning of the eruption (AT-4598), the midst of the eruption (AT-4596), and the November explosive event (AT-4593).

3. 7Melt inclusion textures

Many inclusions are glassy, spherical, or oblate, but there are MI with negative crystal faceting (**Figure 3.1**). Angular spinel grains are present in a small portion of MI but are rare. While some MI are hosted in unbroken euhedral olivine grains, many MIs are contained in grain fragments. Thus, original grain dimensions and location of the melt inclusion within the olivine grain are unknown; the measured distance between the inclusion and grain boundary are minimum length scale estimates. To minimize this effect, the analyzed olivine-hosted MIs are from grains that are almost euhedral to subhedral with most crystal faces present. Moreover, MIs were chosen in larger fragments that preserved matrix glass around the grain circumference to retain information

about host grain textures and crystal orientation information. In the case of fragmented grains, crystallographic axes of grains were approximated based on grain shape and angles where edges were preserved, similar to the methodology of Salas et al. (2021). There is a smaller population of clustered subhedral olivine grains that are either twinned grains or connected along the crystal faces with minor volcanic glass between the grains. Many of the grains also contain multiple, smaller melt inclusions that were too small to analyze. These smaller melt inclusion morphologies either exist in random orientations or exhibit a spiral pattern (Welsch et al., 2014). This texture of melt inclusions has been observed at other volcanic systems in other mineral phases, such as in the clinopyroxene or plagioclase phenocrysts (Rapien et al., 2003; Streck & Wacaster, 2006). Other morphologies that are present but not discussed are anhedral grains with embayments and clots of olivine and clinopyroxene grains (Chapter 4).

4. Methods

4.1 Sample Preparation

Single olivine grains were picked and mounted in dental resin on a glass slide and exposed by polishing with 600-1200 grit silica carbide paper followed by 1-6 micron diamond paste. Melt inclusions and shrinkage bubble, if present, were measured in the x-, y-, and z-axes to calculate volumes of the melt inclusion and bubble (Supplementary document 1). The vapor bubble was within ~10 microns

of the polished surface for the Raman analysis. Subsequently, the MI were fully exposed (if needed), and olivine grains were removed from the dental resin mounts and pressed into an indium mount. After a final colloidal silica polish, the mount was gold-coated for secondary ion mass spectrometry (SIMS) analysis. After the SIMS analyses, the gold coat was removed, and the sample mount was carbon coated for electron microprobe (EMPA) analysis. The carbon coat was then removed, and a subset of olivine grains was analyzed via laser ablation inductively-coupled plasma mass spectrometry (LA-ICP-MS).

4.2 Raman Spectroscopy

Raman spectra were collected using a JY Horiba LabRam HR (800 mm) Raman spectrometer equipped with a 514 nm argon laser, confocal hole diameter of 1800 mm^{-1} gratings, and slit width of 150 μm under 100x objective magnification at Virginia Tech. Where noted, data was corrected using Ne lines (Supplementary document 1). A subset of shrinkage bubbles was reanalyzed using a Horiba LabRAM HR Evolution Raman spectrometer with an open-space confocal microscope and 532 nm Nd:YAG laser at the University of Nevada, Reno under the same analytical conditions at Virginia Tech, except for corrections with Ne lines. Three 60-150 s scans were collected and averaged, with analysis time depending on the strength of the signal. LabSpec and Fityk software were used to apply a baseline correction to each spectrum and to fit the CO_2 peaks using a combined Gaussian/Lorentzian (Voigt) fit. CO_2 densities were

calculated using the Lamadrid et al. (2017) densimeter using minimum, maximum, and average volume estimates of the melt inclusion and bubble. Average volume estimates are utilized for CO_2 density corrections and presented in Supplementary document 1.

4.3 Secondary Ion Mass Spectrometry

Volatile and minor element species (H_2O, CO_2, S, Cl, F, and P) were analyzed over two sessions using the Cameca IMS-6f at Arizona State University following SIMS analyses settings of Hauri (2002), including a primary current of 5-10 nA, impact energy of 15 kV, and a $^{133}Cs^+$ beam. During both sessions, samples were pre-sputtered for 180 seconds to remove the gold coat prior to data acquisition. The first two SIMS sessions were used to collect elemental volatile concentrations. During these sessions, the entrance slit was set to 0 µm, the exit slit to 48 µm, the field aperture was closed to 400 µm, and the energy slit was set to 40 eV. For both sessions, the mass spectrometer was operating at a mass resolving power of ~5000. Two check standards (Fonualei Rift:ND-60-01 and Mangatolu Rift:ND-70-01; Lloyd et al. 2013) were used as replicate analyses throughout the runs. Analyses of secondary reference glasses (VE32, D30-1, D52-5, ALV1833-1; (Hauri et al., 2002; Kumamoto et al., 2017) were analyzed to create the calibration curves (Supplementary Figure 1). Host-olivine grains were also analyzed to serve as a blank for the calibration curves (64-100 ppm H_2O). Due to lower resolution microscope imaging on the SIMS and small inclusion size, ion images of ^{13}Al and ^{19}F were primarily used to center the ion beam in the

melt inclusion. However, in some cases the ion beam was incorrectly placed touching the host olivine crystal leading to dilution of elemental data due to the instrument camera resolution and similarities in greyscale between the melt inclusions and host olivine grains. The analyses where this occurred are noted in the supplement.

A third SIMS session was used to collect hydrogen isotopic data of 18 Mis. This session was conducted at a lower mass resolution (MRP=800) on the Cameca IMS-6f at Arizona State University. Melt inclusions were pre-sputtered for 360 seconds using a current of 1-5 nA, a secondary accelerating voltage of 5 kV, and a $^{133}Cs^{+}$ primary beam. The entrance slit was set to 0 μm, the exit slit to 300 μm, the field aperture was closed to 400 μm, the contrast aperture at 150 μm, and the energy slit set to 0 eV. During these sessions, reference materials GL07, D52-5 and GL07 D30-1 (Hauri et al., 2006) were analyzed to create a calibration curve. D/H concentrations were calculated with an average DSMOW value of 0.0001559 and an average alpha value of 0.669 ± 0.011 based on standards.

4.4 Electron Microprobe Analyses

Point analyses of host olivine phenocrysts and melt inclusions were collected on a JEOL JXA-iHP200F field emission electron microprobe equipped with five wavelength dispersive spectrometers at the University of Nevada, Reno in two separate sessions. Profiles were collected using a mean atomic number (MAN) background correction for each element (Donovan et al., 2016). Standards used

for MAN background corrections are listed in supplementary document 2. Analyses of glasses within the MIs were obtained, with the following elements analyzed with counting times in parentheses: Na (5s), Al (20s) on a spectrometer 1 with large TAP; Si (20s), Mg (30s) on TAP on spectrometer 2; Fe (50s) and Mn on a large LIF on spectrometer 3; K (20s), P (40s), S (20s) on a large PET on spectrometer 4; and, Ca (20s), Ti (40s), and Cl (30s) on a large PET. All analyses were collevted using a focused beam current of 10 nA and an accelerating voltage of 15 kEV, except S and Cl, which were collected under at a higher beam current of 50 nA and an accelerating voltage of 15 kEV. Spot sizes ranged from 7-10 μm depending on the size of the inclusion. MRND60-01 and FRND70-01 were used as secondary standards (supplementary document 2). MI analyses was collected after SIMS analyses without polishing. When possible, analysis spots were placed outside SIMS rastered area. In the case of smaller MIs, analyses were within the rastered area and noted. Host olivine grains were obtained, with the following elements analyzed with counting times in parentheses: Na (40s) and Al (60s) on a large TAP on the first spectrometer; Si (20s) and Mg (20s) on TAP on the second spectrometer; Mn (40s) and Ni (50s) on a large LIF on the third spectrometer; Fe (20s), Cr (30s), and Ti (30s) on a large LIFL on the fourth spectrometer; and Ca (60s) and P (30s) on a large PET on the fifth spectrometer. For the analyses of the olivine hosts, we used a beam current of 50nA, accelerating voltage of 15 kV, and a spot size of 1 μm. A list of standards used for the MAN background are located in supplementary document 2. Corrections for post-entrapment re-equilibration were completed using

Petrolog3 (Danuyshevsky and Plechov, 2011) and verified with the Melt Inclusion Modification Model (MIMiC, Rasmussen et al, 2020).

4.5 Laser Ablation Inductively-Coupled Plasma Mass Spectrometry

Host olivine grains and melt inclusions were analyzed trace and minor elements at the Pacific Centre for Isotopic and Geochemical Research (PCIGR) at the University of British Columbia (UBC) using a Resolution M-50LR Applied Spectra 193nm ArF excimer laser ablation system coupled with a quadrupole Agilent 7700x ICP-MS. UBC measurements were performed at a repetition rate of 5 Hz on the melt inclusion and 8 Hz on host olivine and using a spot size of 34 μm. Energy density on the sample was ~2 J/cm^2. Calibration for trace element analyses was carried out by standard-sample bracketing using the silicate glass SRM NIST612 as external standard and Ca as an internal standard (from concentrations in the MI collected by EPMA). SRM NIST610, USGS basaltic glass standard reference material BCR2-G (Jochum et al., 2005), GOR128-g, GOR132-G (Jochum et al., 2006), MongOL (Batanova et al., 2019; Batanova & Sobolev, 2023) and San Carlos olivine were analyzed for quality control (Lambart et al., 2022; Ruprecht & Plank, 2013). Data reduction of the host olivine grains were calculated with Mg as an internal standard based on concentrations collected by EPMA.

Trace elements from 8 pairs of host olivine and melt inclusions were previously analyzed at the University of Nevada, Reno using a Resonetics RESOlution M50-E Excimer 193nm laser coupled with an Agilent 7700x ICP-MS.

For these analyses, a 40 μm pre-ablation spot size and 30 μm data-acquisition spot size were used at a repetition rate of 10 Hz. Data reduction was completed using Ca as an internal standard, previously collected using a JEOL JSM 7100FT at UNR. NIST-610 (Jochum et al., 2011), BCR2, BHVO2, ML3B-G (Jochum et al., 2005, 2006) GSC-1g, San Carlos olivine, and high Ni-content Corning Glass IR-X (Jarosewich, 2002) were used as second reference materials. A previous subset of olivine grains were also analyzed using a 40 μm pre-ablation spot size and 30 μm data-acquisition spot size at UNR. Data reduction were based off Mg as an internal standard calculated via stoichiometry (assuming binary solid solution between fayalite and forsterite). A suite of glasses and olivine (BHVO2G, Corning glass IR-X, GOR128-G, ML3B-G, NIST610, San Carlos Olivine, Marjalahti were used as standards to assess data accuracy. Data reduction was performed using the Iolite v.4 software (Paton et al., 2011) for both analyses at UBC and UNR.

5. Results

5.1 Host-olivine textures and compositions

For all olivine host morphologies, the cores of the grain have a narrow compositional range of Fo_{72-78}. There is insignificant variation in minor and major elements in the cores. Trace element compositions for representative olivine grains hosting melt inclusions are displayed in supplementary table 2 and **Figures 3.2, 3.3, and 3.4**. Olivine grains with melt inclusions do not have large

Ni/Cr numbers, while previously measured grains in unit AT-4593 and 2 grains from AT-4598 have large Ni/Cr ratios (**Figure 3.4**; Oeser et al., 2018, Ruprecht and Welsch 2023).

5.2 Post-Entrapment Modification (PEM) Corrections

Melt inclusions can be influenced by disequilibrium processes after the initial trapping of the inclusion during post-eruption modification. The trapped melt can deviate from equilibrium with the host olivine through crystallization or melting along the melt inclusion-olivine interface (Danyushevsky et al. 2000, Kent, 2008, Rassmussen et al. 2020). The initial trapped melt inclusion composition can be estimated by adding equilibrium olivine compositions back into the melt (subtracting, in the case of post-entrapment melting). We utilized both Petrolog 3.1 (Danyushevsky and Plechov, 2011) and Melt Inclusion Modification Correction (MIMiC, Rasmussen et al. 2020) to determine the amount of post-entrapment modification to the melt inclusions, assuming an oxygen fugacity of NNO (after Loewen et al., 2021). For both models we used Fe-Mg partition coefficients by Toplis (2005), oxygen fugacity calculated by Kress and Carmichael (1988), and olivine-melt equilibrium model of Ford et al. (1983). Since there is minor variation in FeO^T and MgO between analyzed melt inclusions and whole rock data from tephra from the 2018 eruption at Mount Veniaminof (Loewen et al. 2021, Supplementary document 2), we assumed that Fe-loss or gain in the melt inclusions is negligible (**Figure 3.5**, see discussion for

further detail). We calculate a Kd (Fe-Mg) of 0.29 to 0.35 using the Toplis (2005) model and an average $Fe^{3+}/\sum Fe$ of 0.21.

Based on Petrolog3.1 and MIMiC, melt inclusions require 5% post entrapment melting to 1% post entrapment crystallization and 5% post-entrapment melting to 5% post entrapment crystallization, for each respective model. Differences between both post-entrapment crystallization models are due to differences in the calculation of Kd values (Rasmussen et al., 2020; **Figure 3S.2**).

5.3 Major and Trace Element Concentration of Melt Inclusions

Major and minor element results are shown in **table 3.1**, **figure 3.5**, and **figure 3S.3**. Uncorrected melt inclusions from the 2018 eruption are predominantly of basaltic andesitic composition with two, more primitive inclusions (SiO_2 ~48.2 wt%, Na_2O+K_2O ~3.9-4.0 wt.%) and three more evolved inclusions (SiO_2 57.07-57.44 wt.%). Corrected melt inclusions fall into a similar range of basalt-basaltic andesite magma irrespective of whether Petrolog3.1 or MIMiC is used. There is variation between other major oxides (MgO: 3-6 wt.%, CaO: 6.2-9.7 wt.%, FeO^T: 8-11 wt.%, and Al_2O_3: 13-18 wt.%) in glass compositions from the 2018 eruption. Variations in glass compositions are gradational and do not point to a bimodality or distinct populations based on glass compositions. This variation is observed over each tephra unit and does not indicate that trapped melt inclusions vary with stratigraphic position.

Trace element compositions are listed in supplementary dcoument 2. For each tephra unit from Mount Veniaminof, MIs follow characteristic arc signatures

of enriched large ion lithophile (LILE) and light rare earth (LREE) elements relative to high field strength elements (HFSE), such as Nb, Ta, Zr, and Hf (Figure 6). Each tephra unit from the 2018 eruption at Mount Veniaminof are strongly enriched in Sr and Ba, but not other highly incompatible elements such as Pb and U. The trends in trace element data are consistent with a larger dataset of whole rock trace elements from multiple eruptions from Mount Veniaminof from Wallace et al. (2020) presented in Wei et al. (2021).

5.4 Volatile Concentration in Melt Inclusions

Corrected volatile element concentrations vary greatly across all melt inclusions with 0.23-2.40 wt% H_2O, below detection limit (bdl)-2815 ppm CO_2, 48-3111 ppm S, and 707-2045 ppm Cl. Corrections for H_2O are small because small degrees of post entrapment modification (uncorrected: 0.22-2.41 wt.% H_2O). These ranges in volatile species are observed in each tephra unit (**Figure 3.7 and 3.8, 3S. 4, Table 3.1**). CO_2 measurements are a combination of CO_2 dissolved in the melt and contribution from a coexisting shrinkage bubble.

The hydrogen isotopic values from Mount Veniaminof have δD values of -38 to +277‰ in δDSMOW values, with the majority of analyses ranging from δD values of 0-100‰ (**Figure 3.9**). We do not find a correlation between the range in δD and size of the melt inclusion, distance of the inclusion from an a- or b-axis of the grain, or the stratigraphic tephra layer (**Figures 3.9b and c**). δD values and calibration curves are listed in supplementary document 2.

Half of the melt inclusions analyzed contain one or more shrinkage bubbles, which requires that melt inclusion CO_2 concentrations are corrected for any CO_2 stored in the bubble. Shrinkage bubbles form due to the differential response between host olivine and melt inclusion as temperature and pressure changes (e.g., Aster et al. 2016). Important effects are, for example, the differences in thermal expansion of the melt and host olivine and pressure drops due to post-entrapment crystallization along the circumference of the melt inclusion (Roedder, 1979;Lowenstern & Thompson, 1995; Roeder, 1979). A pressure drop within the melt inclusion affects the CO_2 solubility, where CO_2 preferentially partitions into the vapor phase of the melt inclusion. Other volatile species may also partition into the vapor phase, but to first order the vapor phase is composed of pure CO_2 (Aster et al., 2016; Moore et al., 2015). We have observed mineral precipitates along the bubble-melt inclusion interface. The precipitates are less than a micron in size, and thus could not be analyzed.

In order to correct for CO_2 stored in the bubble, Raman analyses of shrinkage bubbles in melt inclusions from Mount Veniaminof were performed. The corrections are substantial for many melt inclusions resulting in an increase of the CO_2 budget of these melt inclusions. A full summary of the corrections is found in supplemental document 1.

5.4.1 *Differences in Raman spectra between instruments*

Discrepancies between repeat analyses of vapor bubbles at Virginia Tech and at UNR are due to the difference between analytical setup at each lab

(DeVitre et al., 2021). At Virginia Tech, prior to data collection, the instrument is calibrated using CO_2 standards. At UNR, the instrument was not calibrated prior to analyses. Other variations could be in part because of thermal variations between lab spaces at Virginia Tech and UNR. Temperature was noted between each analysis at Virginia Tech but were not noted at UNR.

6. Discussion

6.1 Source or storage: Insights from volatile concentrations

Whether corrected melt inclusion volatile contents represent records of crustal storage or provide links to magma generation in the mantle depends on the magma history before and since inclusion entrapment. Melt inclusions can retain information about subsurface magma storage and ascent; however, recent studies have documented that melt inclusions are leaky vessels that may be subject to modification (Barth et al., 2019; Barth & Plank, 2021; Bucholz et al., 2013; Gaetani et al., 2012; Lloyd et al., 2013; Newcombe et al., 2014; Portnyagin et al., 2008; Qin et al., 1992). At Mount Veniaminof, the highest concentrations of H_2O that we measured are 2.4 wt.% while typical H_2O contents in arc magmas are, on average, around 4 wt.% of water (Plank et al., 2013). To be able to discern if the MI are recording information about magma generation or storage at Veniaminof, melt inclusion compositions need to be corrected. Many corrections for post-entrapment changes to the melt inclusions have emerged, such as corrections for post-entrapment crystallization/dissolution (Danyushevsky et al.,

2002; Danyushevsky & Plechov, 2011; Rasmussen et al., 2020); Fe-loss or gain in melt inclusions (Danyushevsky et al., 2002); coupled Si-H2O loss in melt inclusions (Portnyagin et al., 2019); and, the loss of CO_2 or other volatile species to shrinkage bubbles (Aster et al., 2016; Moore et al., 2015; Moore & Bodnar, 2019) and the formation of mineral precipitates along the bubble-melt-crystal interfaces (Esposito et al., 2014). As such, when corrected for post-entrapment modifications, melt inclusions at Veniaminof remain one of the best and direct recorders of pre-eruptive magma conditions at the time of entrapment.

There have not been any previous direct measurements of volatile contents from the melt inclusions at Mount Veniaminof, so it is unclear whether the 2.4 wt.% measured in this study is truly representative. Instead, volatile contents have been estimated through indirect means, such as through microlite number density (Loewen et al. 2021). Using calculated Microlite Number Density (MND), melt SiO_2 compositions, a density of 2500 kg/m3, and estimated ascent rated based on precursory seismic activity and first eruptive behavior, Loewen et al. (2021) estimated that the magmas contributing to the 2018 Veniaminof eruption contained less than 0.75 wt.% H_2O. This disparity between the melt inclusion H_2O record and that from MND calculation is due the formation of microlites recording different stages of magma storage during the eruption compared to melt inclusions in early forming phases, like olivine. Microlites typically form in shallow conditions preceding eruption when the exsolution of volatiles stabilizes anhydrous crystals (i.e., olivine, clinopyroxene, plagioclase) and raises the liquidus temperature of the melt. This change in the liquidus temperature, or the

apparent difference between the liquidus temperature and actual temperature known as the undercooling, drives crystallization during decompression. On the other hand, olivine growth and the melts captured during growth, occur deeper in the storage system and thus are recording a different process than the MND calculations. Furthermore, the H_2O estimates from MND calculations is not in opposition to the melt inclusion data from Veniaminof when considering the effect of crustal processing, through degassing.

The datasets presented in this paper point to melt inclusions that are underrepresenting the volatile budget for this eruption. Melt inclusions are susceptible to re-equilibration through rapid diffusion of H^+ (Portnyagin, 2008, 2019; Gaetani et al. 2012, Bucholz et al, 2013, Barth et al. 2019, and others) with the surrounding olivine through incorporation of H^+ into cation vacancies within the olivine (Gaetani et al, 2012; Ferriss et al., 2018; Jollands et al. 2019, Barth et al. 2019, Barth and Plank, 2021). Numerous studies have documented that hydrogen loss from the melt inclusions can occur on timescales of magma ascent (Hauri, 2002; Portnyagin et al., 2012, 2019), and H_2O can re-equilibrate with the surrounding melt through vacancies in the olivine structure (Ferriss et al., 2018; Barth et al., 2019). We can assess how much modification Mount Veniaminof inclusions have endured through comparisons with other volatile concentrations.

6.1.1 *Corrections for post-entrapment water loss*

To reconcile how much degassing occurred, we compared melt inclusion water values to other hygrometers, such as Ca-in-olivine hygrometer (Gavrilenko

et al. 2016), coupled SiO2-H2O loss model (Portnyagin, 2019), plagioclase hygrometer (Waters and Lange, 2015), and the tholeiitic index (Zimmer et al., 2010) to try to rectify pre-degassed magmatic water contents. One caveat is that all the used hygrometers rely on melt chemistry, so even if they are independent of the direct volatile measurements, these analyses are largely reliant on glass chemistry from melt inclusion analyses.

6.1.2 *Coupled Si-H_2O loss hygrometer*

Based on experimental data, Portnyagin (2019) confirmed that diffusive loss of H_2O also causes a decrease in SiO_2, where H_2O and silica are incorporated along the olivine-melt inclusion interface. The model uses whole rock data to estimate initial trapping SiO_2 content, choosing WR data based on incompatible element ratios (CaO/Al_2O_3, Al_2O_3/TiO_2). With using WR data, there is the assumption that the system must be approximately a closed system and not have experienced assimilation of other crystals after the melt inclusions are formed until eruption. Since Veniaminof is an open-source volcano with an observed secondary population of cumulate olivine grains, melt inclusions from this study were carefully selected based on trace element ratios of the olivine host (Ni/Cr) and relationship between incompatible element ratios in the melt and whole rock data. None of the melt inclusions from host olivine grains have high Ni/Cr ratios and thus were included in these calculations (**Figure 3.4**). Furthermore, based on the little deviations between WR data and the melt inclusions in major element trends (**Figure 3S. 5**) and similar CaO/Al_2O_3 ratios,

we believe that this model applies to some of the melt inclusions in our system. Incompatible ratios of Al_2O_3/TiO_2 were not always similar between the WR and MI dataset.

Using the Portnyagin (2019) model, melt inclusions experienced a variable amount of SiO_2-H_2O depreciation, from no SiO_2-H_2O loss detected using the chosen WR values from the 2018 eruption, to raising the H_2O budget to ~4.64 wt.% H_2O (sample with a measured H_2O ~2.41wt.% H_2O; **Figure 3.10**). Average restored H_2O values of ~2.56 wt.% H_2O suggest a loss of ~56% of the initial H_2O from the melt inclusions. Due to the open-source nature of this edifice, this model may erroneously point to higher water contents than are verifiable. However, it does point out that the melt inclusions in this system have experienced variable post-entrapment degassing, for MIs that fit into the parameters of the model.

6.1.3 *Tholeiitic Index*

The Tholeiitic Index ($THI=FeO_{4.0}/FeO_{8.O}$) is a model based on the role of water and Fe enrichment and depletion in the genesis of calc-alkaline and tholeiitic magmas (Zimmer et al., 2010). By choosing Fe contents over the range of the liquid line of descent (LLD), the THI describes magma generation where magmas experience diverges in Fe due to H_2O suppressing the growth of plagioclase, leading to more abundant spinel growth. Thus, Zimmer et al. (2010) observed an anti-correlation between H_2O and THI. We calculated the THI for magmas at Mount Veniaminof using melt inclusion compositions and comparing the Fe content at the averaged FeO content at MgO 4.0 wt.% and the Fe content

at the highest MgO wt.% (MgO ~5.5 wt.%), due to the lack of primitive, high MgO compositions in this data set, with the original THI model using the FeO content at 8.0 wt.% MgO (**Figure 3.5**). THI calculations suggest that the 2018 eruption have an intermediate THI (~ 0.95) at the transition from calc-alkaline to tholeiitic. Using the parameterization of Zimmer et al. (2010), this leads to a H_2O estimate of 2.6 ± 1.1 wt.% H_2O (**Figure 3.10**). This result is similar to those observed in measured olivine hosted MI and is similar for THI and H_2O composition comparisons for other edifices in the Alaskan Peninsula (i.e., Emmons, Zimmer et al., 2010; Larsen, 2016). One caveat with H_2O estimates based on THI is that magmas from Mount Veniaminof do not extend over the whole LLD, so this estimate possibly does not capture the full scale or the lack of Fe-enrichment.

6.1.4 *Plagioclase Hygrometry*

To independently determine pre-eruptive water contents, we used two different mineral-based hygrometers. We first used measurements of cores of plagioclase grains measured by Loewen et al. (2021) and average MI melt compositions, and temperatures from olivine-liquid thermometry based on re-calculated melt compositions (1080ºC). We calculated H_2O estimates using the Waters and Lange (2015) plagioclase-melt hygrometer. Using these temperatures and MI melt inclusion data, H_2O estimates range from 1.5-2.2 wt% H_2O (**Figure 3.10**), corroborating the data from the highest measured H2O content in the olivine hosted melt inclusion. Accounting for possible higher

temperatures, at 1100 ºC, H_2O estimates range from ~1.00–2.10 wt.%, still within the observed range from the measurements of the MIs.

6.1.5 *Ca-in-olivine hygrometry*

Since olivine grains are already utilized in this data set, we also applied the Ca-in-olivine mineral hygrometer proposed by Gavrilenko et al. (2016) based on the partitioning of Ca in olivine. Underlying this hygrometer is the idea that H_2O in the melt reduces the activity of calcium through depolymerization of the melt structure, lowering the amount of Ca partitioning with increased presence of H_2O in the melt. Where H^+ diffusion through the olivine host is fast, Ca diffusion is orders of magnitude slower (Coogan et al., 2005; Costa & Morgan, 2010), leading to a method that might record initial H_2O contents in a system that is actively degassing and diffusively losing H_2O in the MI. To use this model, high precision Ca measurements are needed within the host olivine grain. Using equations (1), (2) and (4) of Gavrilenko et al. (2016), CaO contents predicts H_2O as high as 6.3 wt.%, and an average of 5.13 wt.%, a substantial increase than what has been directly measured or predicted using other methods (**Figure 3.10**).

6.1.6 *Implications*

These models elucidate that H_2O contents of the melt inclusions have been modified during storage, but it is unclear how much degassing has

occurred. The different methods presented points to a different amount of water loss (**Figure 3.10**), from not indicating any water loss (plagioclase hygrometer) to pointing to significant loss of H_2O (~60%, Ca-in-olivine). Most hydrogen isotope data from inclusions are heavy but do not point to a systematic loss (**Figure 3.9**). Instead, these melt inclusions may point to melt that had degassed prior to entrapment in melt inclusions.

Aside from volatile content in the MI, the major elements signatures preserve information about how the trapped melts have interacted with the host olivine and external melt leading to a decoupling of major elements through differentiation. Since host-olivine grains remain in contact with surrounding magma, Fe-Mg can diffusively exchange from the melt inclusion to the olivine leading to potential “Fe-loss” in MI. On the other hand, melting along the olivine-melt inclusion interface can lead to an increase in Fe within the melt inclusion (i.e., Danyushevsky et al., 2002; Danyushevsky & Plechov, 2011). For the 2018 eruption, Mount Veniaminof’s uncorrected melt inclusion FeO^T contents are close to the analyzed WR from the 2018 eruption, if not slightly higher. Furthermore, major element trends, including Fe enrichment at similar MgO contents, decreasing Al_2O_3 with increasing SiO_2 (**Figure 3.5**), also suggest these melt inclusions have experienced differentiation through crystallization of other mineral phases, such as plagioclase.

6.26.2 Storage Conditions

Olivine-liquid thermometry for the MIs recalculated based on the amount of post entrapment modification suggest entrapment temperatures from 1030–1140ºC (**Figure 3.11**, and averages around ~1060 ºC. These are consistent with the plagioclase hygrometer temperatures for both the rim compositions (1070–1090 ºC) and more anorthitic core temperatures of 1080–1100 ºC and olivine-saturated liquid thermometers from Putrika (2008) calculated in Loewen et al. (2021). Using MagmaSAT solubility models (Ghiorso & Gualda, 2015) through Vesical 2 python code (Weiser et al., 2022) for the melt inclusions from the 2018 eruption, we resolve a maximum storage pressure of 520 MPa. The populations of melt inclusions with 1000–2000 ppm CO_2 fall into entrapment pressures of 100-400 MPa. The presence of mineral precipitates around the bubble-melt inclusion interface also may indicate that estimates from shrinkage bubbles may lead to minimum estimates of CO_2 within the vapor bubble. While too small to analyze, they are readily apparent around many bubbles. With the current minimum pressure estimates and using a density of 2500 kg/m^3, we constraina maximum entrapment depth of 19 km and an average depth of ~4 km (**Figure 3.11**). When accounting for up to 6.3 wt% H_2O estimate (Gavrilenko et al., 2016), pressure estimates are increased to >500 MPa.

Previously published studies at Mount Veniaminof support the existence of a shallow magma body and complex mush column under Mount Veniaminof (Bacon et al, 2007), based on zircons in plutonic xenoliths and geologic mapping of the edifice (Bacon et al., 2009). A zoned magmatic plumbing system with

evolved melt ponding shallowly and hotter than more mafic magma stored deeper in the crust is supported by geophysical and geodetic studies (De Angelis and McNutt, 2007; Fournier and Freymueller, 2008; Bennington et al, 2018). These studies point towards a shallow inflation center from (1–5 km) beneath Mount Veniaminof. Moreover, magma produced from the recent Holocene eruptions at Mount Veniaminof tend to be more mafic (basaltic andesites to basalts) and have approximate tholeiitic magma signatures. However, directly before the start of the 2018 eruption, two long-period earthquakes were sensed at depths of 19 and 16 km, suggesting that these tholeiitic systems within the Aleutian arcs may have deeper assembly than the regional models predict.

Extensive interdisciplinary geophysical and petrologic work completed along the Aleutian Arc has highlighted the link between magma chemistry and local and regional tectonics of the arc (Buurman et al., 2014; Larsen et al. 2016). Edifices that typically erupt tholeiitic magma (i.e., Okmok, Seguam) tend to exist in extensional stress regime environments, where magma travels with little impediment and ponds at shallower depths. Erupted magma tends to be more mafic, crystal poor, and lower in water content. On the other hand, edifices that tend to produce more calc-alkaline magmas (i.e., Augustine) trend towards more compressional stress environments. Magma migration is impeded, producing a protracted, polybaric storage network beneath the edifices. Magma crystallization occurs at lower depths, leading to more crystal rich magmas that are potentially higher in water content. However, due to the trans-crustal storage nature, these magmas tend to be more evolved than the extensional counterparts. Due to slow

ascent, melt inclusions trapped in these systems may experience re-equilibration at the P-T-X conditions of where magma was stored prior to eruption.

Qualitative models based on the textures of clinopyroxene and olivine growth in magmas from the 2018 eruption described by Loewen et al. (2021) also support mid-crustal storage prior to the eruption. Through experimental work, Blatter et al. (2013) showed that the stability of clinopyroxene increases with pressure and can crystallize prior to olivine at high pressures (>800 MPa). Textures observed in clinopyroxene and olivine grains (i.e., anhedral clinopyroxene grains with sieved cores) from this study and Loewen et al. (2021) are in accordance with early crystallization of clinopyroxene and olivine, as we find both grains growing together. Magma was then mobilized to shallower storage where clinopyroxene was destabilized and olivine grew.

Prolonged storage and recycling is not only supported by the presence of geochemically related plutonic xenoliths (Bacon, 2007) but also mineral scale evidence in the 2018 eruption indicating that crustal cumulates are remobilized during magma ascent. Insignificant variation in major and minor elements of the host olivine consistent with prolonged diffusive equilibration over hundreds to thousands of years in distinct but compositionally and thermally buffered environments (Winslow et al., 2020). This is consistent with olivine analysis from Loewen et al. (2021), in which they observed olivine core compositions of Fo_{67-78}, with thin rims as low as Fo_{60}. The high Ni/Cr ratios in olivine from some tephra samples of the 2018 eruption are inconsistent with regular magmatic fractionation trends (Oeser et al., 2018; Ruprecht & Plank, 2013) that instead leads to low

Ni/Cr ratios <50. During fractionation, Ni and Cr are simultaneous removed from the melt by olivine (Ni) as well as by spinel and clinopyroxene (Cr). The high Ni/Cr ratio are a result of both high Ni contents (>2000 ppm) at intermediate Fo content and coeval low Cr (<50 ppm). We explain this by diffusive equilibration Kd between olivine and clinopyroxene in a cumulate with large distribution coefficients between olivine and clinopyroxene for Ni and low Kd for Cr (Otamendi et al, 2016; Oeser et al, 2018). Textures of clots of olivine and pyroxene have been observed in tephra from the 2018 eruption (Loewen et al., 2021) and previous historic eruptions at Mount Veniaminof (Bacon, 2007); however, those direct assemblages have yet to be analyzed to substantiate this model. This disparity in Cr concentrations in the grains with MIs and earlier measured olivine grains is probably due to host olivine grains analyzed for melt inclusion work were predominantly single crystal grains, while previous trace element work included multiple grain clusters.

6.3 6.3 Comparisons with Along Arc Trends

The Aleutian-Alaskan subduction zone has been the locus of many studies linking geochemical tracers of slab and mantle inputs (Plank, 2005; Plank et al, 2013 Yogodzinski et al., 2015, Jicha and Kay, 2018, Wei et al., 2021). Cooper et al. (2012) and Plank et al. (2013) showed an anti-correlation between Nb/Ce and H_2O/Ce, reflecting that volatile melt inclusion data retain information about the region of magma genesis. Higher Nb represents more influence in the mantle wedge, and higher Ce ratios indicate greater contribution of slab melt

(Cooper, 2012; Plank et al. 2014). Olivine-hosted MI utilized in this study were from variably evolved systems (Shishaldin (~$Fo_{70–72}$) to Pakushin ($Fo_{86.7–88.7}$). In the AASZ, edifices with high measured water contents, like Augustine, tend to have lower Nb/Ce ratios or are edifices that are moderately hydrous with lower Ce, such as Seguam. On the other hand, edifices with lower water contents, such as Shishaldin (average 2.37 wt.% H_2O, Cooper et al. 2012), and high Ce values tend to have higher amounts of Nb and thus higher Nb/Ce ratios and low H_2O/Ce ratios.

Based on trace element data of the melt inclusions, Mount Veniaminof has higher Nb concentrations (on average ~6.36 ppm) and higher Ce measurements (on average 33.8 ppm), leading to a Nb/Ce ratio at 0.188 (**Figure 3.12**). Since Ce is already established as higher, with this ratio, H_2O concentrations around 1-2 wt.% are expected. Using the maximum direct H_2O concentrations from melt inclusions at Mount Veniaminof of 2.41 wt.%, Mount Veniaminof seemingly fits the regional trend expected. However, even when accounting for a maximum pre-eruptive water content up to 6.3 wt.% H_2O predicted using the Ca-in-olivine hygrometer, Mount Veniaminof still reasonably fits the regional trend predicted using this relationship, begging the question how sensitive this ratio is at higher concentrations of Ce. We performed a sensitivity analysis of Ces values from 0–50 ppm and H_2O concentrations from 0–9.0wt.%, where melt inclusions may not quench into a glass (Gavrilenko et al., 2019). At lower Ce values, like observed at Seguam, H_2O concentrations exerts more control. However, at Ce concentrations >20 ppm, this relationship is more sensitive to Ce. Even with H_2O

concentrations up to 9.0 wt.%, at Ce concentrations >25 ppm, those potential melt inclusions fit the regional trend.

6.4 6.4 Drivers for eruption dynamics

While we observe a wide range of volatile contents (0.2–2.4 wt% H_2O; bdl–2815 ppm CO_2) for each eruptive unit, a similar trend is observed in each tephra unit. Not including Raman spectroscopy analyses of the shrinkage bubbles, AT-4593 has a higher maximum CO_2 measurement reaching up to 2815 ppm, but when including CO_2 from bubble estimates, CO_2 estimates for units in AT-4598 (the beginning of the eruption) and AT-4596 (the midst of the eruption) are further elevated from 1080 ppm CO2 to 2177 ppm CO2 and up to 1550 ppm, for the respective units. Changes to volatile content during the eruption did not cause the November, paroxysmal event. However, a similar range of volatile concentrations throughout the eruption could point to open system behavior where magma from different storage areas is mobilized throughout the eruption. The cause of the increase in explosivity has instead been attributed to an increase in tachylite proportions through the November explosive event. This groundmass texture has been attributed to formation along the conduit margins, where shearing and fragmentation lead to the increase in ash emissions (Loewen et al., 2021). Alternatively, a recent model of a bifurcating conduit underneath Veniaminof leading to simultaneous effusive and explosive eruptions at Mount Veniaminof has emerged, where gas-magma segregation could lead to an increase of explosivity (Waythomas et al., 2022).

Geophysical research and gas flux during the eruption Mount Veniaminof supports arguments for open-system behavior. The 2018 eruption at Mount Veniaminof was only directly preceded by two long period earthquakes (Loewen et al., 2021; Waythomas et al, 2021). Lack of precursory signals prior to eruption is not limited to the 2018 eruption (Bennington et al., 2018; Li et al., 2022). Moreover, simultaneous explosive and effusive eruptions during the 2018 eruption point to shallow branching volcanic conduits leading to gas segregation possibly causing increases in explosivity during the 2018 eruption (Waythomas et al., 2022).

Generally, volatile measurements from the 2018 eruption do not follow any degassing pathway calculated using average melt inclusion major element compositions from the 2018 eruption and maximum volatile concentrations. There are a large population of melt inclusions with high CO_2 measurements and low H_2O concentrations (Fig. 8). Such trends could be created by variable processes, such as flushing of deep-seated hot CO_2-rich magmas and fluids (i.e., Mount Saint Helens, Stromboli, Merapi; Caricchi et al., 2018) or by large degrees of diffusive loss of H_2O through the mineral hosts. Hydrogen isotope data from inclusions in the 2018 eruption point to moderately heavy inclusions (δD_{SMOW} ~50), except for one heavy inclusion (δD_{SMOW} ~280) and two moderately light inclusions (δD_{SMOW} -30) (Figure 9). While CO_2 flushing can be a cause in generating paroxysmal events at Stromboli and other similar edifices (Caricchi et al., 2018) increases in CO_2 leading up to the November explosive event at Veniaminof would be expected and is not observed in melt inclusion data.

Instead, the moderately heavy inclusions point to melt inclusions that are degassed.

7. Conclusions

During the 2018 eruption at Mount Veniaminof, we observe little change in volatile concentration, major and trace elements through each tephra layers leading to the November explosive event. The olivine hosts of the melt inclusions are evolved compositions, further evidence that these inclusions that are not representative of primary conditions. However, these melt inclusions point to deeper storage of magma prior to eruption that coincides with the two precursory long-period earthquake depths at 16 and 19 km. Models of magma storage for this volcano are sparse (Bacon, 2007), so this study provides valuable insights about magma storage at Mount Veniaminof.

The volatile budget derived from melt inclusions are already minimum estimates, because CO_2 was lost to shrinkage bubbles and mineral precipitates along the bubble-melt inclusion interface. Comparisons with other hygrometers and corrections point to magma that is similar to the maximum H_2O estimates from melt inclusions, such as the Waters and Lange (2015) plagioclase hygrometer and the Tholeiitic index (Zimmer et al., 2010), or demonstrably higher, such as from the joint Si-H_2O correction (Portnyagin et al., 2019) and Ca-in-olivine hygrometer (Gavrilenko et al., 2016). While the upper limits of H_2O

concentrations are extreme, they point to magma that has lost H_2O after entrapment.

While the Aleutian Arc has been widely studied, this study provides insights into the volatile budget for a section of the AASZ that had previous been overlooked. Data from trace elements concentrations of the melt inclusions fit regional trends of H_2O/Ce and Nb/Ce. However, at higher Nb/Ce ratios, the role of H_2O driving trends in the H_2O/Ce ratio becomes less apparent. Further investigation into this phenomenon is warranted.

ACKNOWLEDGEMENTS

This study is supported by a National Science Foundation (NSF) grant (NSF EAR 2147714). We thank Rick Hervig, Lynda Williams, and Megan Guild for help with SIMS analyses, as well as Joel DesOrmeau at UNR for EPMA and LA-ICP-MS analyses.

TABLES

Table 3.1: EPMA and SIMS measurement of MIs, Fo content of the host olivine, and PEM calculated via both petrolog3.1 and MIMic**.**

SAMPLE	Fo #	SiO2	1σ	TiO2	1σ	Al2O3	1σ	FeO	1σ	MnO	1σ	MgO	1σ	CaO	1σ	Na2O	1σ	P2O5	1σ	K2O	1σ	TOTAL	H2O	Co2	CO2 bub	F	P	S	Cl	PEM Petrolog	PEM_MIMic
AT-4591 OI 7	72.64	55.77	0.18	1.66	0.02	17.26	0.10	9.96	0.07	0.20	0.02	3.67	0.03	7.36	0.05	4.48	0.08	0.33	0.02	1.23	0.02	102.22	0.39	181.90		451.47	1567.70	1229.34	934.10	-4.24	-0.74
AT-4593 OI 12	78.24	51.05	0.18	1.34	0.02	17.72	0.10	8.52	0.06	0.15	0.02	4.14	0.03	9.03	0.05	3.66	0.07	0.31	0.02	0.83	0.01	97.14	1.72	142.70	1577.31	559.29	1365.24	1312.17	1104.85	-2.60	-0.25
AT-4593OI 13	72.77	50.69	0.18	1.38	0.02	15.99	0.10	11.31	0.07	0.21	0.02	5.49	0.03	7.79	0.05	3.78	0.07	0.35	0.02	0.97	0.02	98.15	1.27	165.31		317.81	1110.09	1141.46	684.21	1.40	-5.06
AT-4593_OI 14_MI	75.76	47.18	0.17	1.36	0.02	18.21	0.10	10.82	0.07	0.19	0.02	4.49	0.03	9.76	0.06	3.34	0.07	0.31	0.02	0.59	0.01	96.72	1.31	401.13	879.44	545.77	1010.10	1886.38	846.77	-1.96	0.24
AT-4593_OI 14_MI	74.74	51.03	0.18	1.34	0.02	17.44	0.10	10.22	0.07	0.17	0.02	3.98	0.03	8.57	0.05	3.70	0.07	0.37	0.02	0.95	0.02	98.13	1.67	505.67		590.40	1373.79	2627.40	987.22	-3.20	0.41
AT-4593_OI 17	72.78	53.79	0.18	1.40	0.02	16.18	0.10	10.08	0.07	0.18	0.02	3.39	0.03	7.44	0.05	4.29	0.08	0.30	0.02	1.00	0.02	98.51	1.01	129.67	591.38	430.00	1188.30	1041.76	742.61	-3.95	0.94
AT-4593_OI 18	73.05	51.63	0.18	1.50	0.02	16.06	0.09	10.06	0.07	0.21	0.02	3.54	0.03	7.87	0.05	3.83	0.07	0.33	0.02	0.97	0.02	96.47	1.18	152.84	798.08	565.38	1134.80	1158.93	886.75	-2.79	0.64
AT-4593_OI 19	72.42	53.97	0.18	1.62	0.02	15.15	0.09	9.31	0.06	0.17	0.02	3.14	0.02	6.92	0.05	3.77	0.07	0.42	0.02	1.21	0.02	95.88	0.88	69.92	661.94	482.54	1605.48	418.01	1063.94	-0.22	2.59
AT-4593_OI 20	72.17	56.42	0.18	1.59	0.02	16.33	0.09	9.47	0.07	0.20	0.02	2.92	0.03	7.24	0.05	3.89	0.07	0.36	0.02	1.22	0.02	99.82	0.87	22.02		408.72	1390.45	245.35	800.45	-1.66	3.95
AT-4593_OI 72	72.62	55.48	0.18	1.82	0.02	14.36	0.09	10.24	0.07	0.22	0.02	2.78	0.02	6.50	0.05	3.95	0.07	0.45	0.02	1.61	0.02	97.59	0.63	8.40		824.11	1715.47	266.79		-2.42	4.77
AT-4593_OI 73	78.29	52.65	0.18	1.39	0.02	17.35	0.10	8.51	0.06	0.15	0.02	3.95	0.03	8.42	0.05	3.54	0.07	0.37	0.02	0.96	0.02	97.64	1.70	2026.48		372.98	1177.73	1231.76		-3.87	1.09
AT-4593_OI 75	72.76	55.42	0.18	1.70	0.02	15.26	0.09	9.18	0.06	0.18	0.02	3.26	0.03	6.81	0.05	4.04	0.07	0.38	0.02	1.35	0.02	97.78	1.24	2904.55		531.57	1318.06	430.43		-0.37	3.12
AT-4593_OI 76	72.75	54.64	0.18	1.60	0.02	15.20	0.09	9.16	0.06	0.18	0.02	3.58	0.03	6.83	0.05	3.89	0.07	0.36	0.02	1.29	0.02	96.93	1.87	47.91		681.43	1695.50	604.84	1180.52	0.36	0.99
AT-4593_OI 77	77.60	53.15	0.18	1.47	0.02	17.85	0.10	8.39	0.06	0.16	0.02	3.61	0.03	8.19	0.05	3.97	0.07	0.29	0.02	1.13	0.02	98.55	1.24	110.23		596.06	1160.73	1197.14		-4.29	0.78
AT-4593_OI 78	72.04	53.68	0.18	1.54	0.02	15.24	0.09	10.02	0.07	0.20	0.02	3.99	0.03	7.13	0.05	3.60	0.07	0.39	0.02	1.09	0.02	97.05	1.29	665.66		561.43	1458.28	494.01		0.42	-1.47
AT-4593_OI 79	72.51	54.15	0.18	1.63	0.02	15.17	0.09	9.05	0.06	0.20	0.02	3.16	0.03	7.48	0.05	3.65	0.07	0.41	0.02	1.24	0.02	96.33	0.95	41.34		641.93	1557.15	617.43		-0.29	2.11
AT-4593_OI 80	72.59	56.44	0.18	1.57	0.02	15.67	0.09	9.57	0.07	0.21	0.02	3.77	0.04	7.12	0.05	4.32	0.07	0.32	0.02	1.22	0.02	100.39	1.43			523.17	1375.03	460.72		-0.06	0.67
AT-4593_OI 81	72.70	54.20	0.18	1.59	0.02	15.28	0.09	9.68	0.06	0.21	0.02	3.24	0.03	7.23	0.05	4.00	0.07	0.36	0.02	1.32	0.02	97.33	0.69	54.79		536.39	1365.69	559.59		-1.04	0.90
AT-4593_OI 82	77.55	52.37	0.18	1.56	0.02	16.01	0.10	8.17	0.06	0.15	0.02	3.48	0.03	8.53	0.05	3.56	0.07	0.30	0.02	1.07	0.02	95.53	1.54	451.97		550.31	1145.01	1080.20		-3.36	1.21
AT-4593_OI 83	78.21	50.97	0.18	1.37	0.02	17.18	0.10	9.00	0.06	0.16	0.02	4.30	0.03	8.40	0.05	3.68	0.07	0.35	0.02	0.88	0.02	96.67	1.51	841.74		411.39	1185.61	1399.32		-3.16	0.27
AT-4593_OI 84	72.20	55.00	0.18	1.68	0.02	15.63	0.10	9.46	0.06	0.21	0.02	3.15	0.02	7.23	0.05	3.51	0.07	0.42	0.02	1.31	0.02	97.81	0.92	698.20		620.43	1568.84	785.59	1068.64	-0.86	2.69
AT-4593_OI 85	78.13	52.93	0.18	1.16	0.02	17.37	0.10	9.11	0.07	0.17	0.02	4.85	0.04	8.17	0.05	3.76	0.07	0.22	0.02	0.75	0.01	98.58	1.11	1025.30		402.17	732.20	1362.08		-2.16	-1.50
AT-4593_OI 86	72.65	55.74	0.18	1.67	0.02	15.16	0.09	8.78	0.06	0.17	0.02	3.44	0.03	6.64	0.05	3.95	0.07	0.38	0.02	1.36	0.02	97.47	1.89	1479.86		663.09	1601.52	441.93	1164.32	0.28	1.10
AT-4595_OI 22	77.26	50.87	0.18	1.42	0.02	17.86	0.10	9.32	0.06	0.16	0.02	3.99	0.03	8.89	0.05	3.72	0.07	0.37	0.02	0.88	0.02	97.85	1.09	162.92		548.37	1605.54	1578.15	986.24	-3.12	0.87
AT-4595_OI 87	72.70	52.46	0.18	1.52	0.02	15.26	0.09	9.88	0.07	0.19	0.02	3.49	0.03	7.98	0.05	3.57	0.07	0.34	0.02	1.08	0.02	96.08	1.67	394.75		687.06	1364.16	1011.81	992.10	-2.80	0.62
AT-4595_OI 89	75.44	50.29	0.18	1.29	0.02	16.81	0.10	9.30	0.06	0.17	0.02	4.03	0.03	8.67	0.05	3.38	0.07	0.28	0.02	0.73	0.01	95.32	2.03	255.45		525.25	1251.77	1757.34	1009.45	-1.77	-0.35
AT-4596_OI 23	72.47	51.75	0.18	1.61	0.02	15.96	0.10	10.79	0.07	0.25	0.02	2.96	0.02	8.39	0.05	3.75	0.07	0.38	0.02	0.96	0.02	97.67	1.29		950.39	825.24	1623.49	2158.56	2581.15	-5.17	4.31
AT-4596_OI 25	72.67	52.38	0.18	1.47	0.02	15.75	0.10	10.71	0.07	0.21	0.02	4.35	0.03	7.35	0.05	3.68	0.07	0.32	0.02	1.00	0.02	97.87	0.68	94.32	115.62	288.78	860.01	693.39	479.25	-1.75	-1.77
AT-4596_OI 26	71.53	53.76	0.18	1.61	0.02	16.33	0.09	9.63	0.07	0.20	0.02	3.76	0.03	7.77	0.05	3.76	0.07	0.37	0.02	1.21	0.02	98.64	0.37	87.30		569.26	1394.18	662.14	1033.71	-1.49	-1.99
AT-4596_OI 28	72.89	50.61	0.18	1.46	0.02	16.88	0.10	10.53	0.07	0.21	0.02	3.81	0.03	8.23	0.05	3.79	0.07	0.33	0.02	0.87	0.02	97.23	1.40	207.89		606.22	1380.33	1665.16	990.53	-3.20	0.20
AT-4596_OI 32	72.71	52.28	0.18	1.70	0.02	16.60	0.10	10.00	0.07	0.22	0.02	3.30	0.03	7.75	0.05	3.84	0.07	0.36	0.02	1.25	0.02	97.56	0.25	85.38	669.75	468.14	1260.26	861.85	866.66	-3.03	1.02
AT-4596_OI 34	72.52	53.58	0.18	1.70	0.02	16.06	0.10	10.04	0.07	0.20	0.02	3.13	0.03	7.65	0.05	4.01	0.07	0.33	0.02	1.29	0.02	98.27	0.40	93.76	682.55	600.64	1424.43	842.89	1001.73	-4.65	1.70
AT-4596_OI 35	72.46	53.52	0.18	1.48	0.02	17.01	0.10	9.94	0.07	0.22	0.02	3.28	0.03	8.04	0.05	4.04	0.07	0.35	0.02	1.07	0.02	99.26	0.82	354.78	1161.29	572.22	1171.67	1176.46	913.02	-4.08	0.99
AT-4596_OI 36	72.80	53.63	0.18	1.58	0.02	15.92	0.10	10.09	0.07	0.18	0.02	3.98	0.03	7.41	0.05	3.88	0.07	0.32	0.02	1.24	0.02	98.45	0.38		419.78	541.48	1371.71	635.34	1085.17	-3.07	-1.43
AT-4596_OI 37	74.27	50.22	0.18	1.33	0.02	17.66	0.10	10.70	0.07	0.20	0.02	4.23	0.03	9.01	0.05	3.53	0.07	0.25	0.02	0.84	0.01	98.27	0.65	183.68	1329.39	375.89	1155.32	1720.51	787.86	-2.03	-0.25
AT-4596_OI 38	72.72	53.49	0.18	1.63	0.02	16.02	0.10	9.46	0.07	0.17	0.02	3.29	0.03	7.63	0.05	3.91	0.07	0.35	0.02	1.25	0.02	97.42	0.31	91.76		601.74	1462.06	618.09	1013.11	-1.47	0.24
AT-4596_OI 39	72.87	53.99	0.18	1.52	0.02	16.08	0.10	10.05	0.07	0.22	0.02	3.41	0.03	7.52	0.05	3.94	0.07	0.35	0.02	1.07	0.02	98.45	1.30	467.28	971.00	511.98	1320.60	988.71	800.37	-4.00	1.17
AT-4596_OI 40	71.94	55.49	0.18	1.61	0.02	15.86	0.10	10.09	0.07	0.20	0.02	3.56	0.03	7.06	0.05	4.06	0.07	0.35	0.02	1.23	0.02	99.74	0.88	193.69		561.13	1739.51	579.82	988.00	-0.68	0.34
AT-4596_OI 41	78.51	48.85	0.17	1.23	0.02	17.49	0.10	9.67	0.06	0.18	0.02	4.73	0.03	9.14	0.05	3.32	0.07	0.28	0.02	0.70	0.01	96.03	2.41	1565.12		488.70	1205.16	2244.47	967.14	-2.44	0.72
AT-4596_OI 42_MI	72.72	54.08	0.18	1.64	0.02	14.99	0.09	9.38	0.07	0.19	0.02	3.82	0.04	6.81	0.04	3.73	0.07	0.37	0.02	1.33	0.02	96.53	1.48	222.60		568.35	1509.84	578.36	1038.00	0.91	0.36
AT-4596_OI 46	72.58	57.43	0.18	1.63	0.02	16.39	0.09	9.72	0.06	0.20	0.02	3.45	0.03	6.95	0.05	4.43	0.07	0.41	0.02	1.35	0.02	102.14	0.28	73.50		504.34	1600.13	312.07	711.69	-0.94	2.24
AT-4597 OI48	72.37	57.07	0.19	1.64	0.02	15.91	0.10	9.77	0.06	0.20	0.02	3.13	0.03	7.51	0.05	4.14	0.07	0.36	0.02	1.17	0.02	101.10	1.17	138.84		639.71	1610.00	424.10	798.09	-1.85	3.11
AT-4598_OI50	72.35	51.93	0.18	1.23	0.02	16.67	0.10	10.77	0.07	0.19	0.02	4.01	0.03	8.40	0.05	3.93	0.07	0.25	0.02	0.86	0.02	98.60	1.33	280.87	1905.70	594.03	1163.64	1394.23	660.66	-2.52	-0.64
AT-4598_OI51	71.63	53.95	0.18	1.68	0.02	14.91	0.09	11.48	0.07	0.23	0.02	4.27	0.03	6.41	0.05	3.89	0.07	0.40	0.02	0.98	0.02	98.66	2.09	93.70	958.13	683.20	1848.53	3085.69	996.50	-3.92	-0.83
AT-4598_OI52	73.64	50.36	0.17	1.11	0.02	17.64	0.10	10.50	0.07	0.21	0.02	3.97	0.04	8.68	0.05	2.82	0.06	0.29	0.02	0.71	0.01	96.73	1.27	452.62	1516.06	418.41	939.76	1406.20	562.42	-2.27	0.79
AT-4598_OI53	72.56	55.45	0.18	1.35	0.02	16.59	0.10	10.45	0.07	0.22	0.02	4.04	0.03	7.44	0.05	4.41	0.08	0.34	0.02	1.01	0.02	101.63	1.40	265.98	716.15	568.92	1210.84	1691.80	654.37	-3.72	-1.20
AT-4598_OI54	72.46	53.91	0.18	1.37	0.02	16.43	0.10	10.32	0.07	0.21	0.02	3.82	0.03	7.39	0.05	4.28	0.08	0.30	0.02	0.97	0.02	99.40	1.23	163.79	1119.29	591.67	1238.46	1217.06	653.06	-3.47	-0.65
AT-4598_OI55	72.46	53.68	0.18	1.54	0.02	16.29	0.10	10.38	0.07	0.20	0.02	4.00	0.03	7.42	0.05	4.07	0.07	0.33	0.02	1.09	0.02	99.37	0.57	278.99	1219.59	493.35	1208.59	1698.03	675.86	-2.54	-1.28
AT-4598_OI56	72.71	51.73	0.18	1.52	0.02	16.82	0.10	10.14	0.07	0.21	0.02	3.42	0.03	8.15	0.05	4.35	0.08	0.38	0.02	0.99	0.02	98.02	0.25		1277.26	321.91	747.45	737.64	459.12	-2.86	0.49
AT-4598_OI57	72.62	54.57	0.18	1.68	0.02	16.10	0.10	8.91	0.06	0.17	0.02	2.98	0.02	7.27	0.05	4.15	0.07	0.43	0.02	1.37	0.02	97.85	0.60	252.00	502.50	660.39	1634.04	646.81	1149.87	-0.45	1.64
AT-4598_OI64	72.74	55.96	0.18	1.53	0.02	15.51	0.10	10.24	0.07	0.19	0.02	3.96	0.03	6.58	0.05	4.23	0.07	0.33	0.02	1.26	0.02	99.98	1.57	59.98		447.89	1378.97	318.64	648.84	-0.46	0.74
AT-4598_OI66	72.60	55.05	0.18	1.57	0.02	15.51	0.09	9.67	0.06	0.22	0.02	3.34	0.03	6.38	0.05	3.74	0.07	0.36	0.02	1.14	0.02	97.19	1.78	18.66		705.60	1506.33	426.77	836.45	-0.97	3.25
AT-4598_OI69	72.60	55.63	0.18	1.58	0.02	15.68	0.10	9.88	0.07	0.18	0.02	3.46	0.03	7.59	0.05	3.90	0.07	0.37	0.02	1.18	0.02	99.69	1.18	247.45		548.11	1430.22	565.18	728.18	-1.29	0.71
AT-4598_OI70	72.42	55.10	0.18	1.62	0.02	15.48	0.09	9.74	0.06	0.19	0.02	3.78	0.03	6.82	0.05	4.03	0.07	0.33	0.02	1.28	0.02	98.57	1.13	158.70		623.56	1712.99	472.95	874.90	0.35	0.70
AT-4598_OI 90	72.68	53.13	0.18	1.45	0.02	15.46	0.10	10.14	0.07	0.19	0.02	3.90	0.03	7.60	0.05	3.75	0.07	0.39	0.02	0.98	0.02	97.34	2.14	191.79		745.82	175.94	1644.34	1155.44	-3.56	-0.61
AT-4598_OI 91	72.43	54.88	0.18	1.63	0.02	14.66	0.09	10.03	0.07	0.19	0.02	3.41	0.03	7.04	0.05	3.69	0.07	0.40	0.02	1.24	0.02	97.38	1.21	99.43		495.36	1465.25	470.62	893.31	-0.84	2.21
AT-4598_OI 92	74.87	53.81	0.18	1.51	0.02	15.57	0.10	9.11	0.06	0.18	0.02	4.05	0.03	7.18	0.05	3.84	0.07	0.34	0.02	1.13	0.02	96.97	1.93	229.63		675.90	1475.70	738.56	989.92	0.87	-0.90
AT-4598_OI 93	72.90	54.13	0.18	1.51	0.02	15.66	0.10	9.84	0.07	0.19	0.02	3.61	0.03	7.35	0.05	3.86	0.07	0.38	0.02	1.26	0.02	98.04	0.90	318.25		690.78	1667.52	48.75	939.28	-0.77	-0.12
AT-4598_OI 95	72.53	53.39	0.18	1.53	0.02	15.25	0.09	10.01	0.07	0.20	0.02	3.72	0.03	7.07	0.05	3.91	0.07	0.34	0.02	1.15	0.02	96.83	1.57	317.90		672.24	1347.80	884.54	851.40	-0.15	0.42
AT-4598_OI 96	71.81	53.87	0.18	1.63	0.02	15.52	0.09	10.75	0.07	0.22	0.02	3.32	0.03	7.47	0.05	3.35	0.07	0.36	0.02	1.17	0.02	97.91	0.76	114.94		621.34	1465.16	660.26	994.21	-4.05	2.17
AT-4598_OI 97	72.73	55.16	0.18	1.54	0.02	15.56	0.09	9.64	0.07	0.19	0.02	3.51	0.03	6.93	0.05	3.29	0.07	0.37	0.02	1.26	0.02	97.68	1.33	288.45		570.32	1207.35	614.97	770.61	-1.17	2.45
AT-4598_OI 98	72.80	54.07	0.18	1.61	0.02	15.26	0.09	9.34	0.06	0.18	0.02	2.98	0.02	7.52	0.05	3.64	0.07	0.39	0.02	1.18	0.02	96.40	0.40	66.87		125.96	392.71	134.10	236.06	-0.71	2.06
AT-4598_OI 99	73.14	53.73	0.18	1.52	0.02	15.18	0.09	10.16	0.07	0.20	0.02	3.70	0.03	7.12	0.05	3.85	0.07	0.33	0.02	1.22	0.02	97.19	0.36	1085.06		164.79	303.67	104.44	166.15	-0.33	0.30
AT-4598_OI 100	72.51	54.81	0.18	1.64	0.02	14.95	0.09	9.04	0.07	0.18	0.02	3.17	0.03	6.97	0.05	3.68	0.07	0.36	0.02	1.26	0.02	96.25	1.39	65.17		525.65	1347.73	418.93	872.03	-0.25	2.52
AT-4598_OI 101	72.22	55.93	0.18	1.68	0.02	15.58	0.09	9.69	0.07	0.19	0.02	3.20	0.03	7.02	0.05	3.71	0.07	0.38	0.02	1.36	0.02	98.93	0.62	68.57		459.13	1123.04	260.43	644.25	-1.00	3.35

[1] Error on the SIMS measurements are calculated via RSD of repeat analyses of secondary standards and are 6.39% CO_2, 3.56% on H_2O, 0.80% on F, 2.07% for P, 1.59% on S, and 7.35% for Cl. Full composition data for both the melt inclusions and host olivine grains are located in SD2.

FIGURES

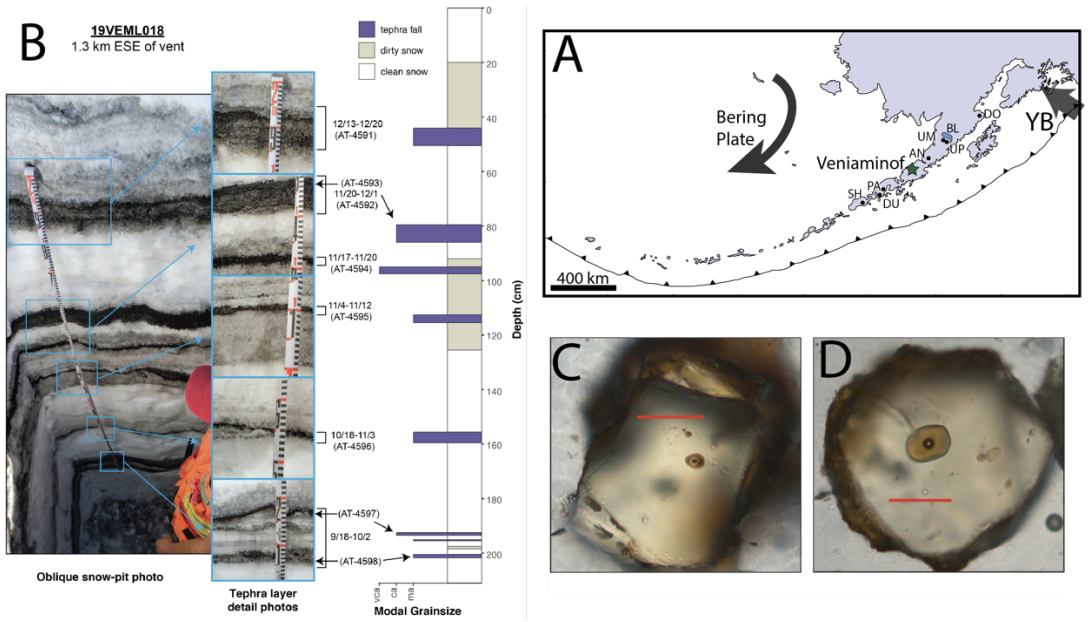

Figure 3.1. Geologic overview and melt inclusions from the 2018 eruption at Mount Veniaminof. **.** (a) Regional setting of Mount Veniaminof in the Alaskan Peninsula. The green star indicates the location of Mount Veniaminof. Other volcanoes along the Alaskan peninsula are denoted by a black dot. DO, Douglas; UM, Ukinrek Maars; UP, Ugashik-Peulik; AN, Aniakchak; PA, Pavlof; DU, Dutton; SH, Shishaldin. Other features on the map include: BL, Becharof Lake. Both the Bering Plate and the Yakutat Block (YB) and vectors denoting motion of these blocks are included. (b) example snow pit where tephra samples were collected from Loewen et al. (2021). Inset displays tephra layers in detail and depth of snow. (c-d) representative olivine grains with melt inclusions measured in this paper. Red scale bar denotes 100 μm.

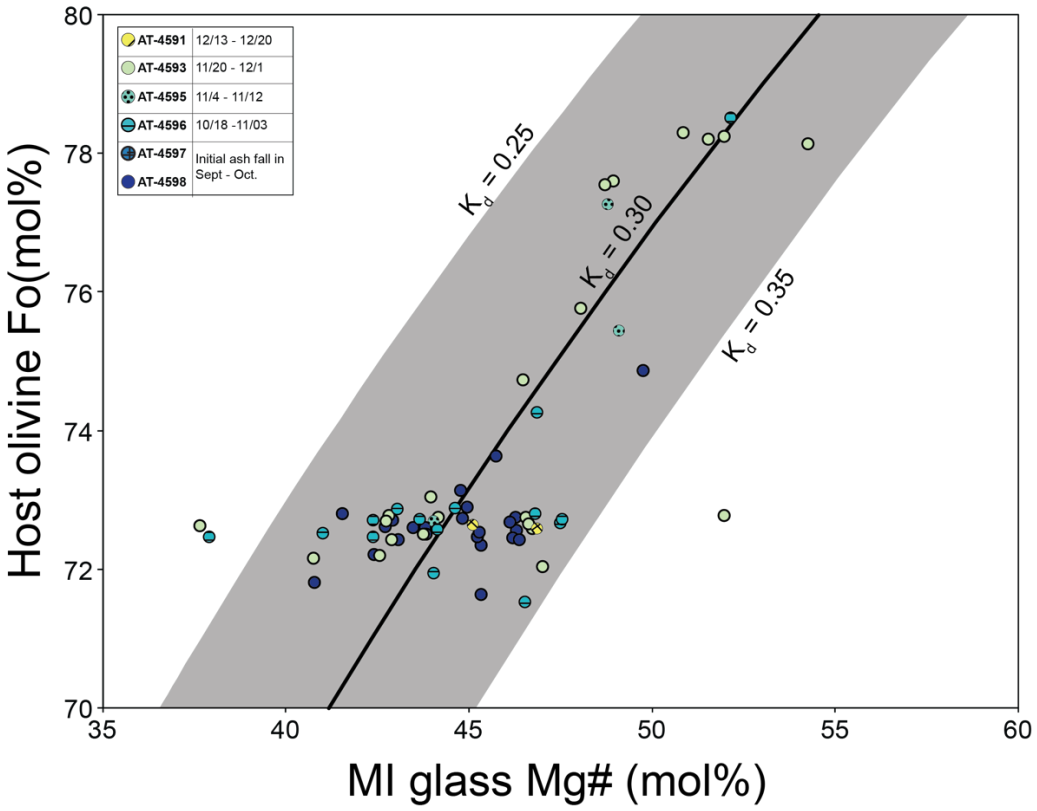

Figure 3.2. Rhodes diagram for melt inclusions and host olivine grains from the 2018 eruption. Forsterite content of the host olivine versus MI glass Mg# using a Fe^{3+}/Fe^{T} = 0.2. Olivine-melt inclusion relationship from EPMA measurements of the host olivine around the melt inclusion and in the inclusions.

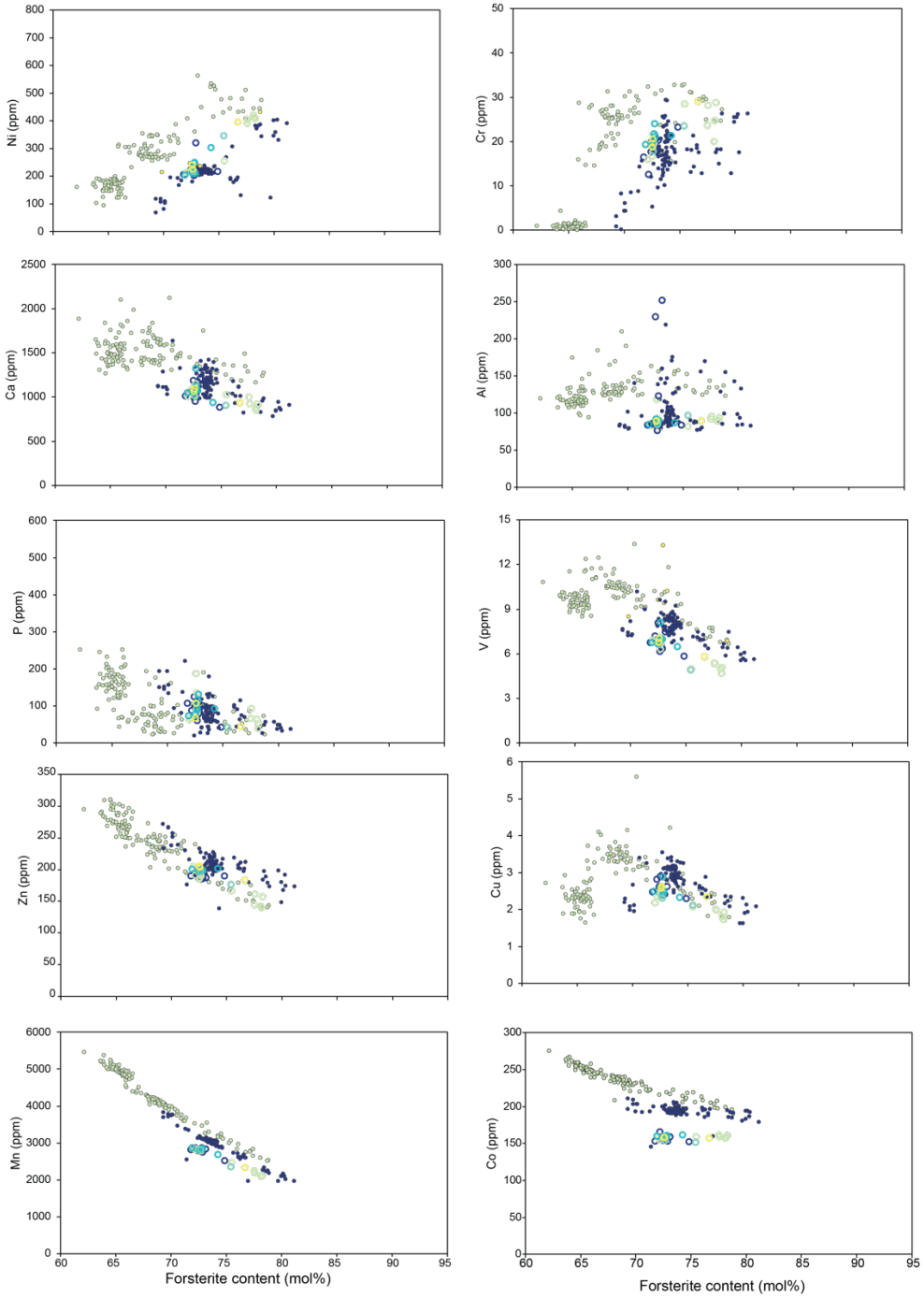

Figure 3.2. Trace elements for olivine grains from Mount Veniaminof.Trace elements for olivine grains from Mount Veniaminof following the color scheme of Figure 3.2. Small, closed circles represent previously collected laser data

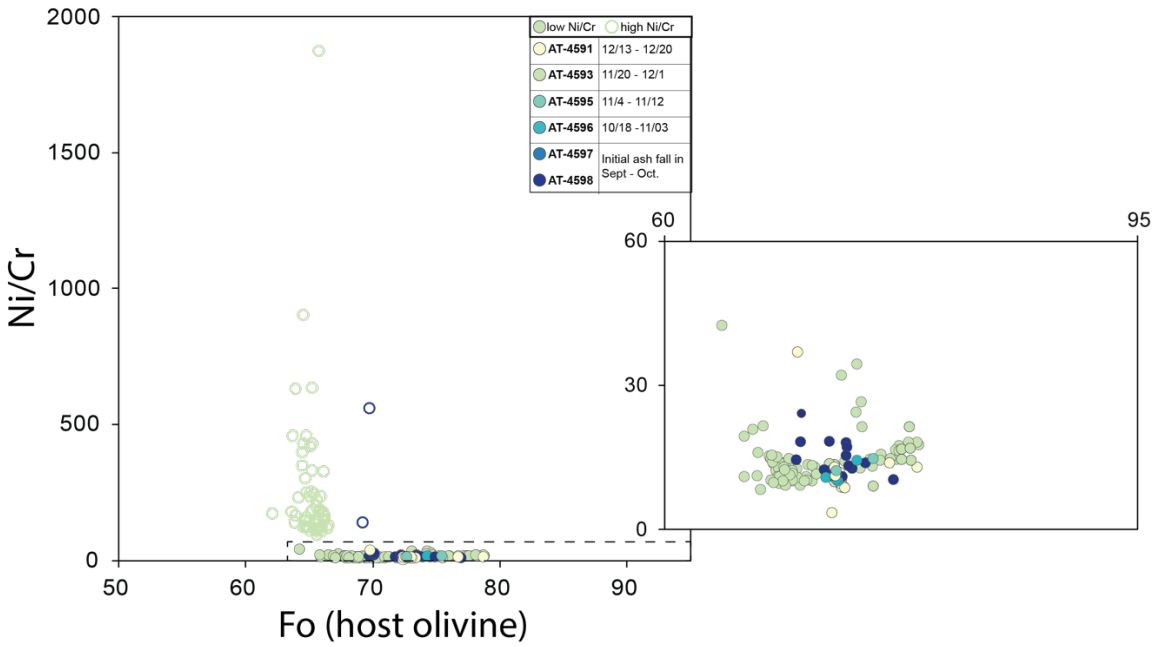

Figure 3.4. Ni/Cr versus Fo for host olivine grains.Color scheme follows previous figures. The inset zooms into the population of olivine grains with low Ni/Cr numbers. In the plot, only grains from AT-4593 have high Ni/Cr ratios, except for two additional points from AT-4598.

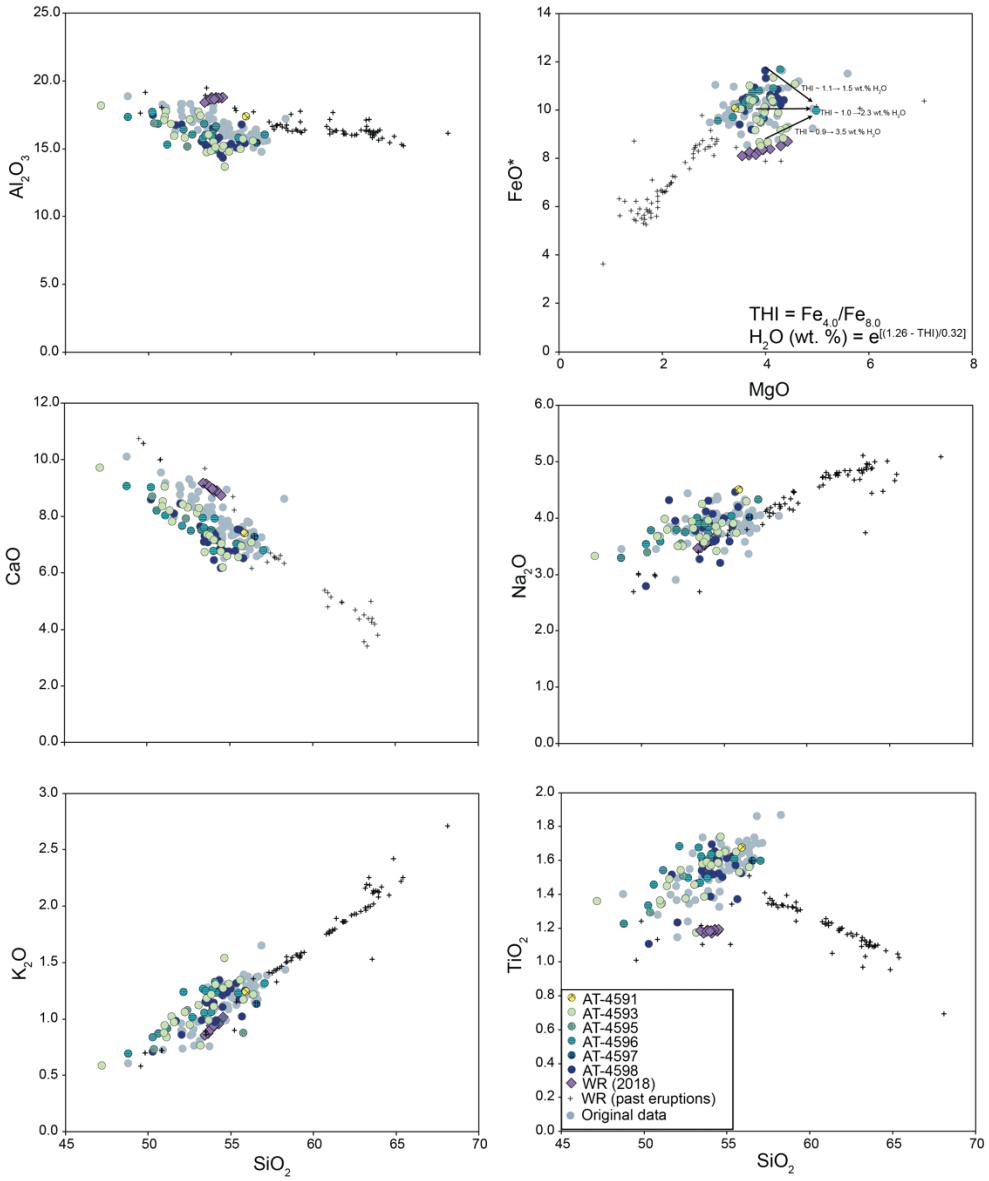

Figure 3.5. Harker diagram for modified melt inclusion data (MIMIC).

Original uncorrected data is presented as more transparent dots. For the plot of FeO vs MgO, the lines demarcate what compositions were chosen for Tholeiitic Index calculations. The data from the 2018 eruption are supplemented with whole rock compositional data from tephra samples from the 2018 eruption obtained from the supplemental documentation of Loewen et al. (2021) and past Veniaminof eruptions from the Alaska Volcano Observatory Geochemical database (Cameron et al., 2019). Whole rock datasets from the AVO Geochemical database span the range of compositional variability of erupted products at Mount Veniaminof. Chosen samples were taken from Kay and Kay (1994) and Wallace et al. (2020).

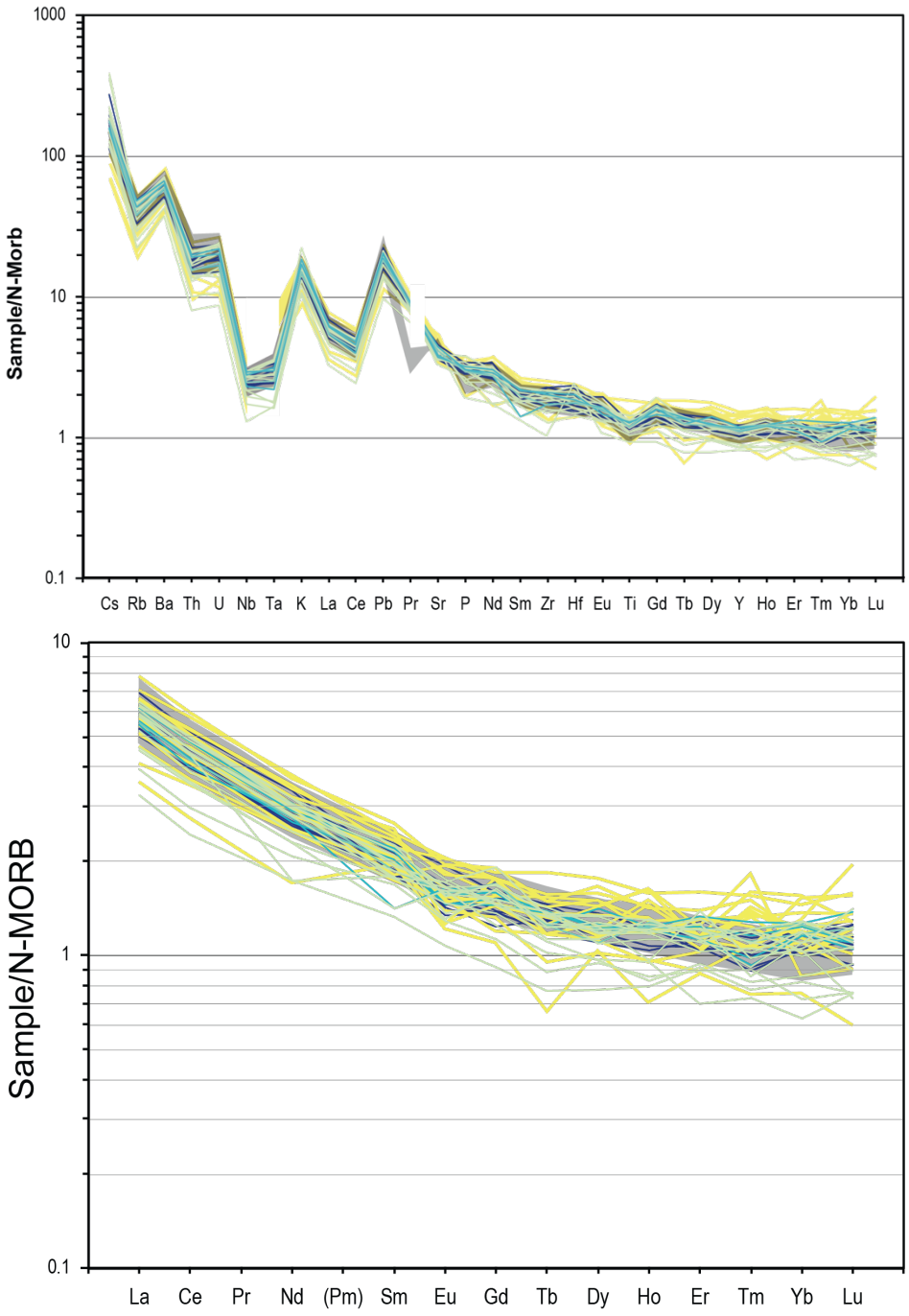

Figure 3.6. Spider diagram of trace elements of melt. Spider diagram of trace elements of melt inclusions collected at UBC and UNR normalized to normal-MORB (N-MORB). Dark grey section are WR XRF measurements from tephra at Mount Veniaminof from Loewen et al. (2021).

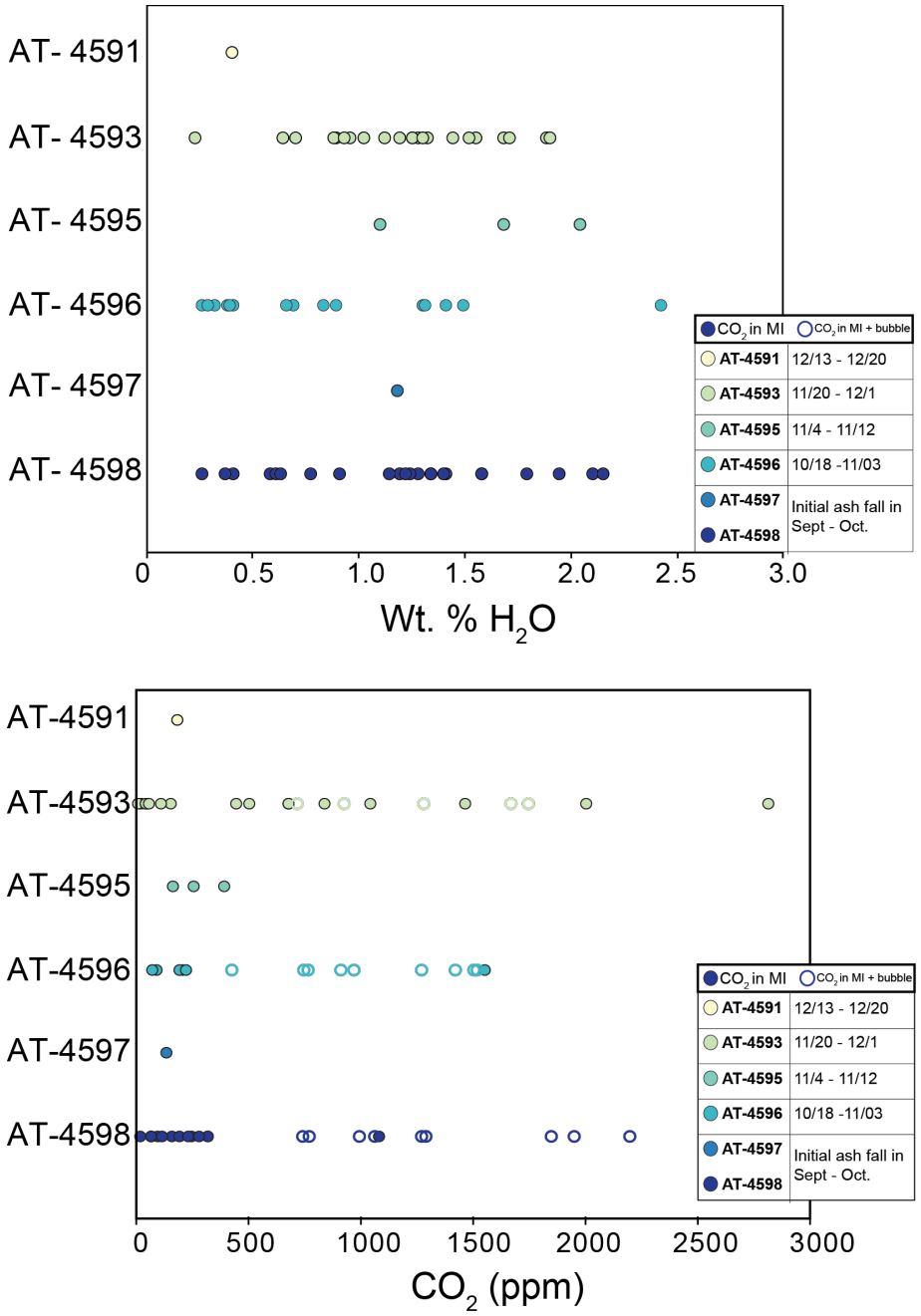

Figure 3.7. CO_2 and H_2O trend for each unit

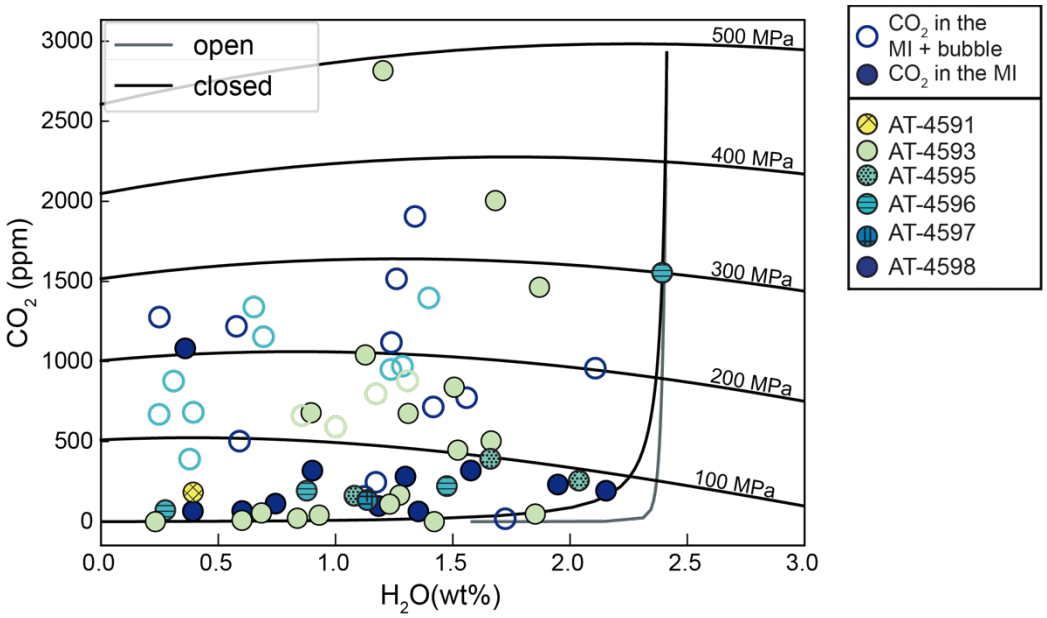

Figure 3.8. CO_2 versus H_2O for melt inclusions at Mount Veniaminof.Degassing pathways and isobars were calculated using Vesical using MagmaSat model. Isobars were calculated based off an average melt inclusion composition for Mount Veniaminof. Closed circles are data with CO_2 measurements of just the melt inclusion and open circles refer to measurements of the vapor bubble and melt inclusions. Isobars calculated off of average melt inclusion compositions..

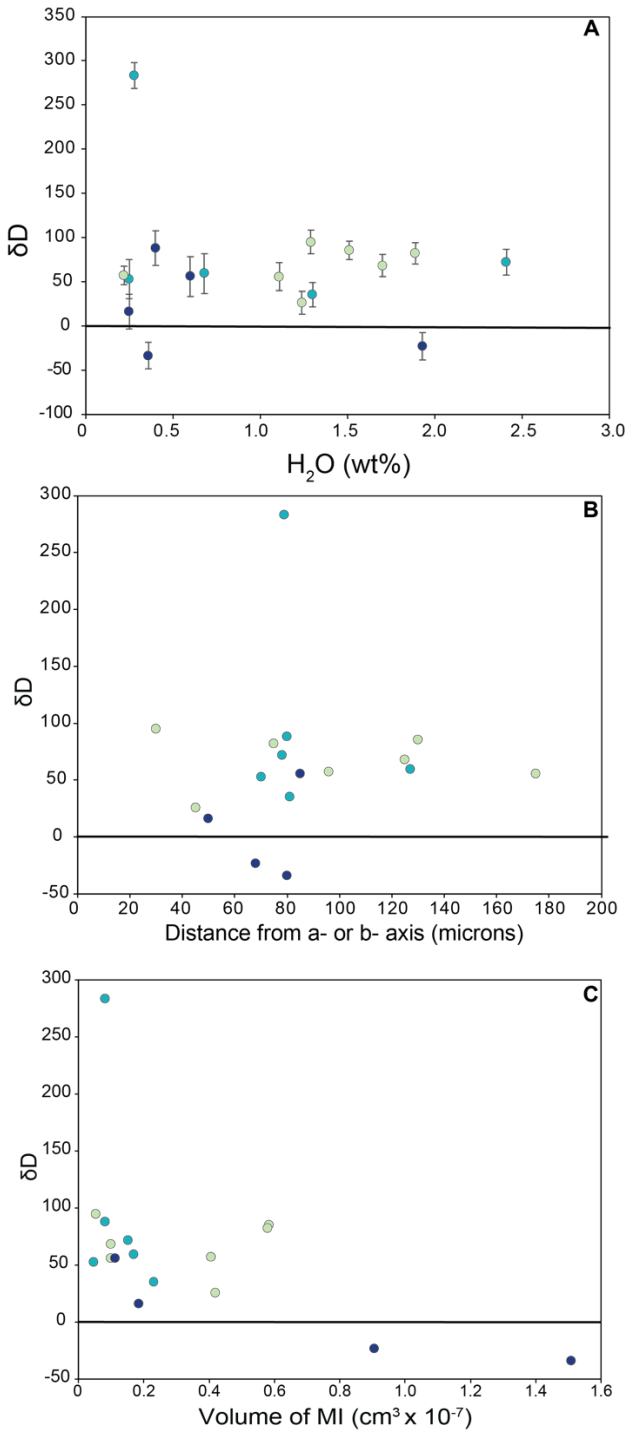

Figure 3.9. δD ratios for select melt inclusions at Veniaminof δD ratios for select melt inclusions at Veniaminof using the same color scheme as previous figures. δD vs distance from a- or b-axis and δD with respect to volume of melt inclusions

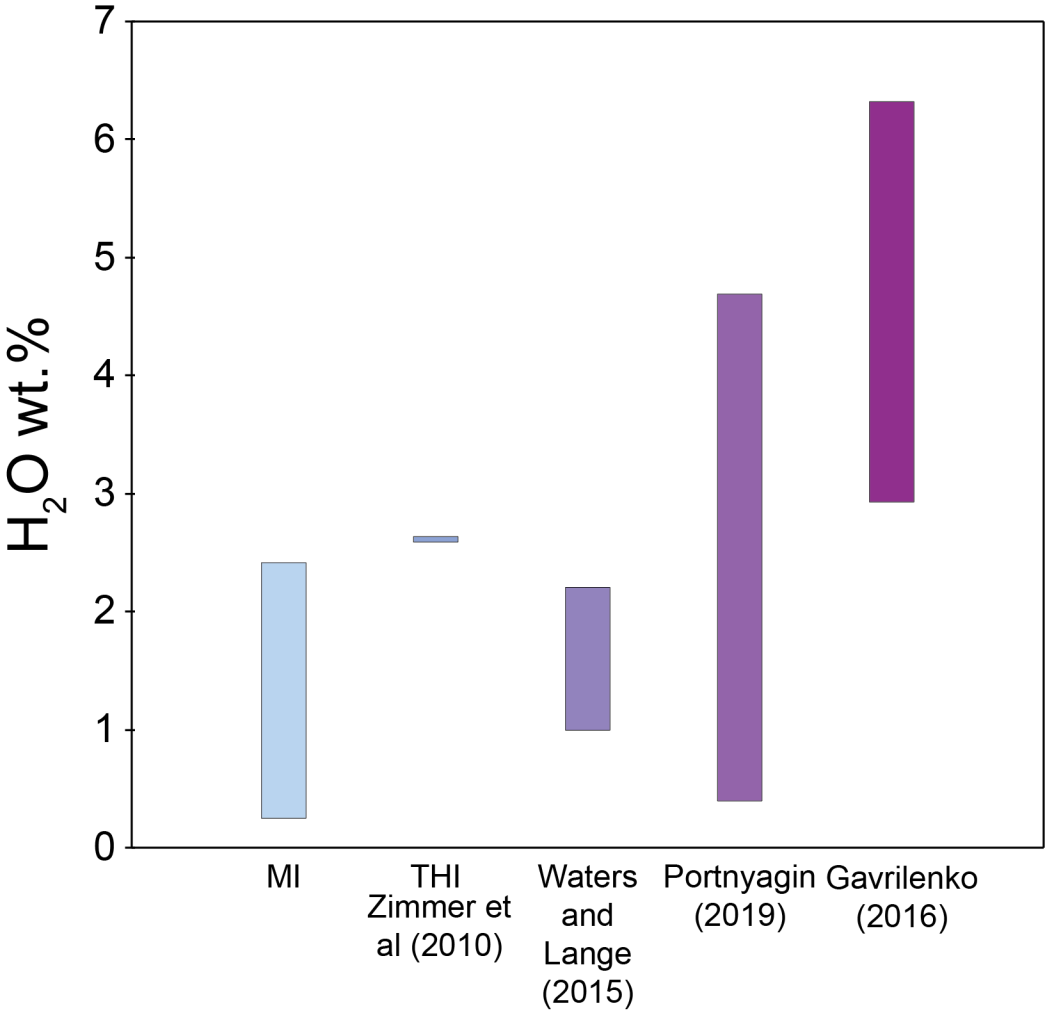

Figure 3.10. A comparison of the range of H_2O concentrations from different hygrometers presented in this chapter.

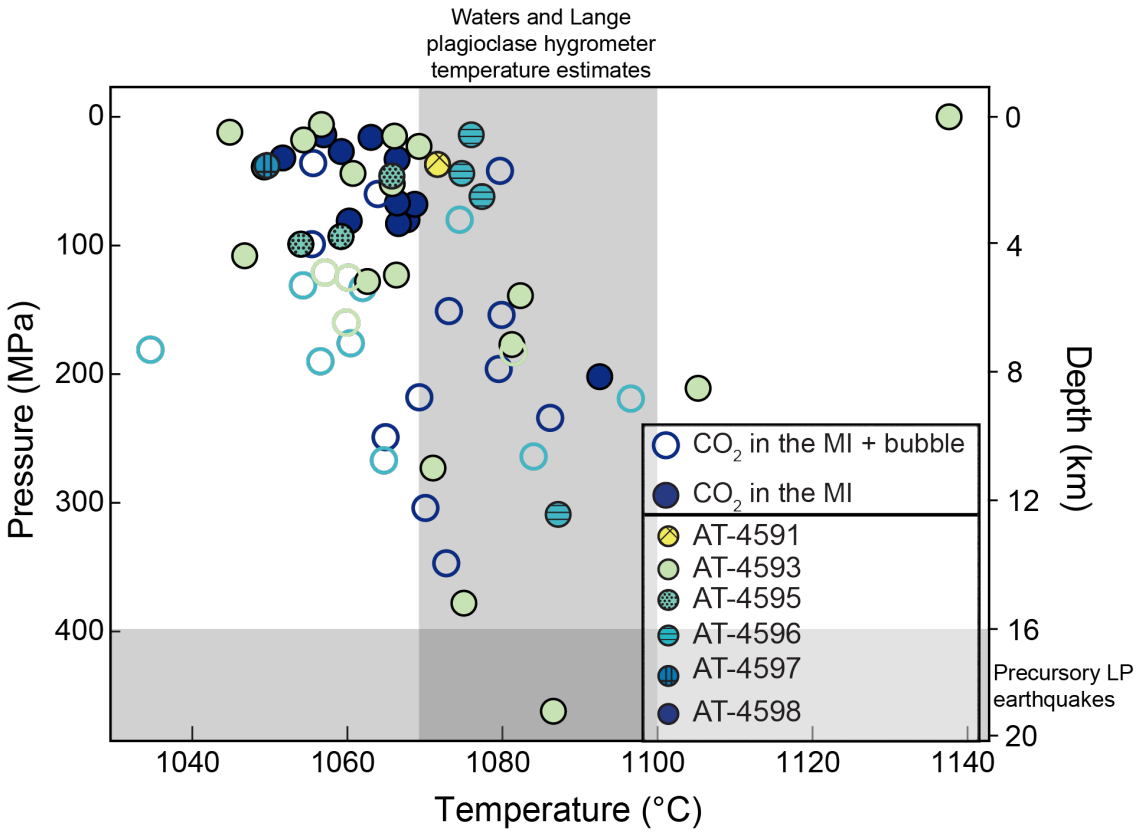

Figure 3.11. Storage conditions in P-T space.

Temperatures from Olivine-liquid thermometer (Putirka, 2008) and pressures from Vesical 2 (Weiser et al., 2022) using MagmaSat model (Gualda and Ghiorso, 2015).

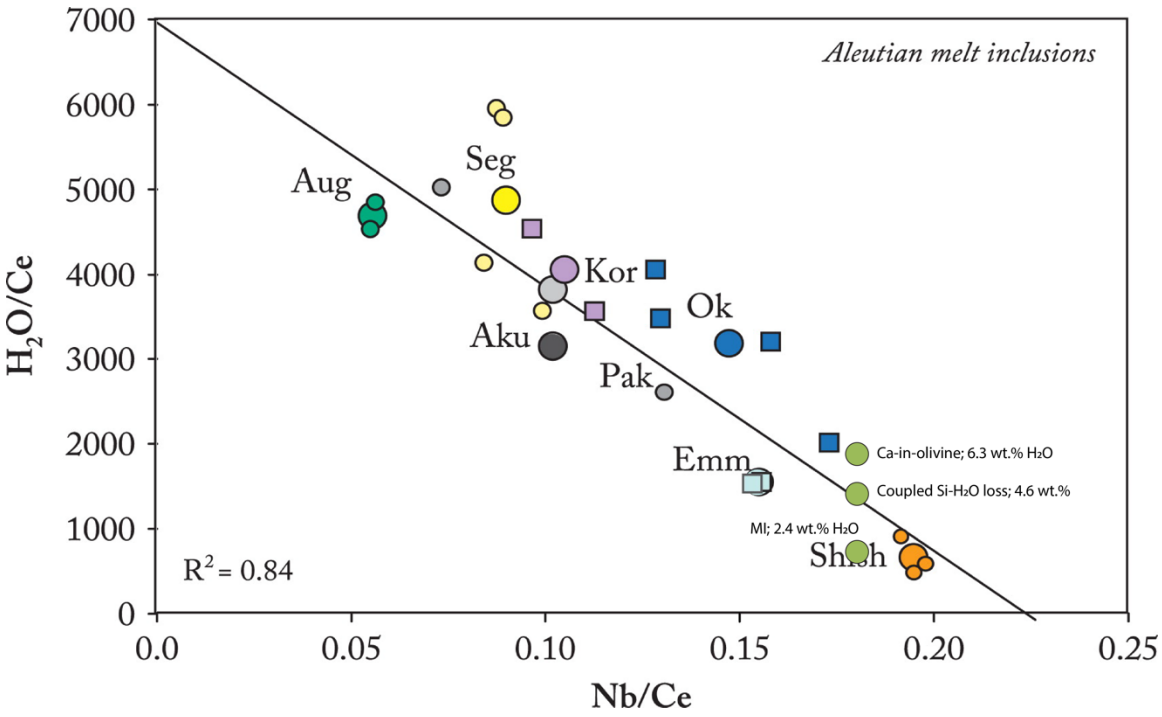

Figure 3.12. Relationship of H_2O/Ce vs Nb/Ce for melt inclusions at Mount Veniaminof.Modified from Plank et al. (2013) Green points represent different H_2O/Ce ratios for water contents calculated using MI H_2O concentrations, coupled Si-H_2O H_2O concentrations from Portnyagin et al. (2019), and H_2O concentrations from the Ca-in-olivine hygrometer from Gavrilenko et al. (2016). H_2O/Ce vs. Nb/Ce for other edifices along the Aleutian Arc are also listed.

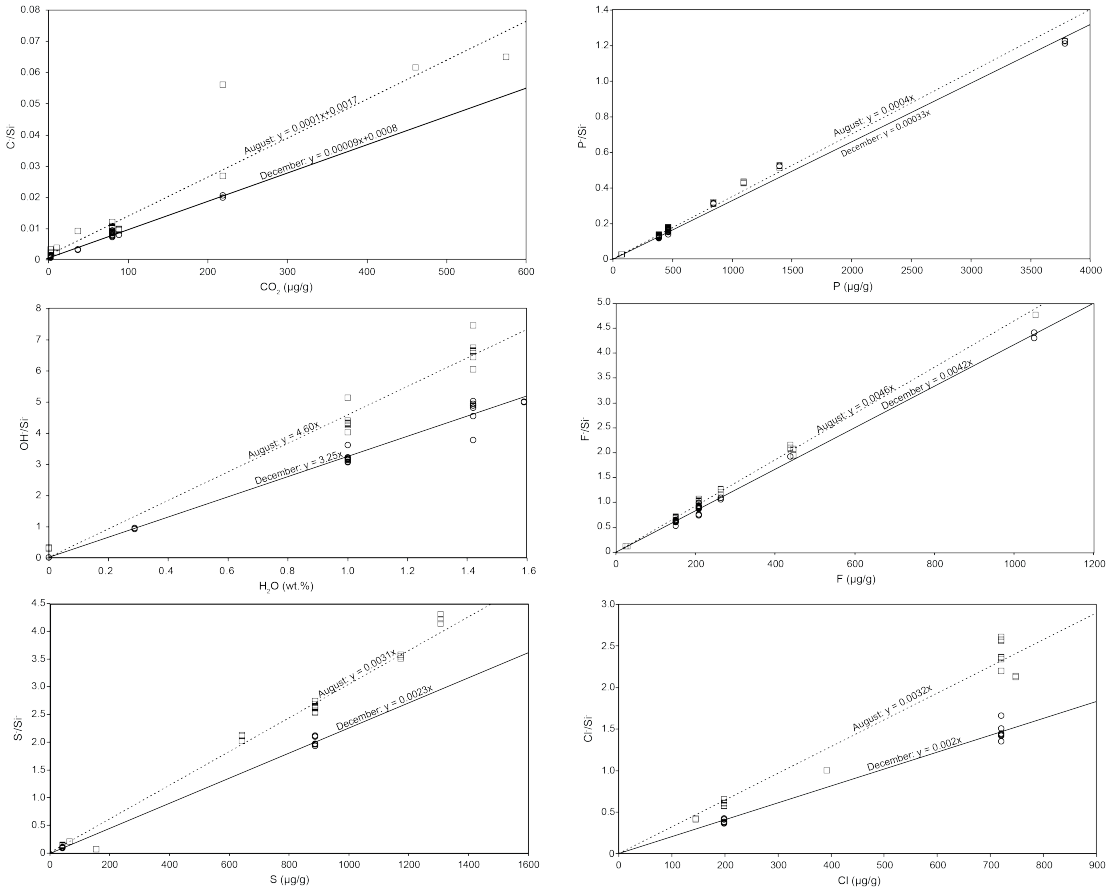

Figure 3S.1. SIMS calibration curves for both data acquisition dates.

Data collected in December are circles with a solid tread line. Data collected in August are squares with a dashed tread line.

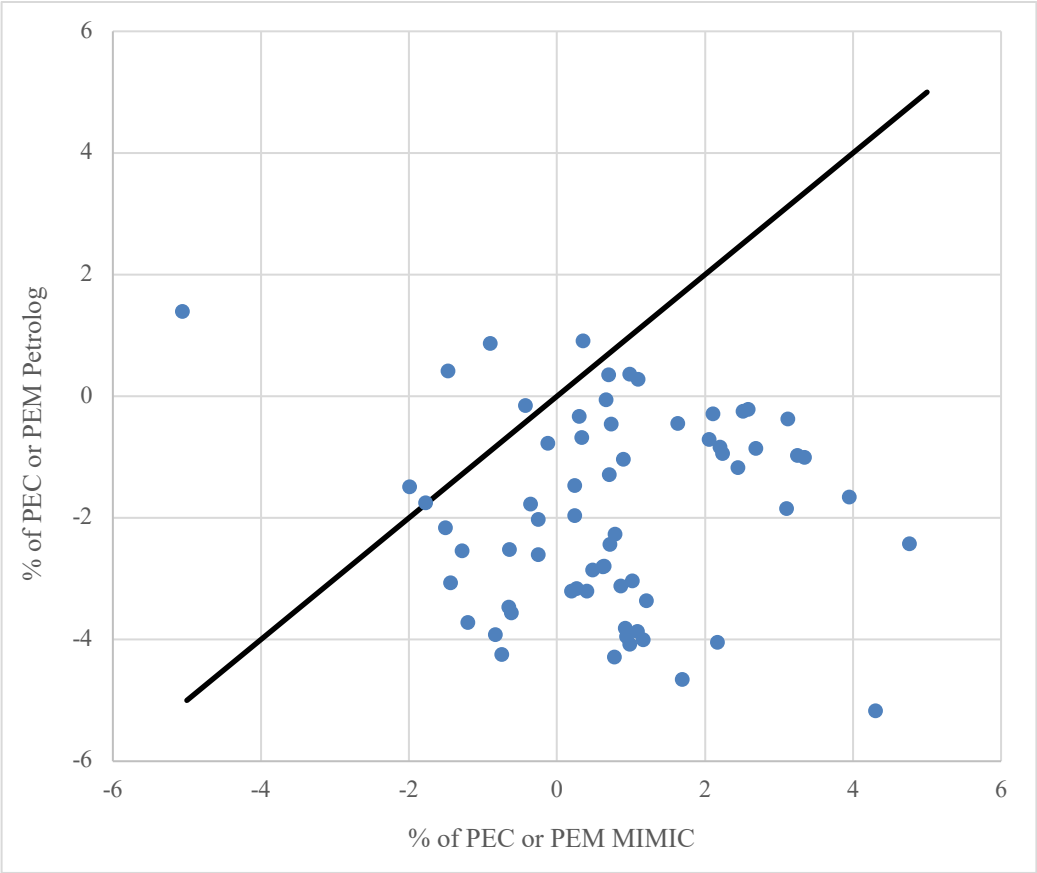

Figure 3S.2. Comparisons of the post-entrapment modification (PEM) models.

Comparisons of the post-entrapment modification (PEM) models with a 1:1 line. MIMIC models predict higher amounts of post entrapment crystallization than the Petrolog3.1 (Danyushevsky & Plechov, 2011) model. Differences in PEM could be due to different fO_2 models used in the calculation

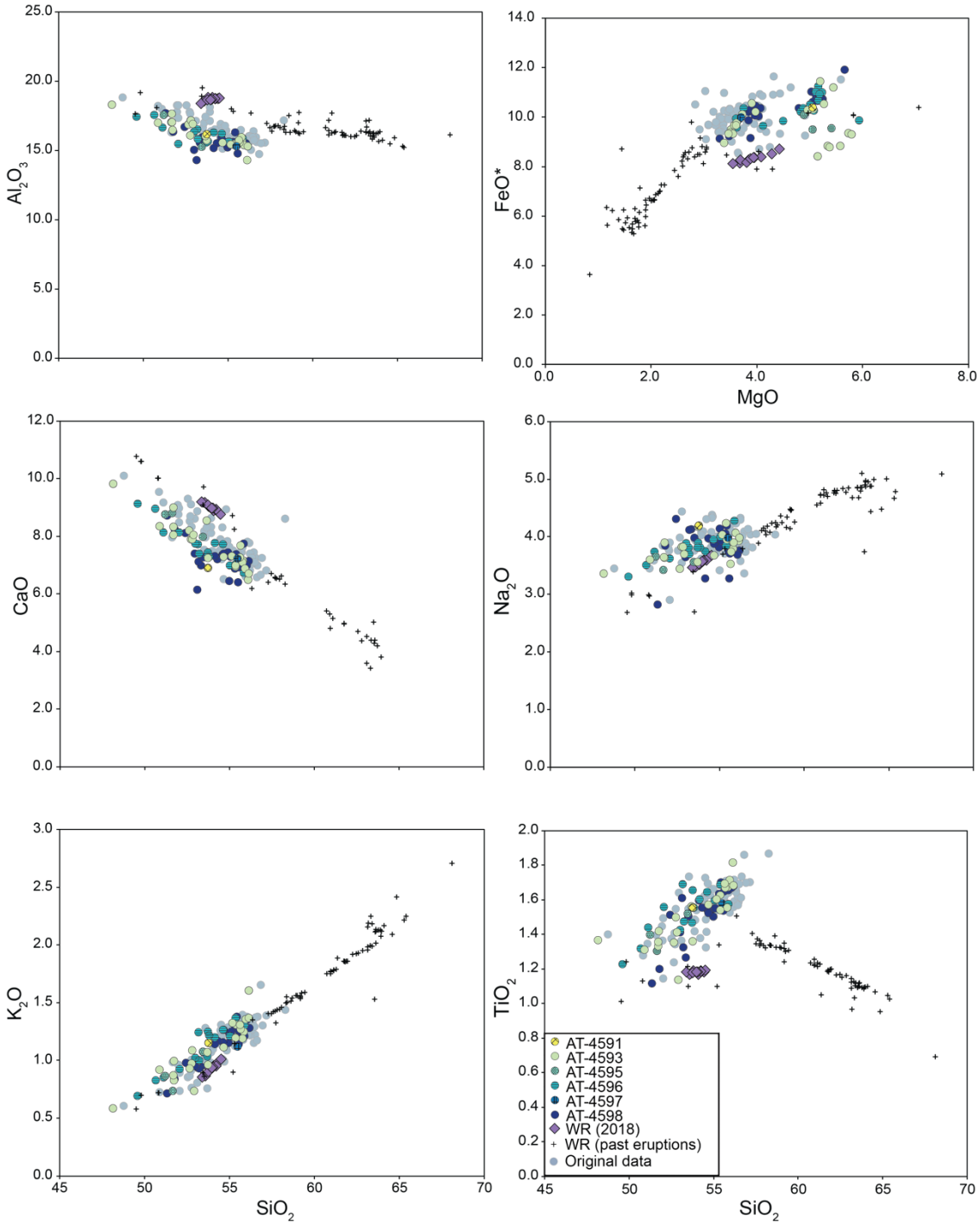

Figure 3S.3. Harker diagram for modified melt inclusion data (petrolog).

Original uncorrected data is presented as more transparent dots. Whole rock from the 2018 eruption is denoted as purple diamonds.

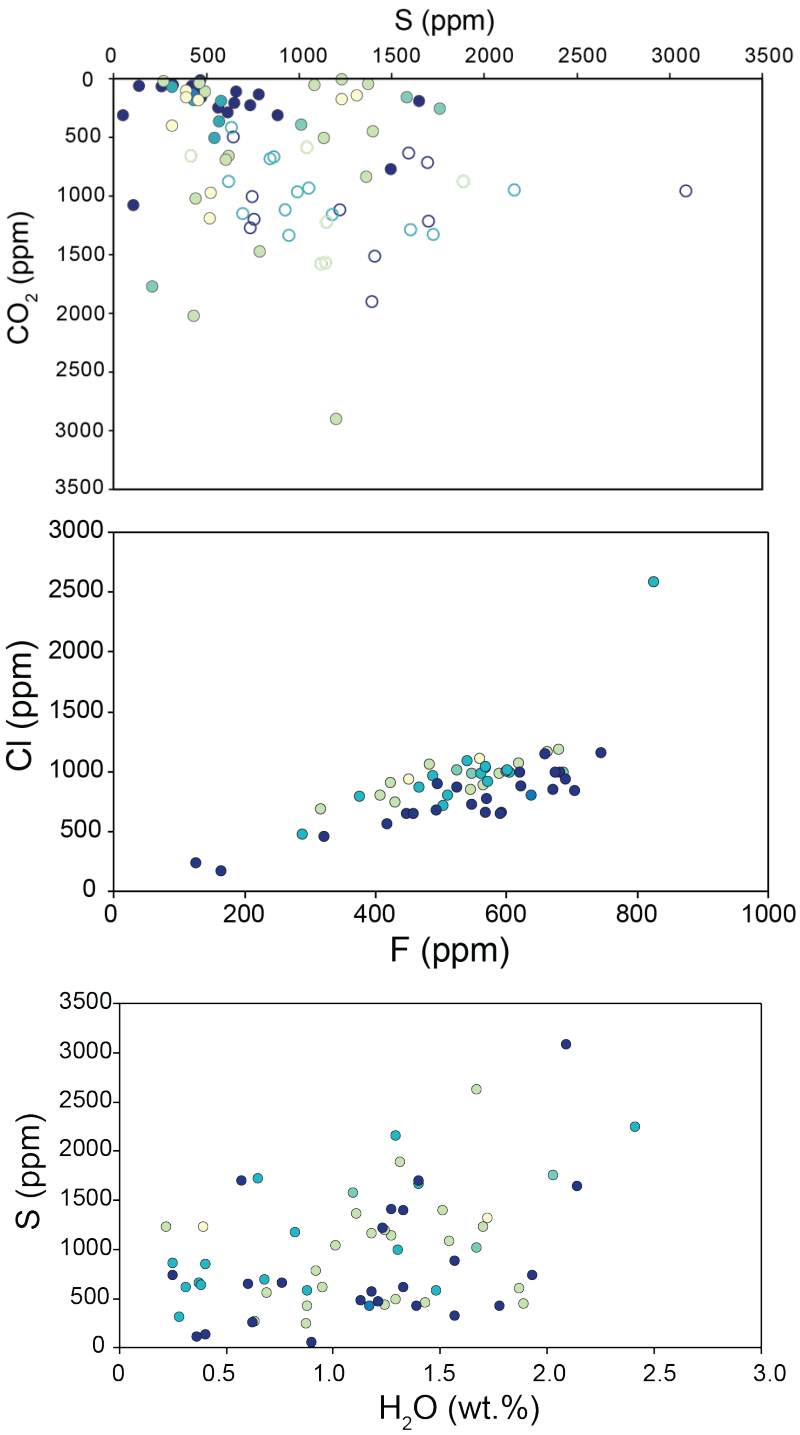

Figure 3S.4. Other volatile trends for MIs at Mount Veniaminof.

(a) S vs H2O, (b) CO_2 versus S, and (c) Cl versus F based on SIMS measurements of melt inclusions from mount Veniaminof.

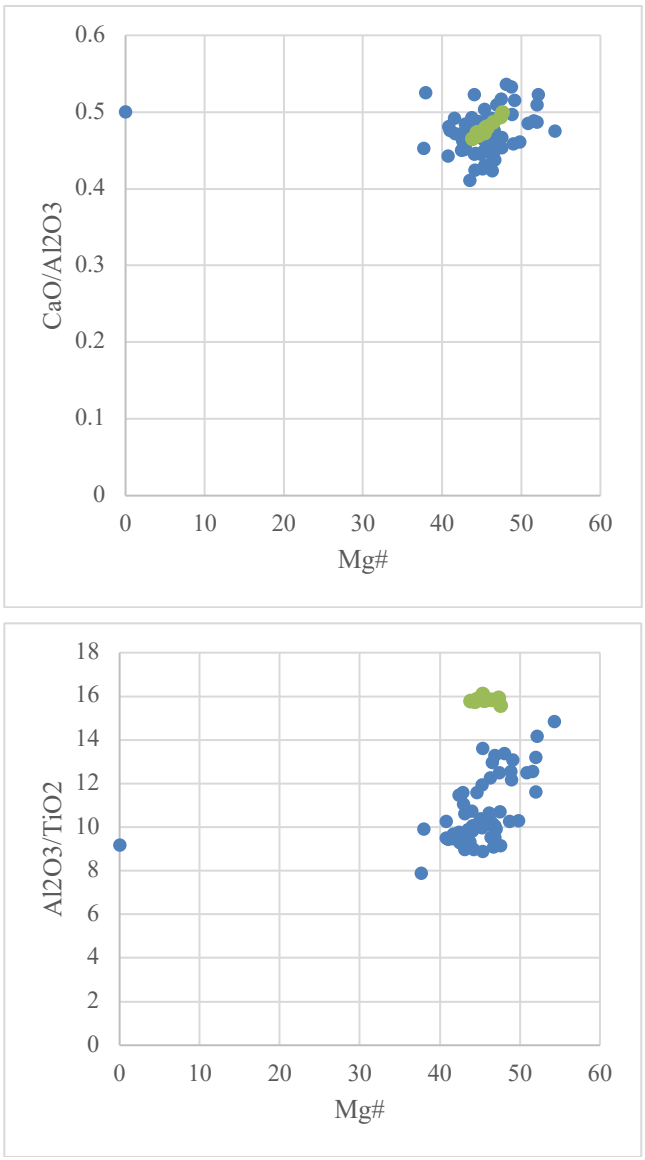

Figure 3S.5. Incompatible ratios for Portnyagin (2019) SiO2-H2O loss model (a) CaO/Al2O3 vs. Mg # and (b) Al2O3/TiO2 vs. Mg#. Green circles are whole rock data from the 2018 eruption at Mount Veniaminof from (Loewen et al., 2021) and blue circles are the data from melt inclusions at Mount Veniaminof.

Chapter 4. A critical missing connection to melt embayment ascent chronometry: Detailed 3D textural analysis of olivine growth and melt embayment formation

in prep to be submitted to JVGR

Huggins, E.G., Ruprecht, P. Loewen, M.

ABSTRACT

Decompression rates of magmas can significantly impact changes in eruption style and vigor. While there have been many petrological tools used to determine decompression rates, the measurement of volatile concentrations in melt embayments, pockets of melt within a crystal, is still considered one of the most effective methods. This is especially powerful when paired with magma storage conditions from external methods (i.e., melt inclusions). The application of melt embayments (ME) is a burgeoning field, but many past usages have been limited in the number of measured samples. Small (>10) sample sizes are partly due to complexities in host-mineral morphologies and melt embayment morphologies and the precision necessary in how samples have to be prepared. Here we present 25 three-dimensional (3D) volume models of melt embayments and host olivine grains from the 2018 eruption at Mount Veniaminof derived from micro x-ray computed tomography. We address different assumptions leveraged in the usage of melt embayment for ascent rate chronometry. These include complicated geometry of both the host mineral and melt embayment; hydrogen diffusion through the olivine; and bubble formation within the melt embayment. We find that melt embayments growing in crystal clusters may preserve a different decompression rate history than embayments in single crystal hosts. In highly necked embayments, diffusion through the host olivine grain is possible, leading to underestimates of ascent rates. We also find that bubbles that form within the embayments can possibly travel through the embayment channel

leading to inaccurate ascent rates. Accounting for these complications will lead to embayments that better approximate the natural phenomena.

1. Introduction

The rate of magma decompression controls the dynamics of volcanic eruptions through the degassing of volatiles, crystallization, nucleation, and fragmentation of magma (e.g., Rutherford, 2008). Recent research has highlighted the critical link between the explosivity of eruptions and ascent rate of magma (Barth et al., 2019), and its importance in understanding the effusive-explosive eruption transition (Cassidy et al., 2018). Thus, understanding ascent rates is paramount for human response during eruption. Over the last several decades, new petrological methods have been developed to determine ascent rates of magmas (i.e., Rutherford, 2008) that complement geophysical techniques (e.g., Scandone & Malone, 1985). Several mineral-based and texturally controlled geospeedometers have leveraged large changes in intensive parameters during ascent that impact the stability of mineral phases and that can control nucleation and growth of microlites and bubbles. These methods use textural analyses of microlites by comparing natural samples to decompression experiments (Castro & Dingwell, 2009; Couch, 2003; Martel & Schmidt, 2003); thermodynamic modeling and phase relationships (Huggins et al., 2021); the breakdown of reaction rims on amphiboles (Rutherford, 2008; Rutherford & Hill,

1993); analysis of microlite number density (Couch, 2003; Loewen et al., 2021; Szramek, 2016; Toramaru et al., 2008); and bubble number densities (Hajimirza et al., 2021; Shea, 2017; Toramaru, 2006). However, while these methods unambiguously are controlled by ascent and degassing, they are all influenced by other processes occurring in the magma conduit, such as shallow fragmentation (bubble number density), or are limited by kinetic timescales (i.e., rates of nucleation and crystal growth), and are better suited for applications with longer timescales (microlite number density, reaction rims).

Diffusion modeling of concentration gradients of pressure-sensitive elements (i.e., volatile elements) in melt embayments (also referred to as melt reentrants) has been used to determine the timescales of ascent and can potentially capture magma ascent timescales on the order of minutes (Liu et al., 2007; Lloyd et al., 2014). Melt embayments are open pockets of melt hosted within a crystal. The origin of melt embayments has been attributed to dissolution of the host mineral or through defects in crystal growth (Welsch et al., 2013). Unlike melt inclusions, which are fully enclosed by the host crystal, melt embayments remain connected to the carrier melt in which the host crystal is dispersed. This connection facilitates chemical exchange of the melt embayment with the surrounding melt (Liu et al., 2007). During ascent, volatile elements in the matrix melt respond to pressure-changes by exsolution once saturation for a particular volatile element has been reached. This sets up a compositional gradient between the melt embayment and the surrounding melt. The result is multi-element volatile

diffusion (H, C, S) from the interior of the embayment to the exterior melt (i.e.,Ferguson et al., 2016; Hosseini et al., 2023; Humphreys et al., 2008; Lloyd et al., 2014; Moussallam et al., 2019). The diffusion gradient is arrested when the melt quenches to glass during fragmentation and eruption at the vent. A timescale can be extracted by fitting a diffusion profile to measured compositional gradients. Melt embayments experience similar issues as the other tools for geospeedometry presented above; however, these embayments are directly tied to the elements most affected by decompression, such as volatile elements and species and their saturation state in the magma.

Embayment-based geospeedometry has been applied over a wide compositional range from felsic (Hosseini et al., 2023; Liu et al., 2007; Myers et al., 2019, 2021; Saalfeld et al., 2022) to intermediate and mafic magmas (Ferguson et al., 2016; Humphreys et al., 2008; Lloyd et al., 2014; Moussallam et al., 2019; Zuccarello et al., 2022) in both natural samples and experiments. In the more mafic applications, a correlation between decompression rate and eruption magnitude has been proposed (Moussallam et al., 2019). On the other hand, silicic samples do not show the same correlation, possibly due to delayed degassing (Mangan & Sisson, 2000) or the studies did not accounting for non-linear decompression rates (deGraffenried & Shea, 2021; Lloyd et al., 2014; Su & Huber, 2017).

Although the use of melt embayments to determine ascent rates is on the rise, past ascent rate studies have only utilized small (>10) sample sizes. This is

partly due to the complicated nature of the sample preparation (Ferguson et al., 2016; Lloyd et al., 2014) and assumptions applied during modeling (i.e., constant ascent rates, boundary conditions, 1D diffusion profiles; deGraffenried & Shea, 2021). Sample preparation for melt embayment analyses necessitates fastidious care to polish the extent of the melt embayment for a full diffusion profile (Lynn & Desmither, 2023), requiring ample documentation through imaging to determine the length scales necessary for diffusion modeling. Equally important is determining the crystallographic orientation of the grain owing to the anisotropic growth of olivine. This leads to anisotropic diffusion rates that vary over orders of magnitude along different axes (Barth & Plank, 2021; Shea et al., 2015). The grains must be properly oriented to expose the full extent of the embayment for analyses while ideally also exposing the most important two-dimensional (2D) slice of the host olivine (Lynn & Desmither, 2023) for diffusion chronometry. Crystals are three-dimensional objects, so reducing these objects to a 2D slice for analyses can potentially lead to inaccuracies and uncertainties in measurements (Lubbers et al., 2023; Lynn & Desmither, 2023; Mourey & Shea, 2019; Shea et al., 2015).

Ascent rates based on small sample sizes may not truly be representative for the eruption in question. It does not allow for an analysis of whether ascent rates are uniform and tightly constrained or whether large ranges in ascent rates are recorded in the embayment record. The latter may reflect variable ascent rates of different batches of magma. Moreover, smaller sample sizes make it difficult to

address the assumptions needed for diffusion modeling. Only by going after larger sample sizes with varying geometry can we explore whether there are biases by analyzing the simple geometry embayments.

After completion of the time-intensive and assiduous melt embayment preparation, analyses of volatile concentration gradients in embayments can provide first order information of magma ascent and degassing. Multiple different diffusion codes have been created, each with differences in boundary conditions. However, the large simplifications and restrictive assumptions to ease modeling and help data interpretation have limited the use of melt embayments. For example, a recent study has shown that for embayments with a pinched channel (herein referred to as necking), 1-D approximations lead to overestimations of ascent rates (deGraffenried & Shea, 2021). Thus, the next generation of embayment studies should take embayment geometry more directly into consideration. Large populations of mineral grains are necessary for understanding magmatic history from crystal-based studies (Ruprecht et al., 2023) that in the case of melt embayments potentially reveal a range of decompression rates for different populations.

To interpret ascent rates derived from natural melt embayments, it is imperative to reconcile volatile concentration gradients with information about the formation of melt embayments through thorough textural analyses of the host mineral and the embayment itself. There have been recent studies on textural analyses of bubbles in embayments (Cashman & Rust, 2016) and textures of

embayments in quartz grains (Ruefer et al., 2021), but there have not been any studies connecting the growth of the host mineral to melt embayment geometry. We present three-dimensional volumes of host olivine grains with melt embayments (n=25) derived from micro-computed X-ray tomography. They are a subset of an even larger sample set (n=102) that were documented in detail via microscopy and optical imagery.

2. Samples

Tephra samples were obtained from the 2018 eruption at Mount Veniaminof, where abundant embayments vary in complex geometry, serving as an important case study for testing assumptions leveraged in the diffusion-based modeling of melt embayments. Tephra samples from the 2018 eruption at Mount Veniaminof were collected by colleagues at the Alaska Volcano Observatory in the 2019 field season. Further details regarding sample collection are presented in Chapter 3.

3. Methods

7.13.1 Computed X-Ray Tomography

For each tephra sample from the 2018 eruption at Mount Veniaminof, olivine grains were manually sieved into different-sized fractions, focusing on the 200-

800 µm size fraction to account for potential volatile loss due to particle size (Lloyd et al., 2013). Olivine was then chemically separated using lithium heteropolytungstate heavy liquid (LST; density of 2.85 g/ml). From the heavy fraction, olivine grains were hand-picked from clinopyroxene grains and other subordinate heavy phases (e.g., oxides) using a stereo microscope. The separated olivine grains were then submerged in mineral oil to inspect each grain internally for possible melt embayments. Olivine grains with embayments were chosen for micro-x-ray computed tomography (micro-CT) from three tephra layers of the 2018 eruption: AT-4598, the first tephra fall of the eruption (n = 21); AT-4596, the middle section of the eruption (n = 22); and AT-4593, the late November explosive event (n = 18). Olivine grains were then set into a wide-mouth straw with layers of dental resin and 10-15 grains per olivine grain layer. However, we recommend for future work to use small-mouth straw and the separation of individual grain using low density materials like paper wipes.

Computed tomography scans were conducted by pink beam tomography (Rivers, 2016) using GeoSoilEnviroCARS (sector 13) split bending magnet beamline 13-BM-D synchrotron microtomography at the Advanced Photon Source of Argonne National Laboratory, Illinois. A cerium-doped lutetium aluminum garnet (Ce:LuAG) scintillator was used to convert the compositional contrast in the X-ray images to visible light (Yu et al., 2019), where the visible light images were focused into a 5x microscope objective and recorded by a charged coupled device (CCD) camera. The exposure time for each image was

0.08s and the image pixel size was 1.09 microns (1.09x1.09x1.09 voxels). A total of 1200 2D radiographic scans over 1920 × 1920 pixels were acquired over a step size of 0.05□over 3600 angles for a total rotation of 180□. To account for non-central grain placement to the axis of rotation, the axes of rotation were corrected for each grain in the layer and checked at a step size of 10□rotations to ensure that the grain remained in the field of view for each rotation.

The micro-CT data were initially processed using IDL Tomography (Rivers et al., 1999) for data reconstruction and visualization to reduce ring artifacts and anomalous pixels. Processed data files were reduced in size using the Fiji distribution of ImageJ visualization software (Schindelin et al., 2012) by cropping volumes and removing slices that did not have the target grain in view. The creation of 3D volumes and segmentation of grains were completed using 3D Slicer (**Figure 4.1;** Federov et al., 2012; http://www.slicer.org). How 3D slicer was used to segment the grain is described in supporting text 1.

7.23.2 Sample Preparation

After collecting the micro-CT scans, the layers of olivine grains in the dental resin mount were separated with a soldering iron, and olivine grains were released from each layer by dissolving the dental resin in acetone. Creating mounts for embayment analyses requires care as often the best plane for polishing the embayment is not the preferred resting position of the grain. Precise placement of embayments is especially important in necked olivine grains to

ensure the channel is completely exposed during polishing. Grain mounts were created from a 1-inch plastic ring mount and topped with parafilm, where we placed a droplet of high-viscosity glue gel on the parafilm surface (**Figure 4.2**). While the droplet of the gel is set, single grains are oriented under the microscope to align the preferred polishing plane with the desired exposure of the embayment. As the high-viscosity glue dries, the orientation of the grain is monitored under a stereo microscope and small adjustments are made if the grain is shifting (**Figure 4.2**). Once the gel and olivine grain are set, the crystal mounted in superglue is cast in dental resin to create a surface for easier minor manipulation of the mounts if required during polishing. Grain mounts are placed on top of the ring form to allow efficient polishing. The grains are initially exposed via 600–800 grit silica carbide paper and then finely polished with 1200 grit silica carbide paper and finished with 9 to 1 μm diamond paste. After polishing, the grains are removed from their individual mounts with a soldering iron, cleaned in acetone, and placed in an indium mount for subsequent analysis. Lynn et al. (2023) put forth a detailed roadmap for sample preparation of olivine grains for diffusion analyses to get the best orientation of the grain for microanalytical techniques. While this approach is particularly useful for orienting grains without inclusions, we find the technique outlined in this paper to be the most efficient for melt inclusions and embayments. In Lynn et al. (2023), the grain is oriented on a piece of masking tape with the side of the crystal of interest facing down. In the technique presented in this paper, the melt embayment is mounted facing up

(**Figure 4.2**) so fine adjustments can be made under a stereomicroscope to ensure the correct plane of the embayment will be exposed.

4. Results

In the next sections we present data related to the crystallographic axes of olivine grains. Videos of the created 3D volumes are located in the supplement. Between the accompanying figures and text there are differences in the type of indexing used to denote crystal faces based on longstanding crystallography nomenclature, defined by the types of brackets enclosing the form. Curly braces, what is dominantly used through the text, refer to a set of crystals faces related by symmetry. Round brackets, used in the figures, denote a specific plane. So, in essence, {101} refers to all {101} planes in the crystal, while the (101) refers to a specific plane in the crystal's coordinate system.

For consistency, we employ terminology defined in past papers. In the case of olivine, we separate populations of grains based on textures presented in Welsch et al. (2013). Here, we define basic texture terms that are used throughout this chapter. First, a single grain olivine refers to a single crystal (**Figure 4.3**). The grain may be euhedral (well defined crystal faces) or subhedral (less defined crystal faces). A group of crystals growing together are referred to as a cluster. In these clusters, grains are attached, overlap, and may be euhedral to subhedral. In both single grains and crystal clusters, grains may be full grains or fragments. All grains are surrounded by silicate melt. Parallel groups refer to grains that are

clustered in the same orientation (less than 3° misorientation; Welsch et al., 2013; Weiser et al., 2018).

7.34.1 Host Olivine Grains

All single crystal grains (n=17) have well-developed {110}, {010}, and {021} faces, where all crystal faces are well-developed in the euhedral grains and subhedral grains only express {021} and {010} faces, with rounded {110} (**Figure 4.4**). In grain fragments conchoidal fracture is visible. A small population of single grains exhibit relict skeletal crystal habits (Welsch et al., 2013) expressed by the presence of a depressed section on the {021} faces of the grains (**Figure 4.4b**).

The other population observed are crystal clusters (n=8, **Figure 4.3**). Many of these grains have crystals oriented in parallel groups (Figure 4a,d). Some parallel groups of crystals display hierarchical patterns of grain ordering, as described by Welsch et al. al (2013). The planes in which the grains are connected vary over this group, with half (4 of 8) of the population attached along the {021} plane of olivine grains with grains decreasing in size along the c-axis (**Figure 4.3a**, e.g., R1G3 in supplemental document 1). Some grains are attached along the {010} plane of the crystals, and another group is attached along the {110} plane of the crystal (e.g., R6G1, R2G1 in supplemental material 1).

There is variability in the amount of crystal intergrowth in the parallel units of the crystals. Some grains are only connected at a crystal face (**Figure 4.4d**)

while another set have large degrees of overlap, making determinations of the proper crystallographic faces difficult. In this latter group, the grains overlap completely without any channel of melt between each grain. However, there are grains with more distance between each crystal in the cluster, leading to melt pockets being trapped at each grain interface (**Figure 4.6ab**). While the majority of these grains are oriented in similar directions, misalignment between grains occurs in the subhedral clusters of crystals (e.g., R1G4 in supplemental document 1) or between two crystals on the {110} plane of the crystal (R7G8 in supplemental document 1).

There is only one instance of an olivine grain growing with a clinopyroxene grain observed in these samples (**Figure 4.4c**). This texture has been observed and noted in other studies at Mount Veniaminof (Bacon et al., 2007; Loewen et al., 2021). Both olivine and clinopyroxene grains have multiple inclusions and are both grain fragments. The crystal faces of olivine grains cannot be readily determined.

7.44.2 Inclusions

Melt inclusion chemistry, size, and texture are more thoroughly described in Chapter 3. Melt inclusions of varying sizes and oxide inclusions are prevalent throughout the host olivine grains. All analyzed grains had melt inclusions but the abundance varies greatly. In the whole grains, melt inclusions tend be present towards the center of the grain or close to the {110} faces of the crystal (**Figure**

4.3a and b, Supplemental document 1; **Table 4.1**). In **Table 4.1**, we present the distance of melt inclusions (>10 μm) from the a-axis for all grains where crystallographic axes could be determined, the length of the a-axis, and the distance to the a-axis normalized to the length of the a-axis to account for differences in grain sizes. Melt inclusions range from 1-52% of the length of the a-axis, indicating they are either close to the {110} faces or close to the center of the grain. Distances of melt inclusions in crystal clusters where there are large degrees of grain overlap were unable to be determined. Spherical melt inclusions imaged via micro-CT range from 5 to 55 μm in diameter, and other, more complex shapes are also frequent. This includes oblate, elongate (up to 90 μm in length), angular, or inclusions with negative crystal faceting. Multiple melt inclusions contain cubic oxides growing together. A majority of the melt inclusions include at least one singular shrinkage bubble, with a portion of inclusions including multiple shrinkage bubbles ranging from to 3-20 μm in diameter, depending on the size of the melt inclusion. Many of the inclusions have multiple discrete shrinkage bubbles (**Figure 4.4,7**).

Aside from the oxides associated with melt inclusions, isolated oxide inclusions are rare and only present in two grains. In one grain (R6G6, in supplemental document 1), the oxide is located near the rim of the grain by the {021} face of the crystal. In the other instance of oxide inclusions within a grain (R1G1), the oxides are closer to the cores of the host grain.

7.54.3 Melt Embayments

Melt embayments in host olivine grains are widely prevalent in analyzed grains in varying abundances. Multiple grains have two or more embayments present. Melt embayments in these samples show large variations in channel width. Some are highly necked (<10 μm in diameter), moderately necked (10–20 μm in diameter), and some have thick, cylindrical channels that are roughly uniform in diameter (>20 μm in diameter). The latter of the textures listed has been widely leveraged for diffusion chronometry to calculate decompression rates (i.e., deGraffenried & Shea, 2021; Hosseini et al., 2023; Lloyd et al., 2014, plus others).

These embayments also greatly vary in geometry. We recognize that the difference between each class is more gradational than discontinuous; however, there are clear features that we can use to simplify the results and discussion of these embayments. Each embayment in a grain is simplified into five classes (Figure 5), similar to morphology defined in Ruefer et al. (2021): i) simple 1-D channel (n=8), ii) hourglass (n=3), iii) bent (n=6), iv) highly necked/bulbus (n=8), v) complex (n=6). A simple 1-D channel does not have a bulb, and instead has a simple cylindrical channel. Hourglass embayments may have a bulb and experience some pinching in the middle of the channel, but the channel flares at the outlet. Bent embayments have a sharp bend of ~80-120□in the channel before the bulb (**Figure 4.6d**). In highly necked/bulbus embayments, the ratio of the diameter of the bulb to the diameter of the neck is greater than 20:1. Within

the necked embayments, there is a subclass of embayments with a sheet geometry (n=2). These embayments tend to be wide but have a constricted channel. We observe the most variability in geometry in complex melt embayments. To reduce the number of classifications, we refer to complex embayments as embayments with more than one outlet. The classification become more complicated as these embayments can have multiple bulbs and thin channels connecting the bulbs without an outlet, or these embayments can be as simple as a channel without a bulb traversing the host grain with an outlet on each side (R8G2, supplemental document 4.1).

Our classification differs from the Ruefer et al. (2021) classification to include what we define here as “highly necked” embayments from their “hourglass” embayments. We distinguish between these two types because we observe a clear difference between the shape of the channel at the outlet. We define the separation from hourglass to highly necked by the presence of a thin melt channel (less than 10 microns in width) that remains thin from the bulbus melt rich-portion to the mouth at the olivine-matrix melt interface. The word hourglass evokes a geometry that is constricted in the middle and flares at the base and bulb-channel interface. Necked melt channels (either straight or bent) terminate in a bulb that is either spherical, oblate, or angular.

The embayments with simple geometry often are shorter (30–70 μm in length) and a median channel diameter ~20 μm but up to 70 μm in diameter. There is one case of a grain with a longer channel (~170 μm in length) and a channel diameter of 27 μm. Length of this embayment is truncated by the

boundary of the grain fragment. Hourglass embayments are longer, with channels 70–100 μm in length.

Only 8 out of 31 melt embayments from Mount Veniaminof samples have simple 1-D channel geometries. These embayments are attached to the crystal on the {101}, {010}, {001} and the {021} faces (**Figure 6a,d**). In one rare case, two embayments have a wide embayment channel, but the height of the channel is thin, resulting in an embayment with sheet geometry attached on the {110} face of the crystal. Necked embayment channels have their outlet often at the {021} or the {110} face of the crystal. Other channels in melt embayments have varying degrees of tapering in the middle before it reaches a bulbous body, similar to the “hourglass” and “bulbous” embayment shapes described in the literature, such as in quartz embayments in Ruefer et al. (2021). In bent embayments, the kink bends the body of the embayment towards the {001} face of the grain. Bends are observed in embayments with variable degrees of necking (**Figure 4.6d**) and can be attached on the {110} face of the host crystal.

In singular host olivine grains, there is no correlation between melt embayment geometry and crystal habit. In both euhedral and subhedral full grains, all embayment morphologies are present. Embayments in crystal clusters also exhibit the full range of embayment textures; however, the cluster population of grains predominantly have more complex geometries.

Host olivine grains can also have multiple embayment outlets and termination points in the grain. These melt channels either span the extent of the

grain, have an outlet on the same crystal face or on adjoining crystal faces, or have more complex topologies (**Figure 4.6c**). In one case, the embayment has multiple bulbs connected by a thin bridge. Melt channels can have multiple branches that either connect to crystal faces or terminate in other sections of the grains. Melt channels also can have bends at obtuse angles or a bulb in the midst of the channel (**Figure 4.6d**). A number of these melt channels have varying degrees of vesiculation and microlite growth within the channel. Oxide growth within the channel is rare but is observed in one sample.

The majority of embayments do not have a bubble at the interface between the host crystal and the surrounding silicate melt. A majority of the highly necked embayments have discrete bubbles in the embayment bulb. In some cases, the body contains multiple discrete bubbles (<15 μm in diameter). In one highly necked embayment, the bulb's interior is devitrified and includes microlite and multiple cubic oxides (**Figure 4.7c**). Two necked embayments have bubbles intruding the interface between the melt channel and bulb. Bubbles in the interface are elongate, extended to ~20 μm in diameter. Moderately necked and 1-D embayments often do not have bubbles in the body of the inclusion. Intruding bubbles at the channel outlet are only observed in two samples, R6G1 (a sheet embayment) and R1G2 (bent embayment) (see supplementary document 1).

5. Discussion

While this dataset is small, the microtomography data of the olivine grains provides important context about olivine growth that is necessary to consider when calculating decompression rates from melt embayments. Because most of the grains are covered in matrix glass, many of the textures observed in the host olivine grain and the intricacies of the melt embayments would not have been observed without micro-CT analyses of the grains. These in-depth textural analyses clarify the growth histories of olivine growth and melt embayment formation that typically are missing from previous melt embayment papers.

7.6 5.1 Olivine Growth

The formation of melt embayments within the crystal is directly linked to the conditions of the host mineral growth; thus, broadly determining the timeline of melt embayment formation is critical to understand before making interpretations of melt embayments, especially those with complex geometries. The driving force for crystal growth is the degree of undercooling (ΔT), which is the difference between the liquidus temperature and the temperature of crystallization. Experiments of olivine growth have determined that the amount of undercooling in a system directly impacts the morphologies of crystals and can point to different processes affecting crystal growth. With smaller degrees of undercooling ($-\Delta T < 20°$), polyhedral crystals with well-defined faces will grow. At larger degrees of undercooling ($\Delta T > 20°$), growth of crystals becomes diffusion-limited, as the delivery and removal of elements is outpaced by cooling

timescales (Ruprecht and Welsch, 2023). We observe evidence for both euhedral olivine and evidence for relict skeletal olivine growth in the samples from Mount Veniaminof. While all grains from the 2018 eruption at Mount Veniaminof do not have hollow {021} faces, we observe these slightly depressed {021} faces in multiple olivine grains (**Figure 4.4b**) preserving that initial diffusion-limited growth of the crystals.

The emerging models of olivine growth documented by other textural studies is supported by zoning of incompatible elements in the olivine (i.e, Ni, P, Al, Cr; Ruprecht & Welsch, 2023; Salas et al., 2021; Shea et al., 2019; Welsch et al., 2014), where these incompatible elements form a boundary layer around the dendritic growing olivine (Welsch et al, 2013). The crystallization of oxides on melt inclusions can indicate tapping of these boundary layers of localized increases in concentration of incompatible elements at the interface of the dendritic olivine. Oxide formation can also aid in heterogeneous nucleation of bubbles (i.e., Shea, 2017). We observe oxide growth in melt inclusions from mount Veniaminof that appear cubic. Whether these oxides are Cr-rich spinels or other common oxides in olivine will only become clear with analyses of these grains. However, the presence of depressed {021} faces and the presence of the oxides points to an initial fast growth period of olivine grains at moderate undercoolings.

The initial period of fast olivine growth was then followed by a period of slow growth, where the polyhedral faces of the crystal formed (Faure & Schiano, 2005; Welsch et al., 2013; Ruprecht and Welsch 2023). It is in this period of near

equilibrium growth where the melt inclusions and embayments were trapped within the crystal. More physical evidence of this two-stage growth is presented by location of melt inclusions and embayments in the crystal. Skeletal growths of olivine have hollow {110}, {021}, and {001} faces. We observe melt inclusions (see **Table 4.1**) and embayments (**Figure 4.6**, supplemental document 1) around the fast-growing faces. In these zones, the olivine grains re-equilibrated with the surrounding melt, leading to olivine grains with little zoning of major elements (see Chapter 3). Element maps of incompatible elements could elucidate processes surrounding the growth of these crystals due to their slow diffusion rate.

Interpretations for the development of crystal clusters has been ascribed to variable processes, from mobile processes, such as the synneusis of individual crystals (Schwindinger & Anderson, 1989; Wieser et al., 2019) or from growth processes, such as earlier dendritic growth followed by slow ripening (Welsch et al., 2013). In the case of synneusis, grains are free-floating through convective processes and grains attach and orient themselves due to hydrodynamic forces (Holness et al., 2017; McIntire et al., 2019). Arguments against synneusis point to probability arguments against the attachment of the same crystal faces and minimization of interfacial energy for crystal attachment (Dowty, 1980; Welsch et al., 2013). The simple olivine aggregates from Mount Veniaminof (2–3 attached grains, no complex embayments) have clear faces with preferred orientation of growth, or smaller crystals attached on similar crystal faces pointing towards dendritic growth of these host olivine grains. In the

population of more complex olivine clusters, large pockets of melt (type v, see above) are present within the crystal, in favor of arguments of synneusis for the formation of these textures. Even in these aggregates, however, olivine grains overlap and display hierarchical ordering between the crystals. These grains have undergone multiple periods of growth, with crystal clusters formed in an earlier period, with multiple timings of fast and slow growth.

Past instances of preserved dendritic olivine described in arc settings are rare (Salas et al., 2021), largely due to the large degrees of undercooling necessary to form and sustain this texture (Mourey & Shea, 2019; Welsch et al., 2014). Artifacts of these textures can still be preserved in crystals. In dendritic growth of olivine, olivine will preferentially grow along the a-axis leading to crystals with elongated a-axes (Welsch et al., 2013). These textures are not observed in the samples from the 2018 eruption at Mount Veniaminof. We argue, however, that the crystal clusters with hierarchical growth represent an initial period of large degrees of undercooling that were followed by a period of slower cooling, as observed with the single crystals, where initial temperature gradients are produced by magma mixing. The complex melt embayments that form within these grains represent silicate melt that were trapped between crystals during the slow cooling, polyhedral growth. In these embayments, we observe microlite growth and vesiculation.

To form these textures, however, large temperature gradients are necessary. In Salas et al. (2021), the preservation of these textures is ascribed to continual degassing of CO_2 in a high CO_2/H_2O magma driving ascent from the

deep crust to surface during an eruption. Another explanation for the formation of these crystals has been attributed to magma mixing (Mourey & Shea, 2019). Melt inclusions from Mount Veniaminof (Chapter 3) are representative of magmas that have been captured at multiple crustal levels (~15 km and ~4 km), pointing towards the mixing of magma prior to eruption. Incompatible trace element ratios of whole rock analyses for the 2018 eruption at Mount Veniaminof suggest minor magma mixing between distinct magma compositions are the cause of compositional variation (Loewen et al., 2021).

Based on this textural analysis, we discern that the crystals in this study have experienced at least two periods of growth, one period of fast crystallization of olivine followed by slower cooling, where olivine grew euhedral faces. However, the more complex clusters of crystals could have formed at an earlier period, where matrix glass was trapped between the crystals. Embayments from these crystals would not be well suited for melt embayment geospeedometry, but further chemical analyses, through maps of incompatible elements, can elucidate processes occurring in the magma system at depth prior to eruption.

7.7 5.2 Melt Embayments

To understand the complex history preserved in these crystals, textural analyses of the host-crystals and melt embayments needs to be supported by in-depth chemical analyses. Firstly, melt embayment analyses have predominantly utilized simple, 1-D channel geometry embayments for the ease of modeling. Recent literature has shown that the simplification of a one-dimensional

approach for embayments with increases in pinching off of the melt embayment channel lead to over-estimations of the H_2O gradient (deGraffenried & Shea, 2021). This phenomena has been observed in H_2O gradients in embayments in natural olivine hosts at Mount Etna (Zuccarello et al., 2022). The complexity of embayments in host olivine grains from the 2018 eruption at Mount Veniaminof lends itself as a prime target to understand decompression rates preserved in non-ideal embayments, while comparing them to embayments with a simple 1D geometry (type i, see above). The range of melt embayments at Veniaminof also allow for a detailed investigation of the decompression rates from embayments with a systematic varying degree of necking (**Figure 4.3**).

Testing more complex embayment geometry will examine fundamental assumptions made in these diffusion-based ascent rates. Diffusion modeling limits diffusive flux of volatile elements to the melt embayment channel with no flux of volatile species occurring through the host mineral. Recent literature, however, has elucidated the anisotropic nature of H^+ diffusion through the host olivine grains (Barth et al., 2019; Barth & Plank, 2021; Jollands et al., 2022), with H^+ diffusion coefficients up to two orders of magnitude greater along the a-axis {100} of olivine compared to the b- {010} and c-axis {001} and can be in the same order of magnitude of diffusion through a basaltic melt. While an embayment may provide a pathway for the flux of H^+, H^+ could take advantage of diffusion through the crystal leading to decoupled H^+ decompression rates compared to other volatile species, such as S and CO_2. This would result in an inaccurate

decompression rate. This effect may be more apparent in highly necked embayments, where flux through the embayment channel is already limited.

Using Fick's first law, we recognize that the total flux of H^+ is the combination of the flux though the embayment and flux through the host olivine.

$$J_{Total} = J_{embay} + J_{olv} \quad (1)$$

$$J_{em} = \frac{-D_m^H \frac{\partial C}{\partial x}}{\frac{Area_{embay}}{Area_{total}}} \qquad J_{ol} = \frac{-D_{ol}^H (k_D) \frac{\partial C}{\partial x}}{\frac{Area_{ol}}{Area_{total}}} \quad (2)$$

Where the flux through the embayment is related to -D, the diffusion coefficient for H^+ in a silicate melt, $\frac{\partial C}{\partial x}$ is the change in concentration with respect to x, $\partial y \partial z$ (A) is the area of the melt embayment. The equation for flux through the olivine grain is similar except it accounts for the partitioning of H^+ between the melt and olivine (K_d). We create a non-dimensional value to understand the interplay of the three major parameters:

$$\frac{J_{em}}{J_{ol}} = \frac{1}{k_D} \frac{-D_m}{-D_o} \frac{A_{melt}}{A_{ol}} \quad (3)$$

We test out a range of diffusivity coefficients from a slow diffusivity coefficient (i.e., diffusion along the b- or c-axis; -10^{-15} to -10^{-13}) to fast diffusivity coefficients

(i.e. diffusion along the a-axis (-10^{-10} to 10^{-8}), a range of partition coefficients (K_d) of H^+ between the melt and olivine, and different areas of a necked embayment (from highly necked at 1–5 μm opening) to a simple 1-D channel (10–15 μm). We find that there is a small range for highly necked embayments and fast diffusion rates where diffusion through the olivine needs to be considered (**Figure 4.8**). By increasing the partition coefficient, the window where diffusion through the olivine needs to be considered. Different properties affect the diffusivity of H+ through the olivine, such as temperature (Barth et al., 2019; Newcombe et al., 2020). Increasing the temperature would lead to a larger region where olivine needs to be considered. While this model is simplified, it shows that there could be significant loss of H+ from the embayment, decoupling the H diffusion gradients from the CO_2 and S gradients.

7.85.3 Bubbles and Vesicles

Another requisite for diffusion modeling is that the melt embayment is pristine glass; however, the formation of bubbles or presence of vesicles points to a multiphase nature of embayments. Melt embayments from the 2018 eruption at Mount Veniaminof display either bubble formation or vesiculation in both the body and the channel of embayments, typically in complex melt embayments. In past embayment analyses, bubbles at the outlet of the embayment channel have been necessary to constrain boundary conditions (deGraffenried & Shea, 2021; Hosseini et al., 2023; Lloyd et al., 2014; Saalfeld et al., 2022). In the samples from Mount Veniaminof, the presence of a bubble or vesicles near the outlet are

rare. However, there are vesicles preserved in the external melt near the outlet of the embayment. By observing concave nature of the glass around the melt embayment outlet in 3D-volume data, we can overcome the lack of bubble issue. Intruding bubbles at the melt embayment outlet and vesicles were limited to highly necked embayments and not observed in simple, cylindrical melt embayments. In necked and complex embayments, the amount of vesiculation or bubble formation and the location of bubbles greatly varies. The most common case are free floating bubbles within the body of the embayment. Like in melt inclusions, the formation of intruding bubbles in the body of the embayment can lead to underestimation of the flux of volatile species, due to the loss of CO_2 to the shrinkage bubble. Previous studies have linked free floating bubble formation in crystal hosted embayments to size of the embayment channel (Cashman & Rust, 2016; Hosseini et al., 2023). Bubbles occur in embayments with channels >200 μm, and glassy embayments occur at a characteristic length scale of 100–200 μm. This is inconsistent with melt embayments with intruding bubbles from Mount Veniaminof, as bubbles are mostly observed in embayments with channels >100 μm in diameter, except for one embayment.

In at least two samples, bubbles were situated at the interface between the melt embayment bulb and channel. And, in the case of R4G3, the bubble intrudes ~5 μm into the channel. If the bubble nucleated elsewhere within the embayment and moved to the bulb-channel interface, are melt embayments preserving accurate CO_2 fluxes in the embayment? It also calls into question what the vapor bubble at the interface truly represents. For a bubble with a

density of 300 kg/m^3 (Steinberg & Babenko, 1978), a melt density of 2685 kg/m^3 (calculated using DensityX, Iacovino & Till, 2019), a magma viscosity of 100 Pa s (Giordano et al., 2008), and a bubble radius of 5 μm, the Stokes settling velocity for the bubble is 111 μm /day. With larger bubble radii, the time needed for bubble migration across the melt embayment channel decreases. Depending on the timing of formation of the melt embayment, bubble, and timescales of ascent, the budget of CO_2 within an embayment can be altered on timescales of ascent leading to decoupling of the CO_2 gradient with other volatile species, and, thus, inaccurate ascent rates. Moreover, depending on the length of the embayment channel, the outlet bubble could have been a bubble that had formed within the bulb and migrated during ascent.

6. Finding the missing link

The usage of volatile concentration gradients preserved in open pockets of melt in a host crystal is a novel technique for determining decompression rates of magma. The development of the melt embayment geospeedometer has shed light on the importance of magma decompression rates on controlling eruption dynamics. However, the simplifications used within these studies can lead to inaccurate ascent timescales and the small sample sizes used in melt embayment methodology makes it difficult to test assumptions to determine what this methodology is truly recording. Here, we consider three different assumptions that impact decompression rates from melt embayments:

1. **Flux of H^+ through the host olivine**: While recent models have started to include more complex geometries (deGraffenried & Shea, 2021), these models do not account for the possibility of H^+ flux through the olivine grain. When the melt embayment channel is sufficiently small and if the diffusion coefficient for H^+ through the olivine is on the same order of magnitude as the diffusion coefficient of H^+ through the silicate melt, the flux of volatiles could take advantage of other pathways through the host crystal.
2. **Outlet bubble:** Typical assumptions in melt embayment methodology use a bubble at the outlet as a boundary condition, driving the diffusion of volatiles through the channel. We have observed bubbles growing at the interface of the bulb and channel of two embayments. Calculations of the Stokes settling velocity show that, depending on the timescales of ascent and the length of the melt embayment channel, not only could lead to a decoupling of CO_2 from other volatile species gradients, but also questions what outlet bubbles truly represent.
3. **When are embayments formed:** Through an in-depth textural analysis we have revealed multiple populations of melt embayments and host olivine crystals leading to embayments with different thermal histories that could record different decompression rates. More complex geometries could possibly be utilized in melt embayment studies, but to do so, careful documentation of the host grain and embayment is necessary.

Along with ascertaining decompression rates from melt embayments, this textural study is best followed by using chemical models to understand the growth and preservation of both the complex embayment and host crystal geometry. Incompatible element maps for olivine (P, Al) can further reveal complex histories of the crystals leading to the formation of complicated melt embayment textures (**Figure 4.3c**). While these melt embayments may not be suited for determining decompressions rate, they still preserve vital information about the magmatic system prior to eruption that would otherwise be overlooked.

7. Future work

In the near future, 30 melt embayments from AT-4593, AT-4596, and AT4598 that were analyzed via micro-CT will be analyzed via nanoSIMS at the Caltech Microanalysis Center. Diffusion modeling will then be completed to calculate decompression rates for the 2018 eruption at Mount Veniaminof. These decompression rates will be compared texturally derived decompression rates from Loewen et al. (2021).

Acknowledgements

This work was performed at GeoSoilEnviroCARS (The University of Chicago, Sector 13), Advanced Photon Source (APS), Argonne National Laboratory. GeoSoilEnviroCARS was supported by the National Science Foundation – Earth Sciences (EAR – 1634415). Tomography capability developments were supported by DOE BES Geosciences (DE-SC0020112). This research used resources of the

Advanced Photon Source, a U.S. Department of Energy (DOE) Office of Science User Facility operated for the DOE Office of Science by Argonne National Laboratory under Contract No. DE-AC02-06CH11357.

TABLES

Table 4.1: Distribution of melt inclusions (>10 μm) in olivine grains normalized to the length of the a-axis

	Length of the a-axis (a – a')		*MI diameter*	*distance to 'a'*	$\frac{\text{distance to } 'a'}{a - a'}$
R1G1	434	MI1		88	0.20
		MI2	35	98	0.23
		MI3	21	105	0.24
		MI4	41	102	0.24
		MI5	26	51	0.12
		MI6	34	76	0.18
		MI7	25	100	0.23
R1G2	211	MI1	27	29	0.14
		MI2	28	93	0.44
R1G3	275	MI1	16.8	58	0.21
		MI2	22	45	0.16
R165	284	MI1	17	49	0.17
R2G1	316	MI1	27	45	0.14
		MI2	17	76	0.24
R2 G10	280	MI1	35	60	0.21
		MI2	15.6	65	0.23
		MI3	18	95	0.34
		MI4	18	83	0.30
		MI5	27	5	0.02
		MI6	42	85	0.30
R3G3	180	MI1	32	37	0.21
		MI2	41	56	0.31
		MI3	27	47	0.26
R4G3	228	MI1	15	21	0.09
R5G3	160	MI1	11	74	0.46
		MI2	10.3	58	0.36
R6G1	241	MI1	24	125	0.52
R6G2	200	MI1	30	38	0.19
		MI2	27	52	0.26
R6G12	200	MI1	19	53	0.27

R7G8	230	MI1	38	56	0.24
	230	MI2	24	39.2	0.17
	230	MI3	18	77	0.33
	230	MI4	21	57	0.25
	230	MI5	16	39	0.17
	230	MI6	30	48	0.21
	230	MI7	18	85	0.37

FIGURES

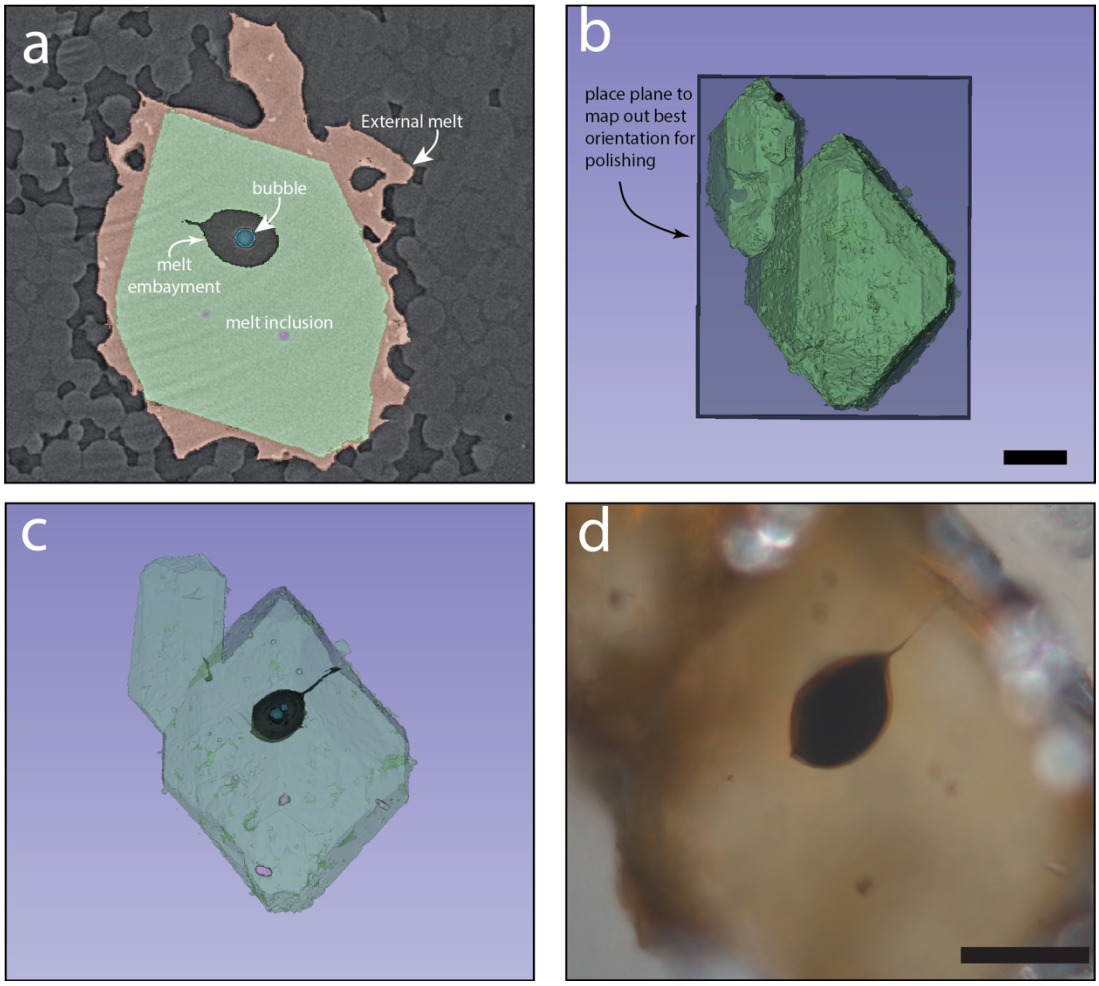

Figure 4.1. Example of segmentation slice of a grain.(A) Example of segmentation slice of a grain (R1G3) using 3D Slicer (Federov, A. et al., 2012; http://www.slicer.org. Segmentation of the grain shows the external silicate melt (brown), host olivine grain (green), melt embayment (Black), vapor bubble (blue), and melt inclusions (purple). In the background is the dental resin mount. Polishing set up for melt embayment analyses. On these ring mounts, a droplet of high viscosity super glue is places so grains can be carefully oriented to polish into the embayment; (B) Once segmentation is complete, users can map out a plane to polish the crystal to get the maximum extent of the melt embayment (C) After mapping out the proper plane for polishing, the user can remove everything above the plane to create a guide whilst polishing (D) Example polished surface of an olivine grain using the methodology presented in this paper

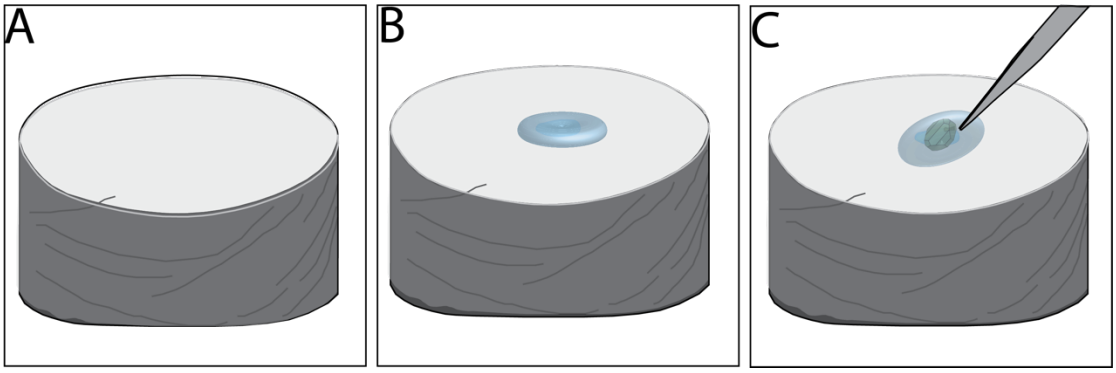

Figure 4.2. Set-up of mounting process for efficient polishing.

In (A), ParaFilm is placed over the 1-inch ring mount to create a surface for mounting. (B) a high viscosity adhesive/gel is placed on the ParaFilm surface. (C) The grain is placed into the adhesive and oriented with tweezers to expose the total extent of the melt embayment in the host mineral.

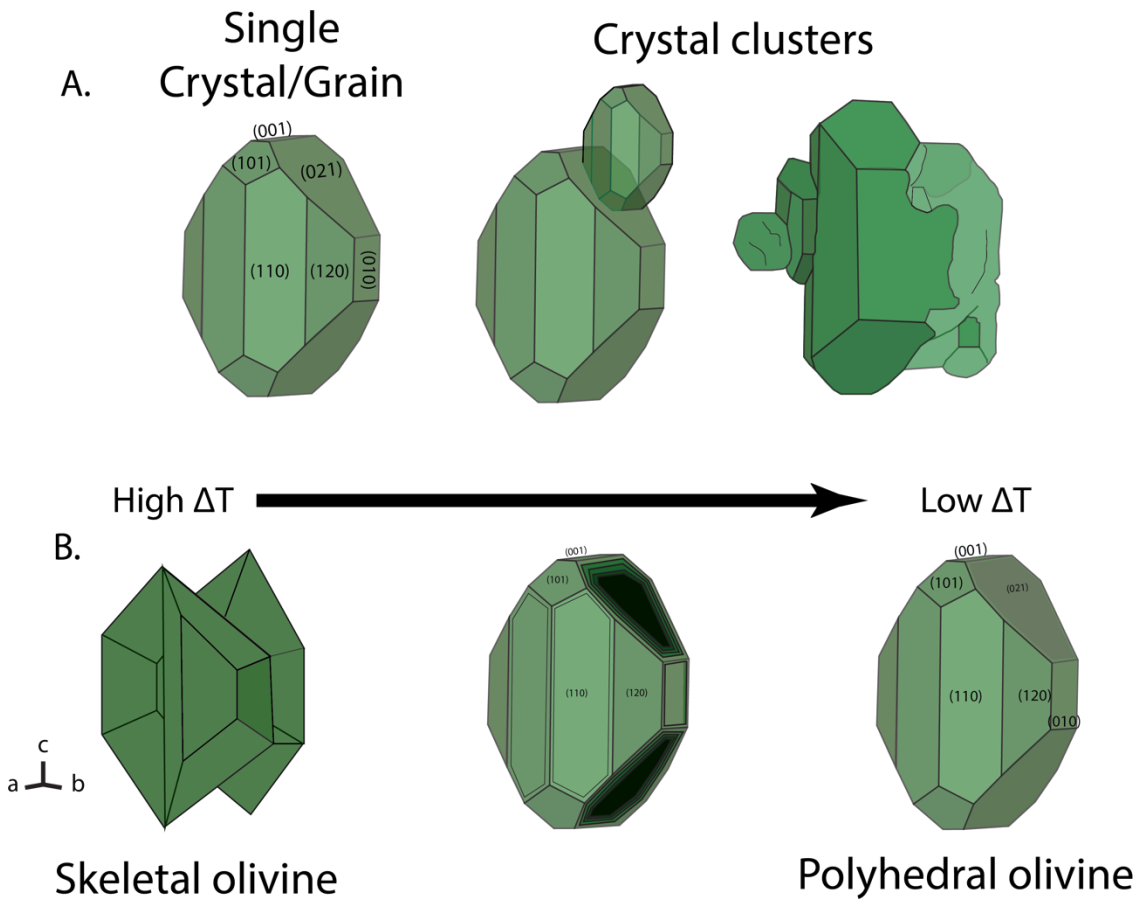

Figure 4.3. Example of different crystal forms of olivine, inspired by Welsch et al. (2013).On the top (A): example of the textures referred to in this chapter. (B) On the bottom from left to right, skeletal crystal habit formed in moderate undercooling. With changing of growth rate, olivine crystals start infilling the {110}, {021), and {010)} face of the crystal to form polyhedral olivine crystals. It is in these formerly hollow faces of the olivine where melt inclusions and melt embayments can be trapped. Crystals were made using Smorf crystal drawing, by Mark Holtkamp. Parameters used to make the crystal are “a:” 4.756, “b” 10.207, and “c” 5.98 and distances {010} = 0.5; {001} = 1.2, {021}= 1.3, {110} = 1.05, {101} = 1.85, and {120} = 1.35.

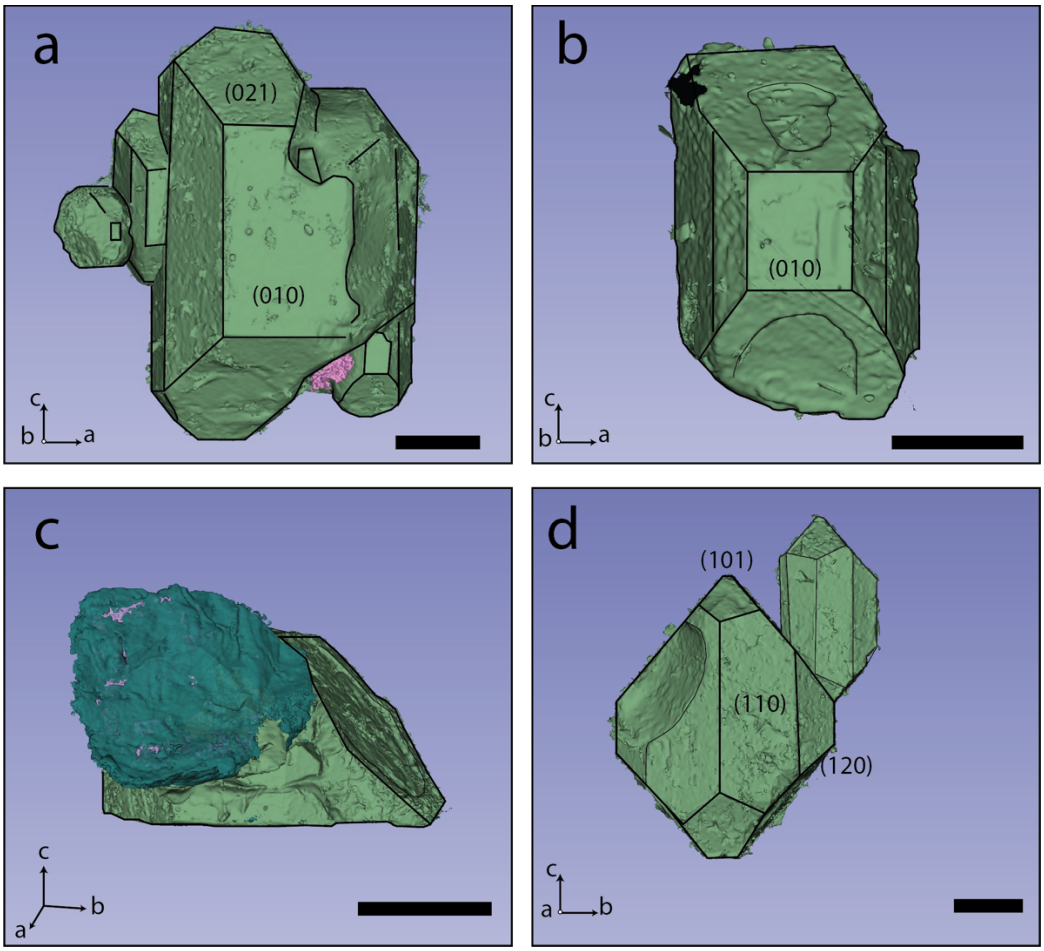

Figure 4.4. . Example 3D tomography data of host olivine grains from the 2018 eruption at mount VeniaminofExample 3D tomography data of host olivine grains from the 2018 eruption at mount Veniaminof with clear crystal faces defined. Tomographic data was performed at the GeoSoilEnviroCARS (The University of Chicago, Sector 13, Advanced Photon Source, Argonne National Laboratory and segmented using 3D Slicer. (A) Grain R6G5: Parallel organization with hierarchical growth. Crystals are attached on the (110) faces of the host olivine grain; (B) Grain R6G3: Single grain with evidence for skeletal growth that has filled in (C) Grain R2G2: fragment of the top of an olivine crystal showing the (021) face of the crystal. A clinopyroxene grain is attached around possible {110} faces of the crystal. (D) R1G1: Two crystals, hierarchical growth. Both crystals have clear crystal faces and are attached on the {021} face of the crystal. Videos of all grains are located in the supplement.

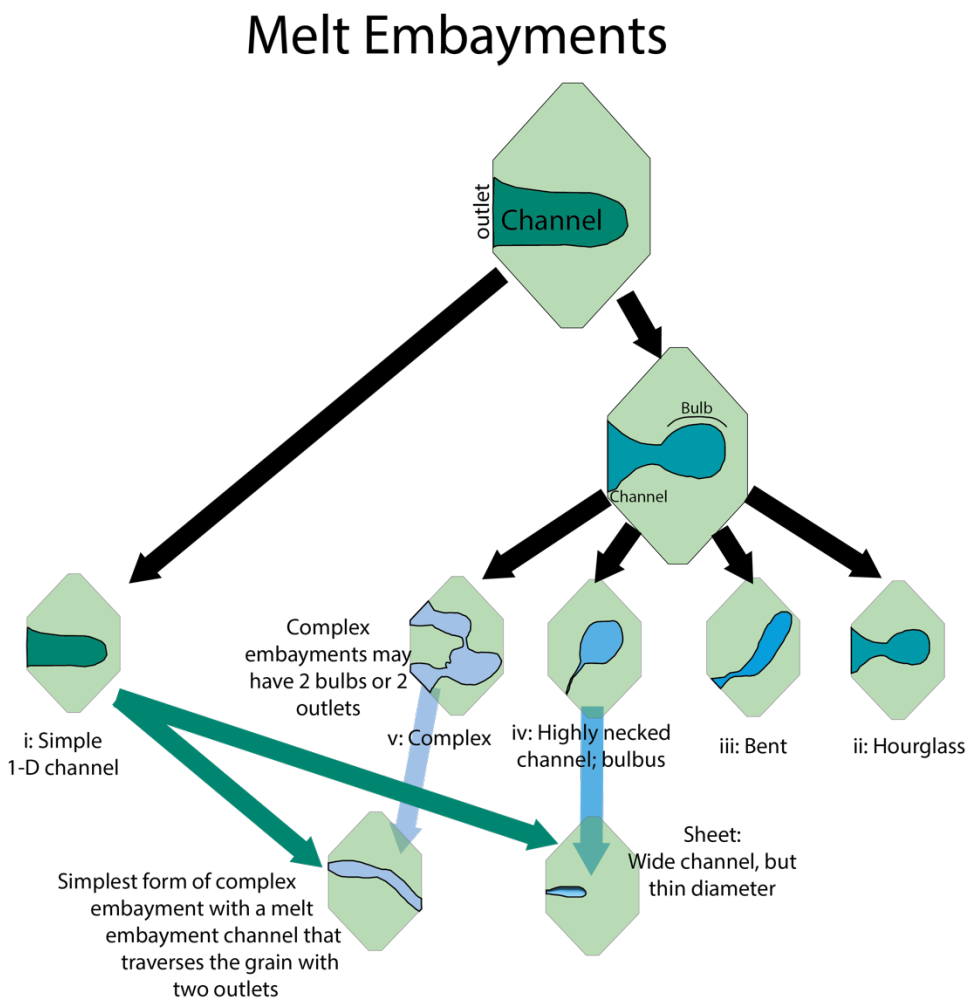

Figure 4.5. Cartoon hierarchy of types of embayments observed.**Simple 1-D:** cylindrical channel shape, typically does not have a bulb

ii. **Hourglass:** Embayment terminates with a bulb, middle of embayment pinches out but flares out by the embayment outlet

iii. **Bent:** Embayment channel sharply bends 80-120□in the channel

iv. Highly necked channel/bulbous: Melt channel >10 microns; bulbs ~20x larger than channel

v. **Complex:** the most diversity in this group. Embayments have multiple channels, bulbs, and/or outlets. Bulbs may be connected by channels that do not have an outlet

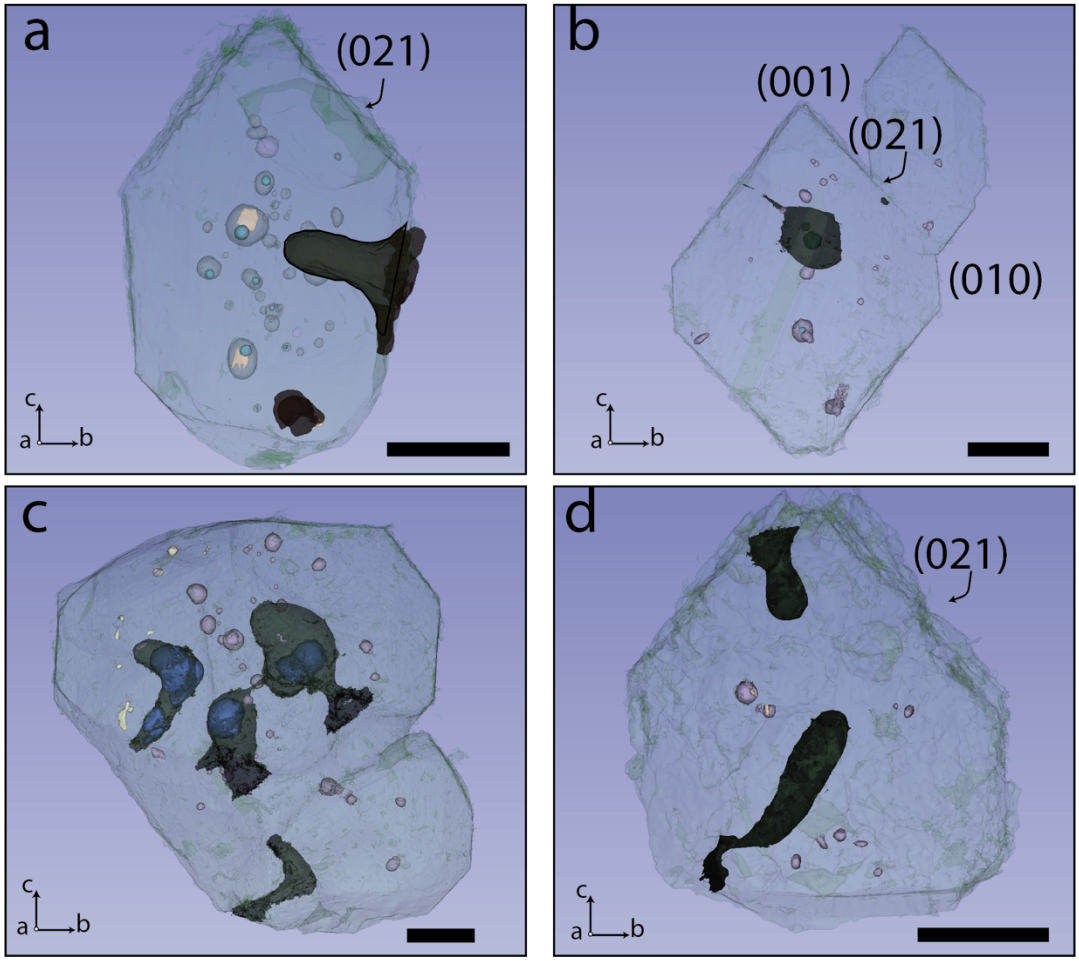

Figure 4.6. Example 3D tomography data of melt embayments in olivine hosts from the 2018 eruption at mount Veniaminof with clear crystal faces defined.Tomographic data was performed at the GeoSoilEnviroCARS (The University of Chicago, Sector 13, Advanced Photon Source, Argonne National Laboratory and segmented using 3D Slicer. In these images, the host olivine is transparent green, the melt embayment is black, melt inclusions are a light lavender, vapor bubbles within inclusions are light blue, bubbles/vesicles in the melt embayment are dark blue, oxides are white. The scale bar at the bottom denotes 100 microns. Videos of these grains spinning are located in the supplementary package. (A) simple embayment on the (010) axis of the host grain; (B) Highly necked and bulbus embayment with two shrinkage bubbles in the body of the embayment attached on the (021) face of the crystal; (C) a highly complex network of melt channels and a necked or hourglass embayments. Melt channels are highly vesiculate. (D) an hourglass embayment attached to the (001) plane and a kinked embayment on the {110} face.

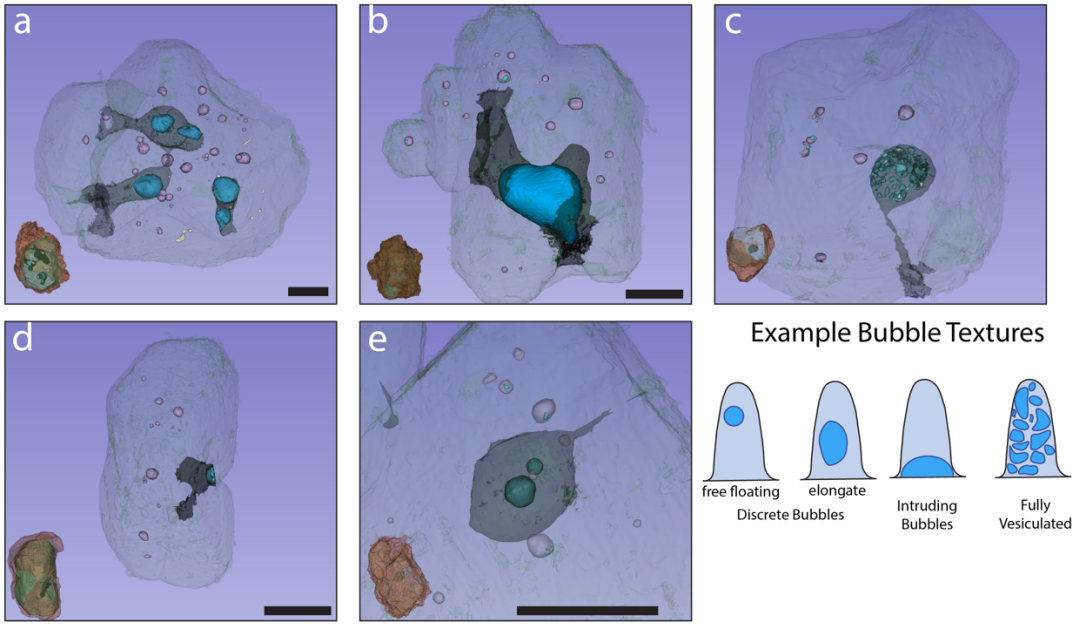

Figure 4.7. . Example 3D tomography data of bubbles and vesicles.

Tomographic data was performed at the GeoSoilEnviroCARS (The University of Chicago, Sector 13, Advanced Photon Source, Argonne National Laboratory and segmented using 3D Slicer). (A) Elongate bubbles intruding into a highly complex grain; (B) An elongate bubble in the middle of a complex melt embayment; (C) A fully vesiculated bulb of a melt embayment. (D) An intruding bubble at the interface between the external melt and embayment channel; (E) Two discrete, free floating bubbles in a highly necked embayment

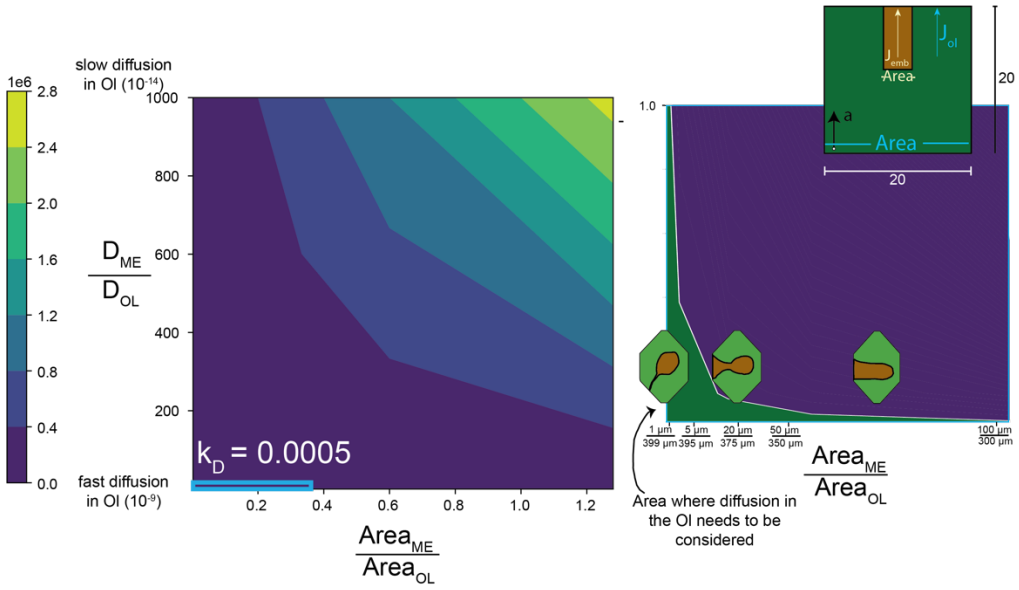

Figure 4.8. Model set up to compare the influences of diffusion through the melt embayment and diffusion through the olivine.

In the upper right corner is the basic model set up of an embayment in the host olivine grain (20x20 area). Area of the embayment is a function of how much necking the embayment has. On the bottom is a contour plot to see where diffusion through the olivine matters with corresponding melt embayment geometry. We find that for a K_d of 0.0001 there is only a small section where diffusion through the olivine needs to be considered (the box to the right) that corresponds with fast diffusion through the olivine and a high degree with necking. With a higher K_d, the area where one needs to consider diffusion through the host olivine expands.

Appendix

Supplementary documentation:

- Text on the methodology of segmentations using 3D Slicer
- Videos of the 3D volumes presented in this chapter (will be stored in a data repository)
- Supplementary excel file with Sample descriptions and more images of the 3D volumes
- **Supporting text:**

3D-Slicer:

In 3D slicer, we segmented grains via thresholding, painting phases present in each slice, or level-tracing areas of uniform intensity (Figure 1). Each slice of the micro-CT data does not need to be segmented. Instead, fast segmentation is completed through a GrowCut algorithm (Zhu et al., 2014) based on the chosen painted segment locations, sizes, shapes, and densities. After initializing the GrowCut algorithm, the segments can be modified and updated if the initial results are incorrect. Using this method, 3D images with defined features can be quickly created. By increasing the number of segments, the definition of many small features (for example, small >10 μm melt inclusions, bubbles, oxides), and segments with similar gray values (for example, highlighting a melt embayment from the surrounding melt around a crystal) can increase the processing time for initialization, or the processing of the segments with the GrowCut algorithm, to be completed.

Segments of olivine grains were completed using the “paint” feature to remove surrounding dental resin and dust particles present in the mount and to highlight melt embayments in the crystal as well as “level tracing” to define boundaries between the external silicate melt, olivine, melt inclusions and shrinkage bubbles (Figure 1). Segments were created on slices where the phases appeared and disappeared to define their boundaries in the models. After the segmented model was initialized, anomalously segmented pixels were corrected. Once segments are defined, their volume can be calculated using the segment statistics module. Segment statistics provide the number of voxels defining a segment, and if the conversion of a voxel to unit length is known, it can be converted to the volume or surface area of a segment. It should be noted that this involves calculating the volume of every instance of the phase that is under the segment. That is, if the volume of a singular shrinkage bubble in a melt inclusion is of interest, it should be defined as its own segment.

CHAPTER 5: Conclusion to the dissertation

Chapter 5: Conclusion

In this dissertation, thermodynamic modeling, chemical analyses, and creation of 3D volumes were employed to better assess ascent rate calculations and determinations of magma storage for the 2018 eruption at Mount Veniaminof. In the second chapter, I evaluated the implication that the lack of microlites in rocks is formed during time periods of fast ascent. I find that microlite growth can be inhibited by thermal disruptions (i.e. magma recharge) prior to eruption, increasing timescales of ascent. The novel approach of this research lies in modeling disequilibrium processes within the MELTS framework, where there is the implicit assumption that the system is in equilibrium.

In the third chapter, I analyzed olivine hosted melt inclusions from the 2018 eruption at Mount Veniaminof to assess whether volatiles played a role in the November paroxysm and contributed direct volatile analyses to a section of the Aleutian Arc lacking that data. Chapter four builds upon the 2018 eruption dataset to include a detailed textural study of melt embayments hosted in olivine derived from 3D volumes and shows that melt embayments in host minerals with variable habits may preserve a different decompression rate history than embayments in single crystal hosts. In highly necked embayments, diffusion through the host olivine grain is possible, leading to underestimates of ascent rates. This also has implication for olivine hosted melt inclusion, where a crack that forms in an inclusion (i.e., a small pathway) may not lead to more substantiative H^+ loss in the inclusion, when considering the volatile loss already

occurring through the host. We also find that bubbles that form within the embayments can possibly travel through the embayment channel leading to inaccurate ascent rates.

Future Directions:

The affinities modeling in chapter two focused on the dissolution of plagioclase crystals due to magma recharge. Future iterations of this modeling should consider crystal growth, but by means of separating nucleation of nanolites and microlites and the growth of crystals. This code could be levered in tandem with experimental set ups to help discern the different mechanisms of crystal growth. This code should also be expanded to other mineral phases to better approximate natural systems.

To better understand the degassing of H_2O from melt inclusions, crystallographic axes of the host grain can be determined by segmenting 3-D models of the grain via micro-CT or after polishing by using electron backscatter diffraction (EBSD) to determine the crystallographic axes of the polished sliced to better pinpoint the location of the melt inclusions in relation to the a-axis of the olivine. Rehomogenizing a subsect of melt inclusions with mineral precipitates around the bubble could determine how much we are underestimating the CO_2 budget (i.e. the depth of storage) at Mount Veniaminof. Melt inclusions at Mount Veniaminof could also be extended to past eruptions to understand how the volatile budget of magmas and storage history have changed through time. An analysis of a melt inclusion from a prior eruption with a similar composition to the

melt inclusions measured from the 2018 eruption has a concentration of H_2O ~3 wt.%. Further studies could elucidate if this is representative, and the impact this has on our models of magma storage for Veniaminof.

Melt embayments have the potential to be expanded to accommodate more complex geometries if accompanied by 3D modeling. Necked embayment geometries with attachments on different crystallographic faces (i.e., {110} versus the {021}) are candidates to be analyzed via Fourier Transform Infrared Light Spectroscopy to map distribution of H_2O in olivine grains around the embayments to better understand the influence of diffusion through the host olivine. After the embayments are analyzed via nanoSIMS or FTIR, element maps of incompatible elements in the host olivine via electron microprobe could further elucidate the growth and thermal histories of the olivine grain. This method has the potential to be extended to encompass additional systems to more accurately determine the prevalence of intricate embayment geometries. While previous research has primarily focused on basic 1-D embayments, a more comprehensive understanding can be achieved by employing this technique in a broader context.

References

Chapter 1:

Liu, Y., Anderson, A. T., & Wilson, C. J. N. (2007). Melt pockets in phenocrysts and decompression rates of silicic magmas before fragmentation. *Journal of Geophysical Research: Solid Earth*, *112*(B6), 2006JB004500. https://doi.org/10.1029/2006JB004500

Wei, S. S., Ruprecht, P., Gable, S. L., Huggins, E. G., Ruppert, N., Gao, L., & Zhang, H. (2021). Along-strike variations in intermediate-depth seismicity and arc magmatism along the Alaska Peninsula. *Earth and Planetary Science Letters*, *563*, 116878. https://doi.org/10.1016/j.epsl.2021.116878

Zimmer, M. M., Plank, T., Hauri, E. H., Yogodzinski, G. M., Stelling, P., Larsen, J., Singer, B., Jicha, B., Mandeville, C., & Nye, C. J. (2010). The Role of Water in Generating the Calc-alkaline Trend: New Volatile Data for Aleutian Magmas and a New Tholeiitic Index. *Journal of Petrology*, *51*(12), 2411–2444. https://doi.org/10.1093/petrology/egq062

Chapter 2:

Alexander, C. M. D. (2011), Modeling diffusive dissolution in silicate melts. *Geochimica et Cosmochimica Acta*, *75*(2), 588-607. doi: 10.1016/j.gca.2010.10.026.

Andrews, B. J., & Befus, K. S. (2020). Supersaturation nucleation and growth of plagioclase: a numerical model of decompression-induced crystallization. *Contributions to Mineralogy and Petrology*, *175*(3), 1-20. doi: 10.1007/s00410-020-1660-9

Arzilli, F., & Carroll, M. R. (2013), Crystallization kinetics of alkali feldspars in cooling and decompression-induced crystallization experiments in trachytic melt. *Contributions to Mineralogy and Petrology*, *166*(4), 1011-1027. doi: 10.1007/s00410-013-0906-1

Barth, A., Newcombe, M., Plank, T., Gonnermann, H., Hajimirza, S., Soto, G.J., Saballos, A., & Hauri, E., (2019), Magma decompression rate correlates with explosivity at basaltic volcanoes — Constraints from water diffusion in olivine. *Journal of Volcanology and Geothermal Research* 387, 106664. doi: 10.1016/j.jvolgeores.2019.106664

Befus, K. S., & Andrews, B. J. (2018), Crystal nucleation and growth produced by continuous decompression of Pinatubo magma. *Contributions to Mineralogy and Petrology*, *173*(11), 92. doi: 10.1007/s00410-018-1519-5

Berman, R. G. (1988), Internally-consistent thermodynamic data for minerals in the system Na2O-K2O-CaO-MgO-FeO-Fe2O3-Al2O3-SiO2-TiO2-

H2O-CO2. *Journal of Petrology*, *29*(2), 445-522. doi:10.1093/petrology/29.2.445

Blundy, J., & Cashman, K. (2001), Ascent-driven crystallization of dacite magmas at Mount St Helens, 1980-1986. *Contributions to Mineralogy and Petrology*, *140*(6), 631–650. doi:10.1007/s004100000219

Blundy, J., Cashman, K., & Humphreys, M. (2006), Magma heating by decompression-driven crystallization beneath andesite volcanoes. *Nature*, *443*(7), 76-80. doi: 10.1038/nature05100

Blundy, J., & Cashman, K. (2008), Petrologic reconstruction of magmatic system variables and processes. *Reviews in Mineralogy and Geochemistry*, *69*(1), 179-239. doi: 10.2138/rmg.2008.69.6

Brugger, C. R., & Hammer, J. E. (2010), Crystallization kinetics in continuous decompression experiments: implications for interpreting natural magma ascent processes. *Journal of Petrology*, *51*(9), 1941-1965. doi:10.1093/petrology/egq044

Cassidy, M., Manga, M., Cashman, K., & Bachmann, O. (2018). Controls on explosive-effusive volcanic eruption styles. *Nature communications*, *9*(1), 1-16. doi:10.1038/s41467-018-05293-3

Castro, J.M., & Dingwell, D.B. (2009), Rapid ascent of rhyolitic magma at Chaitén volcano, Chile. *Nature*, *461*(8), 780–783. doi: 10.1038/nature08458

Couch, S., Harford, C. L., Sparks, R. S. J., & Carroll, M. R. (2003), Experimental constraints on the conditions of formation of highly calcic plagioclase microlites at the Soufrire Hills Volcano, Montserrat. *Journal of Petrology*, *44*(8), 1455-1475. doi:10.1093/petrology/44.8.1455

Crameri, F. (2018a), Scientific colour-maps. Zenodo. http://doi.org/10.5281/zenodo.1243862

Crameri, F., G.E. Shephard, and P.J. Heron (2020), The misuse of colour in science communication, Nature Communications, 11, 5444. doi: 10.1038/s41467-020-19160-7

Davidson, J. P., Hora, J. M., Garrison, J. M., & Dungan, M. A. (2005). Crustal forensics in arc magmas. *Journal of Volcanology and Geothermal Research*, *140*(1-3), 157-170. doi: 10.1016/j.jvolgeores.2004.07.019

Degruyter, W., Huber, C., Bachmann, O., Cooper, K. M., & Kent, A. J. (2016), Magma reservoir response to transient recharge events: The case of Santorini volcano (Greece). *Geology*, *44*(1), 23-26. doi: 10.1130/g37333.1

Degruyter, W., Huber, C., Bachmann, O., Cooper, K. M., & Kent, A. J. (2017), Influence of exsolved volatiles on reheating silicic magmas by recharge and consequences for eruptive style at Volcán Quizapu

(Chile). *Geochemistry, Geophysics, Geosystems*, *18*(11), 4123-4135. doi:10.1002/2017GC007219

Dowty, E. (1980), Crystal growth and nucleation theory and the numerical simulation of igneous crystallization. *Physics of magmatic processes*.

Edwards, B. R., & Russell, J. K. (1998), Time scales of magmatic processes: new insights from dynamic models for magmatic assimilation. *Geology*, *26*(12), 1103-1106. doi: 10.1130/0091-7613(1998)026<1103:TSOMPN>2.3.CO;2

Evans, B. W., & Bachmann, O. (2013). Implications of equilibrium and disequilibrium among crystal phases in the Bishop Tuff. *American Mineralogist*, *98*(1), 271-274. doi: 10.2138/am.2013.4280

First, E. C., Leonhardi, T. C., & Hammer, J. E. (2020), Effects of superheating magnitude on olivine growth. *Contributions to Mineralogy and Petrology*, *175*(2), 1-14.

First E., Hammer J., Ruprecht P., Rutherford M. (2021), Experimental constraints on dacite magma storage beneath Volcán Quizapu, Chile. *Journal of Petrology,* egab027, doi.org: 10.1093/petrology/egab027

Gaetani, G. A., O'Leary, J. A., Shimizu, N., Bucholz, C. E., and Newville, M. (2012), Rapid reequilibration of H_2O and oxygen fugacity in olivine-hosted melt inclusions. *Geology* 40 (10), 915–918. doi:10.1130/g32992.1

Ghiorso, M. S. (1987), Chemical mass-transfer in magmatic processes. 3. crystal-growth, chemical diffusion and thermal-diffusion in multicomponent silicate melts. *Contributions to Mineralogy and Petrology*, *96*(3), 291-313.

Ghiorso, M. S., & Sack, R. O. (1995), Chemical mass transfer in magmatic processes IV. A revised and internally consistent thermodynamic model for the interpolation and extrapolation of liquid-solid equilibria in magmatic systems at elevated temperatures and pressures. *Contributions to Mineralogy and Petrology*, *119*(2-3), 197-212.

Ghiorso, M. S. (2013), A globally convergent saturation state algorithm applicable to thermodynamic systems with a stable or metastable omni-component phase. *Geochimica et Cosmochimica Acta*, *103*, 295-300. doi: 10.1016/j.gca.2012.11.013

Ghiorso, M. S., & Gualda, G. A. (2015), An H 2 O–CO 2 mixed fluid saturation model compatible with rhyolite-MELTS. *Contributions to Mineralogy and Petrology*, *169*(6), 53.

Ginibre, C., Kronz, A., & Wörner, G. (2002), High-resolution quantitative imaging of plagioclase composition using accumulated backscattered electron images: new constraints on oscillatory zoning. *Contributions to*

Mineralogy and Petrology, *142*(4), 436-448. doi: 10.1007/s00410-015-1141-8

Ginibre, C., Wörner, G., & Kronz, A. (2007), Crystal zoning as an archive for magma evolution. *Elements*, *3*(4), 261-266. doi: 10.2113/gselements.3.4.261

Gonnermann, H. M., & Manga, M. (2007). The fluid mechanics inside a volcano. *Annual Review of Fluid Mechanics*, *39*, 321-356. doi: 10.1146/annurev.fluid.39.050905.110207

Grove, T.L., Baker, M.B., & Kinzler, R.J. (1984), Coupled CaAl-NaSi diffusion in plagioclase feldspar: Experiments and applications to cooling rate speedometry. *Geochimica et Cosmochimica Acta*, 48, 2113–2121. doi: 10.1016/0016-7037(84)90391-0)

Gualda, G. A., Ghiorso, M. S., Lemons, R. V., & Carley, T. L. (2012), Rhyolite-MELTS: a modified calibration of MELTS optimized for silica-rich, fluid-bearing magmatic systems. *Journal of Petrology*, *53*(5), 875-890. doi:10.1093/petrology/egr080

Hammer, J. E., Cashman, K. V., Hoblitt, R. P., & Newman, S. (1999). Degassing and microlite crystallization during pre-climactic events of the 1991 eruption of Mt. Pinatubo, Philippines. *Bulletin of Volcanology*, *60*(5), 355-380.

Hammer, J. E., & Rutherford, M. J. (2002), An experimental study of the kinetics of decompression-induced crystallization in silicic melt. *Journal of Geophysical Research: Solid Earth*, *107*(B1), ECV-8. doi: 10.1029/2001JB000281

Huggins, E. G., Ruprecht, P., & Ghiorso, M. (2021), Plagioclase Chemical Affinities (Version v.1.0). Zenodo. http://doi.org/10.5281/zenodo.4723866

Humphreys, M.C.S., Menand, T., Blundy, J.D., & Klimm, K. (2008), Magma ascent rates in explosive eruptions: Constraints from H2O diffusion in melt inclusions. *Earth and Planetary Science Letters 270*(1-2), 25–40. doi:10.1016/j.epsl.2008.02.041

Kent, A. J. (2008). Melt inclusions in basaltic and related volcanic rocks. *Reviews in Mineralogy and Geochemistry*, *69*(1), 273-331.

Lange, R. A., Frey, H. M., & Hector, J. (2009), A thermodynamic model for the plagioclase-liquid hygrometer/thermometer. *American Mineralogist*, *94*(4), 494-506. doi: 10.2138/am.2009.3011

Lasaga, A. C. (1982). Toward a master equation in crystal growth. *American Journal of Science*, *282*(8), 1264-1288.

La Spina, G., Burton, M., Vitturi, M. D. M., & Arzilli, F. (2016), Role of syn-eruptive plagioclase disequilibrium crystallization in basaltic magma

ascent dynamics. *Nature communications*, *7*(1), 1-10. doi: 10.1038/ncomms13402

Liu, Y., Zhang, Y., & Behrens, H. (2005), Solubility of H2O in rhyolitic melts at low pressures and a new empirical model for mixed H2O–CO2 solubility in rhyolitic melts. *Journal of Volcanology and Geothermal Research*, *143*(1-3), 219-235. doi:10.1016/j.jvolgeores.2004.09.019

Lloyd, A., Plank, T., Ruprecht, P., Hauri, E., Rose, W. (2013), Volatile Loss from Melt Inclusions in Pyroclasts of Differing Sizes. *Contributions to Mineralogy and Petrology* 165, 129–153. https://doi.org/10.1007/s00410-012-0800-2

Lloyd, A.S., Ruprecht, P., Hauri, E.H., Rose, W., Gonnermann, H.M., & Plank, T. (2014), NanoSIMS results from olivine-hosted melt embayments: Magma ascent rate during explosive basaltic eruptions. *Journal of Volcanology and Geothermal Research*, *283*(2014), 1–18. doi:10.1016/j.jvolgeores.2014.06.002

Martel, C. (2012), Eruption dynamics inferred from microlite crystallization experiments: application to Plinian and dome-forming eruptions of Mt. Pelée (Martinique, Lesser Antilles). *Journal of Petrology*, *53*(4), 699-725. doi:10.1093/petrology/egr076

Métrich, N., Bertagnini, A., & Di Muro, A. (2010), Conditions of magma storage, degassing and ascent at Stromboli: new insights into the volcano plumbing system with inferences on the eruptive dynamics. *Journal of Petrology*, *51*(3), 603-626. doi:10.1093/petrology/egp083

Mollard, E., Martel, C., & Bourdier, J. L. (2012), Decompression-induced crystallization in hydrated silica-rich melts: empirical models of experimental plagioclase nucleation and growth kinetics. *Journal of Petrology*, *53*(8), 1743-1766. doi: 10.1093/petrology/egs031

Mollo, S., Putirka, K., Iezzi, G., Del Gaudio, P., & Scarlato, P. (2011), Plagioclase–melt (dis) equilibrium due to cooling dynamics: implications for thermometry, barometry and hygrometry. *Lithos*, *125*(1-2), 221-235. doi:10.1016/j.lithos.2011.02.008

Mollo, S., & Hammer, J. E. (2017), Dynamic crystallization in magmas. *EMU Notes in Mineralogy*, *16*, 373-418.

Morse, S. A. (1984), Cation diffusion in plagioclase feldspar. *Science*, *225*(4661), 504-505. doi: 10.1126/science.225.4661.504

Newman, S., & Lowenstern, J. B. (2002), VolatileCalc: a silicate melt–H2O–CO2 solution model written in Visual Basic for excel. *Computers & Geosciences*, *28*(5), 597-604. doi:10.1016/S0098-3004(01)00081-4

Ruprecht, P., & Wörner, G. (2007), Variable regimes in magma systems documented in plagioclase zoning patterns: El Misti stratovolcano and Andahua monogenetic cones. *Journal of Volcanology and Geothermal Research*, *165*(3-4), 142–162. doi: 10.1016/j.jvolgeores.2007.06.002

Ruprecht, P., & Bachmann, O. (2010), Pre-eruptive reheating during magma mixing at Quizapu volcano and the implications for the explosiveness of silicic arc volcanoes. *Geology, 38*(10), 919-922. doi: 10.1130/G31110.1

Ruprecht, P., Bergantz G., Cooper K., & Hildreth W. (2012), The crustal magma storage system of Volcán Quizapu, Chile, and the effects of magma mixing on magma diversity. *Journal of Petrology, 53*(4), 801-840. doi:10.1093/petrology/EGS002

Rutherford, M. J. (2008), Magma ascent rates. *Reviews in Mineralogy and Geochemistry*, *69*(1), 241-271. doi:10.2138/rmg.2008.69.7

Sisson, T.W., Grove, T.L. (1993), Experimental investigations of the role of H2O in calc-alkaline differentiation and subduction zone magmatism. *Contributions to Mineralogy and Petrology*, *113*(2), 143–166.

Streck, M. J. (2008), Mineral textures and zoning as evidence for open system processes. *Reviews in Mineralogy and Geochemistry*, *69*(1), 595-622. doi: 10.2138/rmg.2008.69.15

Sunagawa, I. (1992), In situ investigation of nucleation, growth, and dissolution of silicate crystals at high temperatures. *Annual Review of Earth and Planetary Sciences*, *20*(1), 113-142. doi:10.1146/annurev.ea.20.050192.000553

Tsuchiyama, A. (1983), Crystallization kinetics in the system CaMgSi 2 O 6-CaAl 2 Si 2 O 8; the delay in nucleation of diopside and anorthite. *American Mineralogist*, *68*(7-8), 687-698.

Turnbull, D., & Cohen, M. H. (1960), Crystallization kinetics and glass formation. *Modern aspects of the vitreous state*, *1*, 38-62.

Waters, L. E., & Lange, R. A. (2015), An updated calibration of the plagioclase-liquid hygrometer-thermometer applicable to basalts through rhyolites. *American Mineralogist*, *100*(10), 2172-2184. doi: 10.2138/am-2015-5232

Waters, L. E., Andrews, B. J., & Lange, R. A. (2015), Rapid crystallization of plagioclase phenocrysts in silicic melts during fluid-saturated ascent: phase equilibrium and decompression experiments. *Journal of Petrology*, *56*(5), 981-1006. doi:10.1093/petrology/egv025

Chapter 3:

Aster, E. M., Wallace, P. J., Moore, L. R., Watkins, J., Gazel, E., & Bodnar, R. J. (2016). Reconstructing CO2 concentrations in basaltic melt inclusions using Raman analysis of vapor bubbles. *Journal of Volcanology and Geothermal Research*, *323*, 148–162. https://doi.org/10.1016/j.jvolgeores.2016.04.028

Bacon, C. R., Sisson, T. W., Calvert, A. T., & Nye, C. J. (2009). *Geologic Map and Eruptive History of Veniaminof Volcano Record Aleutian Arc Processing of Mantle-Derived Melts*. *2009*, V51A-1652.

Bacon, C. R., Sisson, T. W., & Mazdab, F. K. (2007). Young cumulate complex beneath Veniaminof caldera, Aleutian arc, dated by zircon in erupted plutonic blocks. *Geology*, *35*(6), 491. https://doi.org/10.1130/G23446A.1

Barth, A., Newcombe, M., Plank, T., Gonnermann, H., Hajimirza, S., Soto, G. J., Saballos, A., & Hauri, E. (2019). Magma decompression rate correlates with explosivity at basaltic volcanoes—Constraints from water diffusion in olivine. *Journal of Volcanology and Geothermal Research*, *387*, 106664. https://doi.org/10.1016/j.jvolgeores.2019.106664

Barth, A., & Plank, T. (2021). The Ins and Outs of Water in Olivine-Hosted Melt Inclusions: Hygrometer vs. Speedometer. *Frontiers in Earth Science*, *9*, 614004. https://doi.org/10.3389/feart.2021.614004

Batanova, V. G., & Sobolev, A. V. (2023). Development of Reference Materials for Microanalysis in Geosciences: The Case of Olivine MongOL Sh11–2. *Microscopy and Microanalysis*, *29*(Supplement_1), 227–228. https://doi.org/10.1093/micmic/ozad067.101

Batanova, V. G., Thompson, J. M., Danyushevsky, L. V., Portnyagin, M. V., Garbe-Schönberg, D., Hauri, E., Kimura, J., Chang, Q., Senda, R., Goemann, K., Chauvel, C., Campillo, S., Ionov, D. A., & Sobolev, A. V. (2019). New Olivine Reference Material for *In Situ* Microanalysis. *Geostandards and Geoanalytical Research*, *43*(3), 453–473. https://doi.org/10.1111/ggr.12266

Bennington, N., Haney, M., Thurber, C., & Zeng, X. (2018). Inferring Magma Dynamics at Veniaminof Volcano Via Application of Ambient Noise. *Geophysical Research Letters*, *45*(21). https://doi.org/10.1029/2018GL079909

Blatter, D. L., Sisson, T. W., & Hankins, W. B. (2013). Crystallization of oxidized, moderately hydrous arc basalt at mid- to lower-crustal pressures: Implications for andesite genesis. *Contributions to Mineralogy and Petrology*, *166*(3), 861–886. https://doi.org/10.1007/s00410-013-0920-3

Bucholz, C. E., Gaetani, G. A., Behn, M. D., & Shimizu, N. (2013). Post-entrapment modification of volatiles and oxygen fugacity in olivine-hosted melt inclusions. *Earth and Planetary Science Letters*, *374*, 145–155. https://doi.org/10.1016/j.epsl.2013.05.033

Buurman, H., Nye, C. J., West, M. E., & Cameron, C. (2014). Regional controls on volcano seismicity along the Aleutian arc. *Geochemistry, Geophysics, Geosystems*, *15*(4), 1147–1163. https://doi.org/10.1002/2013GC005101

Caricchi, L., Sheldrake, T. E., & Blundy, J. (2018). Modulation of magmatic processes by CO2 flushing. *Earth and Planetary Science Letters*, *491*, 160–171. https://doi.org/10.1016/j.epsl.2018.03.042

Cashman, K. V., & Rust, A. (2016). *Causes and implications of suppressed vesiculation and crystallization in phenocryst embayments*. *2016*, V13G-02.

Castro, J. M., & Dingwell, D. B. (2009). Rapid ascent of rhyolitic magma at Chaitén volcano, Chile. *Nature*, *461*(7265), 780–783. https://doi.org/10.1038/nature08458

Coogan, L. A., Hain, A., Stahl, S., & Chakraborty, S. (2005). Experimental determination of the diffusion coefficient for calcium in olivine between 900°C and 1500°C. *Geochimica et Cosmochimica Acta*, *69*(14), 3683–3694. https://doi.org/10.1016/j.gca.2005.03.002

Cooper, L. B., Ruscitto, D. M., Plank, T., Wallace, P. J., Syracuse, E. M., & Manning, C. E. (2012). Global variations in H_2O/Ce: 1. Slab surface temperatures beneath volcanic arcs. *Geochemistry, Geophysics, Geosystems*, *13*(3), 2011GC003902. https://doi.org/10.1029/2011GC003902

Costa, F., & Morgan, D. (2010). Time Constraints from Chemical Equilibration in Magmatic Crystals. In A. Dosseto, S. P. Turner, & J. A. Van Orman (Eds.), *Timescales of Magmatic Processes* (1st ed., pp. 125–159). Wiley. https://doi.org/10.1002/9781444328509.ch7

Couch, S. (2003). The Kinetics of Degassing-Induced Crystallization at Soufriere Hills Volcano, Montserrat. *Journal of Petrology*, *44*(8), 1477–1502. https://doi.org/10.1093/petrology/44.8.1477

Danyushevsky, L. V., McNeill, A. W., & Sobolev, A. V. (2002). Experimental and petrological studies of melt inclusions in phenocrysts from mantle-derived magmas: An overview of techniques, advantages and complications. *Chemical Geology*, *183*(1–4), 5–24. https://doi.org/10.1016/S0009-2541(01)00369-2

Danyushevsky, L. V., & Plechov, P. (2011). Petrolog3: Integrated software for modeling crystallization processes: PETROLOG3. *Geochemistry, Geophysics, Geosystems*, *12*(7), n/a-n/a. https://doi.org/10.1029/2011GC003516

deGraffenried, R. L., & Shea, T. (2021). Using Volatile Element Concentration Profiles in Crystal-Hosted Melt Embayments to Estimate Magma Decompression Rate: Assumptions and Inherited Errors. *Geochemistry, Geophysics, Geosystems*, *22*(5). https://doi.org/10.1029/2021GC009672

DeVitre, C. L., Allison, C. M., & Gazel, E. (2021). A high-precision CO2 densimeter for Raman spectroscopy using a Fluid Density Calibration Apparatus. *Chemical Geology*, *584*, 120522. https://doi.org/10.1016/j.chemgeo.2021.120522

Donovan, J. J., Singer, J. W., & Armstrong, J. T. (2016). A new EPMA method for fast trace element analysis in simple matrices. *American Mineralogist*, *101*(8), 1839–1853. https://doi.org/10.2138/am-2016-5628

Dowty, E. (1980). Synneusis Reconsidered. *Contributions to Mineralogy and Petrology*, *74*(1), 75–84. https://doi.org/10.1007/BF00375491

Esposito, R., Hunter, J., Schiffbauer, J. D., Shimizu, N., & Bodnar, R. J. (2014). An assessment of the reliability of melt inclusions as recorders of the pre-eruptive volatile content of magmas. *American Mineralogist*, *99*(5–6), 976–998. https://doi.org/10.2138/am.2014.4574

Faure, F., & Schiano, P. (2005). Experimental investigation of equilibration conditions during forsterite growth and melt inclusion formation. *Earth and Planetary Science Letters*, *236*(3–4), 882–898. https://doi.org/10.1016/j.epsl.2005.04.050

Ferguson, D. J., Gonnermann, H. M., Ruprecht, P., Plank, T., Hauri, E. H., Houghton, B. F., & Swanson, D. A. (2016). Magma decompression rates during explosive eruptions of Kīlauea volcano, Hawaii, recorded by melt embayments. *Bulletin of Volcanology*, *78*(10), 71. https://doi.org/10.1007/s00445-016-1064-x

Gaetani, G. A., O'Leary, J. A., Shimizu, N., Bucholz, C. E., & Newville, M. (2012). Rapid reequilibration of H2O and oxygen fugacity in olivine-hosted melt inclusions. *Geology*, *40*(10), 915–918. https://doi.org/10.1130/G32992.1

Ghiorso, M. S., & Gualda, G. A. R. (2015). An H2O–CO2 mixed fluid saturation model compatible with rhyolite-MELTS. *Contributions to Mineralogy and Petrology*, *169*(6), 53. https://doi.org/10.1007/s00410-015-1141-8

Giordano, D., Russell, J. K., & Dingwell, D. B. (2008). Viscosity of magmatic liquids: A model. *Earth and Planetary Science Letters*, *271*(1–4), 123–134. https://doi.org/10.1016/j.epsl.2008.03.038

Hauri, E. (2002). SIMS analysis of volatiles in silicate glasses, 2: Isotopes and abundances in Hawaiian melt inclusions. *Chemical Geology*, *183*(1–4), 115–141. https://doi.org/10.1016/S0009-2541(01)00374-6

Hauri, E., Wang, J., Dixon, J. E., King, P. L., Mandeville, C., & Newman, S. (2002). SIMS analysis of volatiles in silicate glasses. *Chemical Geology*, *183*(1–4), 99–114. https://doi.org/10.1016/S0009-2541(01)00375-8

Holness, M. B., Farr, R., & Neufeld, J. A. (2017). Crystal settling and convection in the Shiant Isles Main Sill. *Contributions to Mineralogy and Petrology*, *172*(1), 7. https://doi.org/10.1007/s00410-016-1325-x

Hosseini, B., Myers, M. L., Watkins, J. M., & Harris, M. A. (2023). Are We Recording? Putting Embayment Speedometry to the Test Using High Pressure-Temperature Decompression Experiments. *Geochemistry, Geophysics, Geosystems*, *24*(6), e2022GC010770. https://doi.org/10.1029/2022GC010770

Huggins, E. G., Ruprecht, P., & Ghiorso, M. S. (2021). Using Chemical Affinities to Understand Disequilibrium Textures of Plagioclase Preserved in Magmatic Systems. *Geophysical Research Letters*, *48*(10), e2021GL092884. https://doi.org/10.1029/2021GL092884

Humphreys, M. C. S., Menand, T., Blundy, J. D., & Klimm, K. (2008). Magma ascent rates in explosive eruptions: Constraints from H2O diffusion in melt inclusions. *Earth and Planetary Science Letters*, *270*(1–2), 25–40. https://doi.org/10.1016/j.epsl.2008.02.041

Iacovino, K., & Till, C. B. (2019). DensityX: A program for calculating the densities of magmatic liquids up to 1,627 °C and 30 kbar. *Volcanica*, *2*(1), 1–10. https://doi.org/10.30909/vol.02.01.0110

Jarosewich, E. (2002). Smithsonian Microbeam Standards. *Journal of Research of the National Institute of Standards and Technology*, *107*(6), 681. https://doi.org/10.6028/jres.107.054

Jicha, B. R., & Kay, S. M. (2018). Quantifying arc migration and the role of forearc subduction erosion in the central Aleutians. *Journal of Volcanology and Geothermal Research*, *360*, 84–99. https://doi.org/10.1016/j.jvolgeores.2018.06.016

Jochum, K. P., Stoll, B., Herwig, K., Willbold, M., Hofmann, A. W., Amini, M., Aarburg, S., Abouchami, W., Hellebrand, E., Mocek, B., Raczek, I., Stracke, A., Alard, O., Bouman, C., Becker, S., Dücking, M., Brätz, H., Klemd, R., De Bruin, D., … Woodhead, J. D. (2006). MPI-DING reference glasses for in situ microanalysis: New reference values for element concentrations and isotope ratios: MPI-DING REFERENCE GLASSES. *Geochemistry, Geophysics, Geosystems*, *7*(2), n/a-n/a. https://doi.org/10.1029/2005GC001060

Jochum, K. P., Weis, U., Stoll, B., Kuzmin, D., Yang, Q., Raczek, I., Jacob, D. E., Stracke, A., Birbaum, K., Frick, D. A., Günther, D., & Enzweiler, J. (2011). Determination of Reference Values for NIST SRM 610–617 Glasses Following ISO Guidelines. *Geostandards and Geoanalytical Research*, *35*(4), 397–429. https://doi.org/10.1111/j.1751-908X.2011.00120.x

Jochum, K. P., Willbold, M., Raczek, I., Stoll, B., & Herwig, K. (2005). Chemical Characterisation of the USGS Reference Glasses GSA-1G, GSC-1G, GSD-1G, GSE-1G, BCR-2G, BHVO-2G and BIR-1G Using EPMA, ID-TIMS, ID-ICP-MS and LA-ICP-MS. *Geostandards and Geoanalytical Research*, *29*(3), 285–302. https://doi.org/10.1111/j.1751-908X.2005.tb00901.x

Jollands, M. C., Muir, J., Padrón-Navarta, J. A., & Demouchy, S. (2022). Modelling hydrogen mobility in forsterite as diffusion coupled to inter-site reaction. *Contributions to Mineralogy and Petrology*, *177*(10), 98. https://doi.org/10.1007/s00410-022-01954-1

Kay, S. M., & Kay, R. W. (1985). Role of crystal cumulates and the oceanic crust in the formation of the lower crust of the Aleutian arc. *Geology*, *13*(7), 461. https://doi.org/10.1130/0091-7613(1985)13<461:ROCCAT>2.0.CO;2

Kay, S. M., Kay, R. W., & Citron, G. P. (1982). Tectonic controls on tholeiitic and calc-alkaline magmatism in the Aleutian Arc. *Journal of Geophysical Research*, *87*(B5), 4051. https://doi.org/10.1029/JB087iB05p04051

Kent, A. J. R. (2008). Melt Inclusions in Basaltic and Related Volcanic Rocks. *Reviews in Mineralogy and Geochemistry*, *69*(1), 273–331. https://doi.org/10.2138/rmg.2008.69.8

Kumamoto, K. M., Warren, J. M., & Hauri, E. H. (2017). New SIMS reference materials for measuring water in upper mantle minerals. *American Mineralogist*, *102*(3), 537–547. https://doi.org/10.2138/am-2017-5863CCBYNCND

Lamadrid, H. M., Moore, L. R., Moncada, D., Rimstidt, J. D., Burruss, R. C., & Bodnar, R. J. (2017). Reassessment of the Raman CO 2 densimeter. *Chemical Geology*, *450*, 210–222. https://doi.org/10.1016/j.chemgeo.2016.12.034

Lambart, S., Hamilton, S., & Lang, O. I. (2022). Compositional variability of San Carlos olivine. *Chemical Geology*, *605*, 120968. https://doi.org/10.1016/j.chemgeo.2022.120968

Larsen, J. F. (2016). Unraveling the diversity in arc volcanic eruption styles: Examples from the Aleutian volcanic arc, Alaska. *Journal of Volcanology and Geothermal Research*, *327*, 643–668. https://doi.org/10.1016/j.jvolgeores.2016.09.008

Li, Y., Gregg, P. M., Lu, Z., & Wang, J. (2022). *Investigations of open magma system behavior at Veniaminof Volcano, Alaska*. *2022*, V32F-0125.

Liu, Y., Anderson, A. T., & Wilson, C. J. N. (2007). Melt pockets in phenocrysts and decompression rates of silicic magmas before fragmentation. *Journal of Geophysical Research: Solid Earth*, *112*(B6), 2006JB004500. https://doi.org/10.1029/2006JB004500

Lloyd, A. S., Plank, T., Ruprecht, P., Hauri, E. H., & Rose, W. (2013). Volatile loss from melt inclusions in pyroclasts of differing sizes. *Contributions to Mineralogy and Petrology*, *165*(1), 129–153. https://doi.org/10.1007/s00410-012-0800-2

Lloyd, A. S., Ruprecht, P., Hauri, E. H., Rose, W., Gonnermann, H. M., & Plank, T. (2014). NanoSIMS results from olivine-hosted melt embayments: Magma ascent rate during explosive basaltic eruptions. *Journal of Volcanology and Geothermal Research*, *283*, 1–18. https://doi.org/10.1016/j.jvolgeores.2014.06.002

Loewen, M. W., Dietterich, H. R., Graham, N., & Izbekov, P. (2021). Evolution in eruptive style of the 2018 eruption of Veniaminof volcano, Alaska, reflected in groundmass textures and remote sensing. *Bulletin of Volcanology*, *83*(11), 72. https://doi.org/10.1007/s00445-021-01489-6

Lowenstern, J. B., & Thompson, J. F. H. (n.d.). Applications of silicate-melt inclusions to the study of magmatic volatiles. *Magmas, Fluids and Ore Deposits*, *23*, 71–99.

Lubbers, J., Kent, A., Meisenheimer, D., & Wildenschild, D. (2023). 3D zoning of barium in alkali feldspar. *American Mineralogist*, *108*(2), 297–311. https://doi.org/10.2138/am-2022-8139

Lynn, K. J., & Desmither, L. (2023). *Creating Oriented and Precisely Sectioned Mineral Mounts for In Situ Chemical Analyses—An Example Using Olivine for Diffusion*

Chronometry Studies (Techniques and Methods book 5, chap. D5; Techniques and Methods, p. 36 p). U.S. Geological Survey.

Mangan, M., & Sisson, T. (2000). Delayed, disequilibrium degassing in rhyolite magma: Decompression experiments and implications for explosive volcanism. *Earth and Planetary Science Letters*, *183*(3–4), 441–455. https://doi.org/10.1016/S0012-821X(00)00299-5

Martel, C., & Schmidt, B. C. (2003). Decompression experiments as an insight into ascent rates of silicic magmas. *Contributions to Mineralogy and Petrology*, *144*(4), 397–415. https://doi.org/10.1007/s00410-002-0404-3

McIntire, M. Z., Bergantz, G. W., & Schleicher, J. M. (2019). On the hydrodynamics of crystal clustering. *Philosophical Transactions of the Royal Society A: Mathematical, Physical and Engineering Sciences*, *377*(2139), 20180015. https://doi.org/10.1098/rsta.2018.0015

Melt Inclusion Study of the Embryonic Porphyry Copper System at White Island, New Zealand. (2005). In S. F. Simmons & I. Graham, *Volcanic, Geothermal, and Ore-Forming Fluids* (pp. 41–59). Society of Economic Geologists. https://doi.org/10.5382/SP.10.03

Moore, L. R., & Bodnar, R. J. (2019). A pedagogical approach to estimating the CO_2 budget of magmas. *Journal of the Geological Society*, *176*(2), 398–407. https://doi.org/10.1144/jgs2018-094

Moore, L. R., Gazel, E., Tuohy, R., Lloyd, A. S., Esposito, R., Steele-MacInnis, M., Hauri, E. H., Wallace, P. J., Plank, T., & Bodnar, R. J. (2015). Bubbles matter: An assessment of the contribution of vapor bubbles to melt inclusion volatile budgets. *American Mineralogist*, *100*(4), 806–823. https://doi.org/10.2138/am-2015-5036

Mourey, A. J., & Shea, T. (2019). Forming Olivine Phenocrysts in Basalt: A 3D Characterization of Growth Rates in Laboratory Experiments. *Frontiers in Earth Science*, *7*, 300. https://doi.org/10.3389/feart.2019.00300

Moussallam, Y., Rose-Koga, E. F., Koga, K. T., Médard, E., Bani, P., Devidal, J.-L., & Tari, D. (2019). Fast ascent rate during the 2017–2018 Plinian eruption of Ambae (Aoba) volcano: A petrological investigation. *Contributions to Mineralogy and Petrology*, *174*(11), 90. https://doi.org/10.1007/s00410-019-1625-z

Newcombe, M. E., Fabbrizio, A., Zhang, Y., Ma, C., Le Voyer, M., Guan, Y., Eiler, J. M., Saal, A. E., & Stolper, E. M. (2014). Chemical zonation in olivine-hosted melt inclusions. *Contributions to Mineralogy and Petrology*, *168*(1), 1030. https://doi.org/10.1007/s00410-014-1030-6

Newcombe, M. E., Plank, T., Barth, A., Asimow, P. D., & Hauri, E. (2020). Water-in-olivine magma ascent chronometry: Every crystal is a clock. *Journal of Volcanology and Geothermal Research*, *398*, 106872. https://doi.org/10.1016/j.jvolgeores.2020.106872

Oeser, M., Ruprecht, P., & Weyer, S. (2018). Combined Fe-Mg chemical and isotopic zoning in olivine constraining magma mixing-to-eruption timescales for the continental arc volcano Irazú (Costa Rica) and Cr diffusion in olivine. *American Mineralogist*, *103*(4), 582–599. https://doi.org/10.2138/am-2018-6258

Pesicek, J. D., Wellik, J. J., Prejean, S. G., & Ogburn, S. E. (2018). Prevalence of Seismic Rate Anomalies Preceding Volcanic Eruptions in Alaska. *Frontiers in Earth Science*, *6*, 100. https://doi.org/10.3389/feart.2018.00100

Plank, T. (2005). Constraints from Thorium/Lanthanum on Sediment Recycling at Subduction Zones and the Evolution of the Continents. *Journal of Petrology*, *46*(5), 921–944. https://doi.org/10.1093/petrology/egi005

Plank, T., Kelley, K. A., Zimmer, M. M., Hauri, E. H., & Wallace, P. J. (2013). Why do mafic arc magmas contain ~4wt% water on average? *Earth and Planetary Science Letters*, *364*, 168–179. https://doi.org/10.1016/j.epsl.2012.11.044

Portnyagin, M., Almeev, R., Matveev, S., & Holtz, F. (2008). Experimental evidence for rapid water exchange between melt inclusions in olivine and host magma. *Earth and Planetary Science Letters*, *272*(3–4), 541–552. https://doi.org/10.1016/j.epsl.2008.05.020

Portnyagin, M., Mironov, N., Botcharnikov, R., Gurenko, A., Almeev, R. R., Luft, C., & Holtz, F. (2019). Dehydration of melt inclusions in olivine and implications for the origin of silica-undersaturated island-arc melts. *Earth and Planetary Science Letters*, *517*, 95–105. https://doi.org/10.1016/j.epsl.2019.04.021

Putirka, K. D. (2008). Thermometers and Barometers for Volcanic Systems. *Reviews in Mineralogy and Geochemistry*, *69*(1), 61–120. https://doi.org/10.2138/rmg.2008.69.3

Qin, Z., Fangqiong, L., & Anderson, A. (1992). Diffusive reequilibration of melt and fluid inclusions. *American Mineralogist*, *77*(5–6), 565–576.

Rasmussen, D. J., Plank, T. A., Roman, D. C., & Zimmer, M. M. (2022). Magmatic water content controls the pre-eruptive depth of arc magmas. *Science*, *375*(6585), 1169–1172. https://doi.org/10.1126/science.abm5174

Rasmussen, D. J., Plank, T. A., Wallace, P. J., Newcombe, M. E., & Lowenstern, J. B. (2020). Vapor-bubble growth in olivine-hosted melt inclusions. *American Mineralogist*, *105*(12), 1898–1919. https://doi.org/10.2138/am-2020-7377

Roeder, E. (1979). Origin and significance of magmatic inclusions. Bulletin de Mineralogie. *Bulletin de Mineralogie*, *102*(5), 487–510.

Rose-Koga, E. F., Bouvier, A.-S., Gaetani, G. A., Wallace, P. J., Allison, C. M., Andrys, J. A., Angeles De La Torre, C. A., Barth, A., Bodnar, R. J., Bracco Gartner, A. J. J., Butters, D., Castillejo, A., Chilson-Parks, B., Choudhary, B. R., Cluzel, N., Cole, M., Cottrell, E., Daly, A., Danyushevsky, L. V., … Zhou, T. (2021). Silicate melt inclusions in the new millennium: A review of recommended practices for preparation, analysis, and data presentation. *Chemical Geology*, *570*, 120145. https://doi.org/10.1016/j.chemgeo.2021.120145

Ruprecht, P., & Plank, T. (2013). Feeding andesitic eruptions with a high-speed connection from the mantle. *Nature*, *500*(7460), 68–72. https://doi.org/10.1038/nature12342

Ruprecht, P., & Welsch, B. (2023). Olivine Exit Interviews—Piecing Together Magmatic Puzzles. *Elements*, *19*(3), 158–164. https://doi.org/10.2138/gselements.19.3.158

Rutherford, M. J. (2008). Magma Ascent Rates. *Reviews in Mineralogy and Geochemistry*, *69*(1), 241–271. https://doi.org/10.2138/rmg.2008.69.7

Rutherford, M. J., & Hill, P. M. (1993). Magma ascent rates from amphibole breakdown: An experimental study applied to the 1980–1986 Mount St. Helens eruptions. *Journal of Geophysical Research: Solid Earth*, *98*(B11), 19667–19685. https://doi.org/10.1029/93JB01613

Ryan, H. F., von Huene, R. E., Wells, R. E., Scholl, D. W., Kirby, S., & Draut, A. E. (2012). *History of earthquakes and tsunamis along the eastern Aleutian-Alaska megathrust, with implications for tsunami hazards in the California Continental Borderland* (Report 1795A; Professional Paper, pp. i–31). USGS Publications Warehouse. https://doi.org/10.3133/pp1795A

Saalfeld, M. A., Myers, M. L., deGraffenried, R., Shea, T., & Waelkens, C. M. (2022). On the rise: Using reentrants to extract magma ascent rates in the Bandelier Tuff caldera complex, New Mexico, USA. *Bulletin of Volcanology*, *84*(1), 4. https://doi.org/10.1007/s00445-021-01518-4

Salas, P., Ruprecht, P., Hernández, L., & Rabbia, O. (2021). Out-of-sequence skeletal growth causing oscillatory zoning in arc olivines. *Nature Communications*, *12*(1), 4069. https://doi.org/10.1038/s41467-021-24275-6

Schwindinger, K. R., & Anderson, A. T. (1989). Synneusis of Kilauea Iki olivines. *Contributions to Mineralogy and Petrology*, *103*(2), 187–198. https://doi.org/10.1007/BF00378504

Shea, T. (2017). Bubble nucleation in magmas: A dominantly heterogeneous process? *Journal of Volcanology and Geothermal Research*, *343*, 155–170. https://doi.org/10.1016/j.jvolgeores.2017.06.025

Shea, T., Costa, F., Krimer, D., & Hammer, J. E. (2015). Accuracy of timescales retrieved from diffusion modeling in olivine: A 3D perspective. *American Mineralogist*, *100*(10), 2026–2042. https://doi.org/10.2138/am-2015-5163

Shea, T., Hammer, J. E., Hellebrand, E., Mourey, A. J., Costa, F., First, E. C., Lynn, K. J., & Melnik, O. (2019). Phosphorus and aluminum zoning in olivine: Contrasting behavior of two nominally incompatible trace elements. *Contributions to Mineralogy and Petrology*, *174*(10), 85. https://doi.org/10.1007/s00410-019-1618-y

Shillington, D. J., Bécel, A., Nedimović, M. R., Kuehn, H., Webb, S. C., Abers, G. A., Keranen, K. M., Li, J., Delescluse, M., & Mattei-Salicrup, G. A. (2015). Link between plate fabric, hydration and subduction zone seismicity in Alaska. *Nature Geoscience*, *8*(12), 961–964. https://doi.org/10.1038/ngeo2586

Singer, B. S., Jicha, B. R., Leeman, W. P., Rogers, N. W., Thirlwall, M. F., Ryan, J., & Nicolaysen, K. E. (2007). Along-strike trace element and isotopic variation in Aleutian Island arc basalt: Subduction melts sediments and dehydrates serpentine. *Journal of Geophysical Research*, *112*(B6), B06206. https://doi.org/10.1029/2006JB004897

Steinberg, G. S., & Babenko, J. I. (1978). Experimental velocity and density determination of volcanic gases during eruption. *Journal of Volcanology and Geothermal Research*, *3*(1–2), 89–98. https://doi.org/10.1016/0377-0273(78)90005-7

Streck, M. J., & Wacaster, S. (2006). Plagioclase and pyroxene hosted melt inclusions in basaltic andesites of the current eruption of Arenal volcano, Costa Rica. *Journal of Volcanology and Geothermal Research*, *157*(1–3), 236–253. https://doi.org/10.1016/j.jvolgeores.2006.03.040

Su, Y., & Huber, C. (2017). The effect of nonlinear decompression history on H_2O/CO_2 vesiculation in rhyolitic magmas. *Journal of Geophysical Research: Solid Earth*, *122*(4), 2712–2723. https://doi.org/10.1002/2016JB013812

Wallace, K. L., Cameron, C. E., Waythomas, C. F., & Perreault, J. M. (2020). *Major-oxide and trace-element geochemical data from the tephra collected on Veniaminof volcano, Alaska* (RDF 2020-17; p. RDF 2020-17). Alaska Division of Geological & Geophysical Surveys. https://doi.org/10.14509/30578

Wallace, P. J., Plank, T., Bodnar, R. J., Gaetani, G. A., & Shea, T. (2021). Olivine-Hosted Melt Inclusions: A Microscopic Perspective on a Complex Magmatic World. *Annual Review of Earth and Planetary Sciences*, *49*(1), 465–494. https://doi.org/10.1146/annurev-earth-082420-060506

Waythomas, C. F., Dietterich, H. R., Tepp, G., Lopez, T. M., & Loewen, M. W. (2022). *The 2018 eruption of Mount Veniaminof, Alaska: U.S. Geological Survey Scientific Investigations Report* (Scientific Investigations Report 2022–5075; The 2018 Eruption of Mount Veniaminof, Alaska, p. 32).

Wei, S. S., Ruprecht, P., Gable, S. L., Huggins, E. G., Ruppert, N., Gao, L., & Zhang, H. (2021). Along-strike variations in intermediate-depth seismicity and arc magmatism along the Alaska Peninsula. *Earth and Planetary Science Letters*, *563*, 116878. https://doi.org/10.1016/j.epsl.2021.116878

Welsch, B., Faure, F., Famin, V., Baronnet, A., & Bachèlery, P. (2013). Dendritic Crystallization: A Single Process for all the Textures of Olivine in Basalts? *Journal of Petrology*, *54*(3), 539–574. https://doi.org/10.1093/petrology/egs077

Welsch, B., Hammer, J., & Hellebrand, E. (2014). Phosphorus zoning reveals dendritic architecture of olivine. *Geology*, *42*(10), 867–870. https://doi.org/10.1130/G35691.1

Wieser, P. E., Vukmanovic, Z., Kilian, R., Ringe, E., Holness, M. B., Maclennan, J., & Edmonds, M. (2019). To sink, swim, twin, or nucleate: A critical appraisal of

crystal aggregation processes. *Geology*, *47*(10), 948–952. https://doi.org/10.1130/G46660.1

Winslow, H., Ruprecht, P., Stelten, M., & Amigo, A. (2020). Evidence for primitive magma storage and eruption following prolonged equilibration in thickened crust. *Bulletin of Volcanology*, *82*(11), 69. https://doi.org/10.1007/s00445-020-01406-3

Yogodzinski, G. M., Brown, S. T., Kelemen, P. B., Vervoort, J. D., Portnyagin, M., Sims, K. W. W., Hoernle, K., Jicha, B. R., & Werner, R. (2015). The Role of Subducted Basalt in the Source of Island Arc Magmas: Evidence from Seafloor Lavas of the Western Aleutians. *Journal of Petrology*, *56*(3), 441–492. https://doi.org/10.1093/petrology/egv006

Zimmer, M. M., Plank, T., Hauri, E. H., Yogodzinski, G. M., Stelling, P., Larsen, J., Singer, B., Jicha, B., Mandeville, C., & Nye, C. J. (2010). The Role of Water in Generating the Calc-alkaline Trend: New Volatile Data for Aleutian Magmas and a New Tholeiitic Index. *Journal of Petrology*, *51*(12), 2411–2444. https://doi.org/10.1093/petrology/egq062

Zuccarello, F., Schiavi, F., & Viccaro, M. (2022). The eruption run-up at Mt. Etna volcano: Constraining magma decompression rates and their relationships with the final eruptive energy. *Earth and Planetary Science Letters*, *597*, 117821. https://doi.org/10.1016/j.epsl.2022.117821

Chapter 4:

Aster, E. M., Wallace, P. J., Moore, L. R., Watkins, J., Gazel, E., & Bodnar, R. J. (2016). Reconstructing CO2 concentrations in basaltic melt inclusions using Raman analysis of vapor bubbles. *Journal of Volcanology and Geothermal Research*, *323*, 148–162. https://doi.org/10.1016/j.jvolgeores.2016.04.028

Bacon, C. R., Sisson, T. W., Calvert, A. T., & Nye, C. J. (2009). *Geologic Map and Eruptive History of Veniaminof Volcano Record Aleutian Arc Processing of Mantle-Derived Melts*. *2009*, V51A-1652.

Bacon, C. R., Sisson, T. W., & Mazdab, F. K. (2007). Young cumulate complex beneath Veniaminof caldera, Aleutian arc, dated by zircon in erupted plutonic blocks. *Geology*, *35*(6), 491. https://doi.org/10.1130/G23446A.1

Barth, A., Newcombe, M., Plank, T., Gonnermann, H., Hajimirza, S., Soto, G. J., Saballos, A., & Hauri, E. (2019). Magma decompression rate correlates with explosivity at basaltic volcanoes—Constraints from water diffusion in olivine. *Journal of Volcanology and Geothermal Research*, *387*, 106664. https://doi.org/10.1016/j.jvolgeores.2019.106664

Barth, A., & Plank, T. (2021). The Ins and Outs of Water in Olivine-Hosted Melt Inclusions: Hygrometer vs. Speedometer. *Frontiers in Earth Science*, *9*, 614004. https://doi.org/10.3389/feart.2021.614004

Batanova, V. G., & Sobolev, A. V. (2023). Development of Reference Materials for Microanalysis in Geosciences: The Case of Olivine MongOL Sh11–2. *Microscopy and Microanalysis*, *29*(Supplement_1), 227–228. https://doi.org/10.1093/micmic/ozad067.101

Batanova, V. G., Thompson, J. M., Danyushevsky, L. V., Portnyagin, M. V., Garbe-Schönberg, D., Hauri, E., Kimura, J., Chang, Q., Senda, R., Goemann, K., Chauvel, C., Campillo, S., Ionov, D. A., & Sobolev, A. V. (2019). New Olivine Reference Material for *In Situ* Microanalysis. *Geostandards and Geoanalytical Research*, *43*(3), 453–473. https://doi.org/10.1111/ggr.12266

Bennington, N., Haney, M., Thurber, C., & Zeng, X. (2018). Inferring Magma Dynamics at Veniaminof Volcano Via Application of Ambient Noise. *Geophysical Research Letters*, *45*(21). https://doi.org/10.1029/2018GL079909

Blatter, D. L., Sisson, T. W., & Hankins, W. B. (2013). Crystallization of oxidized, moderately hydrous arc basalt at mid- to lower-crustal pressures: Implications for andesite genesis. *Contributions to Mineralogy and Petrology*, *166*(3), 861–886. https://doi.org/10.1007/s00410-013-0920-3

Bucholz, C. E., Gaetani, G. A., Behn, M. D., & Shimizu, N. (2013). Post-entrapment modification of volatiles and oxygen fugacity in olivine-hosted melt inclusions. *Earth and Planetary Science Letters*, *374*, 145–155. https://doi.org/10.1016/j.epsl.2013.05.033

Buurman, H., Nye, C. J., West, M. E., & Cameron, C. (2014). Regional controls on volcano seismicity along the Aleutian arc. *Geochemistry, Geophysics, Geosystems*, *15*(4), 1147–1163. https://doi.org/10.1002/2013GC005101

Caricchi, L., Sheldrake, T. E., & Blundy, J. (2018). Modulation of magmatic processes by CO2 flushing. *Earth and Planetary Science Letters*, *491*, 160–171. https://doi.org/10.1016/j.epsl.2018.03.042

Cashman, K. V., & Rust, A. (2016). *Causes and implications of suppressed vesiculation and crystallization in phenocryst embayments*. *2016*, V13G-02.

Castro, J. M., & Dingwell, D. B. (2009). Rapid ascent of rhyolitic magma at Chaitén volcano, Chile. *Nature*, *461*(7265), 780–783. https://doi.org/10.1038/nature08458

Coogan, L. A., Hain, A., Stahl, S., & Chakraborty, S. (2005). Experimental determination of the diffusion coefficient for calcium in olivine between 900°C and 1500°C. *Geochimica et Cosmochimica Acta*, *69*(14), 3683–3694. https://doi.org/10.1016/j.gca.2005.03.002

Cooper, L. B., Ruscitto, D. M., Plank, T., Wallace, P. J., Syracuse, E. M., & Manning, C. E. (2012). Global variations in H_2O/Ce: 1. Slab surface temperatures beneath volcanic arcs. *Geochemistry, Geophysics, Geosystems*, *13*(3), 2011GC003902. https://doi.org/10.1029/2011GC003902

Costa, F., & Morgan, D. (2010). Time Constraints from Chemical Equilibration in Magmatic Crystals. In A. Dosseto, S. P. Turner, & J. A. Van Orman (Eds.),

Timescales of Magmatic Processes (1st ed., pp. 125–159). Wiley. https://doi.org/10.1002/9781444328509.ch7

Couch, S. (2003). The Kinetics of Degassing-Induced Crystallization at Soufriere Hills Volcano, Montserrat. *Journal of Petrology*, *44*(8), 1477–1502. https://doi.org/10.1093/petrology/44.8.1477

Danyushevsky, L. V., McNeill, A. W., & Sobolev, A. V. (2002). Experimental and petrological studies of melt inclusions in phenocrysts from mantle-derived magmas: An overview of techniques, advantages and complications. *Chemical Geology*, *183*(1–4), 5–24. https://doi.org/10.1016/S0009-2541(01)00369-2

Danyushevsky, L. V., & Plechov, P. (2011). Petrolog3: Integrated software for modeling crystallization processes: PETROLOG3. *Geochemistry, Geophysics, Geosystems*, *12*(7), n/a-n/a. https://doi.org/10.1029/2011GC003516

deGraffenried, R. L., & Shea, T. (2021). Using Volatile Element Concentration Profiles in Crystal-Hosted Melt Embayments to Estimate Magma Decompression Rate: Assumptions and Inherited Errors. *Geochemistry, Geophysics, Geosystems*, *22*(5). https://doi.org/10.1029/2021GC009672

DeVitre, C. L., Allison, C. M., & Gazel, E. (2021). A high-precision CO2 densimeter for Raman spectroscopy using a Fluid Density Calibration Apparatus. *Chemical Geology*, *584*, 120522. https://doi.org/10.1016/j.chemgeo.2021.120522

Donovan, J. J., Singer, J. W., & Armstrong, J. T. (2016). A new EPMA method for fast trace element analysis in simple matrices. *American Mineralogist*, *101*(8), 1839–1853. https://doi.org/10.2138/am-2016-5628

Dowty, E. (1980). Synneusis Reconsidered. *Contributions to Mineralogy and Petrology*, *74*(1), 75–84. https://doi.org/10.1007/BF00375491

Esposito, R., Hunter, J., Schiffbauer, J. D., Shimizu, N., & Bodnar, R. J. (2014). An assessment of the reliability of melt inclusions as recorders of the pre-eruptive volatile content of magmas. *American Mineralogist*, *99*(5–6), 976–998. https://doi.org/10.2138/am.2014.4574

Faure, F., & Schiano, P. (2005). Experimental investigation of equilibration conditions during forsterite growth and melt inclusion formation. *Earth and Planetary Science Letters*, *236*(3–4), 882–898. https://doi.org/10.1016/j.epsl.2005.04.050

Ferguson, D. J., Gonnermann, H. M., Ruprecht, P., Plank, T., Hauri, E. H., Houghton, B. F., & Swanson, D. A. (2016). Magma decompression rates during explosive eruptions of Kīlauea volcano, Hawaii, recorded by melt embayments. *Bulletin of Volcanology*, *78*(10), 71. https://doi.org/10.1007/s00445-016-1064-x

Gaetani, G. A., O'Leary, J. A., Shimizu, N., Bucholz, C. E., & Newville, M. (2012). Rapid reequilibration of H2O and oxygen fugacity in olivine-hosted melt inclusions. *Geology*, *40*(10), 915–918. https://doi.org/10.1130/G32992.1

Ghiorso, M. S., & Gualda, G. A. R. (2015). An H2O–CO2 mixed fluid saturation model compatible with rhyolite-MELTS. *Contributions to Mineralogy and Petrology*, *169*(6), 53. https://doi.org/10.1007/s00410-015-1141-8

Giordano, D., Russell, J. K., & Dingwell, D. B. (2008). Viscosity of magmatic liquids: A model. *Earth and Planetary Science Letters*, *271*(1–4), 123–134. https://doi.org/10.1016/j.epsl.2008.03.038

Hauri, E. (2002). SIMS analysis of volatiles in silicate glasses, 2: Isotopes and abundances in Hawaiian melt inclusions. *Chemical Geology*, *183*(1–4), 115–141. https://doi.org/10.1016/S0009-2541(01)00374-6

Hauri, E., Wang, J., Dixon, J. E., King, P. L., Mandeville, C., & Newman, S. (2002). SIMS analysis of volatiles in silicate glasses. *Chemical Geology*, *183*(1–4), 99–114. https://doi.org/10.1016/S0009-2541(01)00375-8

Holness, M. B., Farr, R., & Neufeld, J. A. (2017). Crystal settling and convection in the Shiant Isles Main Sill. *Contributions to Mineralogy and Petrology*, *172*(1), 7. https://doi.org/10.1007/s00410-016-1325-x

Hosseini, B., Myers, M. L., Watkins, J. M., & Harris, M. A. (2023). Are We Recording? Putting Embayment Speedometry to the Test Using High Pressure-Temperature Decompression Experiments. *Geochemistry, Geophysics, Geosystems*, *24*(6), e2022GC010770. https://doi.org/10.1029/2022GC010770

Huggins, E. G., Ruprecht, P., & Ghiorso, M. S. (2021). Using Chemical Affinities to Understand Disequilibrium Textures of Plagioclase Preserved in Magmatic Systems. *Geophysical Research Letters*, *48*(10), e2021GL092884. https://doi.org/10.1029/2021GL092884

Humphreys, M. C. S., Menand, T., Blundy, J. D., & Klimm, K. (2008). Magma ascent rates in explosive eruptions: Constraints from H2O diffusion in melt inclusions. *Earth and Planetary Science Letters*, *270*(1–2), 25–40. https://doi.org/10.1016/j.epsl.2008.02.041

Iacovino, K., & Till, C. B. (2019). DensityX: A program for calculating the densities of magmatic liquids up to 1,627 °C and 30 kbar. *Volcanica*, *2*(1), 1–10. https://doi.org/10.30909/vol.02.01.0110

Jarosewich, E. (2002). Smithsonian Microbeam Standards. *Journal of Research of the National Institute of Standards and Technology*, *107*(6), 681. https://doi.org/10.6028/jres.107.054

Jicha, B. R., & Kay, S. M. (2018). Quantifying arc migration and the role of forearc subduction erosion in the central Aleutians. *Journal of Volcanology and Geothermal Research*, *360*, 84–99. https://doi.org/10.1016/j.jvolgeores.2018.06.016

Jochum, K. P., Stoll, B., Herwig, K., Willbold, M., Hofmann, A. W., Amini, M., Aarburg, S., Abouchami, W., Hellebrand, E., Mocek, B., Raczek, I., Stracke, A., Alard, O., Bouman, C., Becker, S., Dücking, M., Brätz, H., Klemd, R., De Bruin, D., … Woodhead, J. D. (2006). MPI-DING reference glasses for in situ microanalysis:

New reference values for element concentrations and isotope ratios: MPI-DING REFERENCE GLASSES. *Geochemistry, Geophysics, Geosystems*, *7*(2), n/a-n/a. https://doi.org/10.1029/2005GC001060

Jochum, K. P., Weis, U., Stoll, B., Kuzmin, D., Yang, Q., Raczek, I., Jacob, D. E., Stracke, A., Birbaum, K., Frick, D. A., Günther, D., & Enzweiler, J. (2011). Determination of Reference Values for NIST SRM 610–617 Glasses Following ISO Guidelines. *Geostandards and Geoanalytical Research*, *35*(4), 397–429. https://doi.org/10.1111/j.1751-908X.2011.00120.x

Jochum, K. P., Willbold, M., Raczek, I., Stoll, B., & Herwig, K. (2005). Chemical Characterisation of the USGS Reference Glasses GSA-1G, GSC-1G, GSD-1G, GSE-1G, BCR-2G, BHVO-2G and BIR-1G Using EPMA, ID-TIMS, ID-ICP-MS and LA-ICP-MS. *Geostandards and Geoanalytical Research*, *29*(3), 285–302. https://doi.org/10.1111/j.1751-908X.2005.tb00901.x

Jollands, M. C., Muir, J., Padrón-Navarta, J. A., & Demouchy, S. (2022). Modelling hydrogen mobility in forsterite as diffusion coupled to inter-site reaction. *Contributions to Mineralogy and Petrology*, *177*(10), 98. https://doi.org/10.1007/s00410-022-01954-1

Kay, S. M., & Kay, R. W. (1985). Role of crystal cumulates and the oceanic crust in the formation of the lower crust of the Aleutian arc. *Geology*, *13*(7), 461. https://doi.org/10.1130/0091-7613(1985)13<461:ROCCAT>2.0.CO;2

Kay, S. M., Kay, R. W., & Citron, G. P. (1982). Tectonic controls on tholeiitic and calc-alkaline magmatism in the Aleutian Arc. *Journal of Geophysical Research*, *87*(B5), 4051. https://doi.org/10.1029/JB087iB05p04051

Kent, A. J. R. (2008). Melt Inclusions in Basaltic and Related Volcanic Rocks. *Reviews in Mineralogy and Geochemistry*, *69*(1), 273–331. https://doi.org/10.2138/rmg.2008.69.8

Kumamoto, K. M., Warren, J. M., & Hauri, E. H. (2017). New SIMS reference materials for measuring water in upper mantle minerals. *American Mineralogist*, *102*(3), 537–547. https://doi.org/10.2138/am-2017-5863CCBYNCND

Lamadrid, H. M., Moore, L. R., Moncada, D., Rimstidt, J. D., Burruss, R. C., & Bodnar, R. J. (2017). Reassessment of the Raman CO 2 densimeter. *Chemical Geology*, *450*, 210–222. https://doi.org/10.1016/j.chemgeo.2016.12.034

Lambart, S., Hamilton, S., & Lang, O. I. (2022). Compositional variability of San Carlos olivine. *Chemical Geology*, *605*, 120968. https://doi.org/10.1016/j.chemgeo.2022.120968

Larsen, J. F. (2016). Unraveling the diversity in arc volcanic eruption styles: Examples from the Aleutian volcanic arc, Alaska. *Journal of Volcanology and Geothermal Research*, *327*, 643–668. https://doi.org/10.1016/j.jvolgeores.2016.09.008

Li, Y., Gregg, P. M., Lu, Z., & Wang, J. (2022). *Investigations of open magma system behavior at Veniaminof Volcano, Alaska*. *2022*, V32F-0125.

Liu, Y., Anderson, A. T., & Wilson, C. J. N. (2007). Melt pockets in phenocrysts and decompression rates of silicic magmas before fragmentation. *Journal of Geophysical Research: Solid Earth*, *112*(B6), 2006JB004500. https://doi.org/10.1029/2006JB004500

Lloyd, A. S., Plank, T., Ruprecht, P., Hauri, E. H., & Rose, W. (2013). Volatile loss from melt inclusions in pyroclasts of differing sizes. *Contributions to Mineralogy and Petrology*, *165*(1), 129–153. https://doi.org/10.1007/s00410-012-0800-2

Lloyd, A. S., Ruprecht, P., Hauri, E. H., Rose, W., Gonnermann, H. M., & Plank, T. (2014). NanoSIMS results from olivine-hosted melt embayments: Magma ascent rate during explosive basaltic eruptions. *Journal of Volcanology and Geothermal Research*, *283*, 1–18. https://doi.org/10.1016/j.jvolgeores.2014.06.002

Loewen, M. W., Dietterich, H. R., Graham, N., & Izbekov, P. (2021). Evolution in eruptive style of the 2018 eruption of Veniaminof volcano, Alaska, reflected in groundmass textures and remote sensing. *Bulletin of Volcanology*, *83*(11), 72. https://doi.org/10.1007/s00445-021-01489-6

Lowenstern, J. B., & Thompson, J. F. H. (n.d.). Applications of silicate-melt inclusions to the study of magmatic volatiles. *Magmas, Fluids and Ore Deposits*, *23*, 71–99.

Lubbers, J., Kent, A., Meisenheimer, D., & Wildenschild, D. (2023). 3D zoning of barium in alkali feldspar. *American Mineralogist*, *108*(2), 297–311. https://doi.org/10.2138/am-2022-8139

Lynn, K. J., & Desmither, L. (2023). *Creating Oriented and Precisely Sectioned Mineral Mounts for In Situ Chemical Analyses—An Example Using Olivine for Diffusion Chronometry Studies* (Techniques and Methods book 5, chap. D5; Techniques and Methods, p. 36 p). U.S. Geological Survey.

Mangan, M., & Sisson, T. (2000). Delayed, disequilibrium degassing in rhyolite magma: Decompression experiments and implications for explosive volcanism. *Earth and Planetary Science Letters*, *183*(3–4), 441–455. https://doi.org/10.1016/S0012-821X(00)00299-5

Martel, C., & Schmidt, B. C. (2003). Decompression experiments as an insight into ascent rates of silicic magmas. *Contributions to Mineralogy and Petrology*, *144*(4), 397–415. https://doi.org/10.1007/s00410-002-0404-3

McIntire, M. Z., Bergantz, G. W., & Schleicher, J. M. (2019). On the hydrodynamics of crystal clustering. *Philosophical Transactions of the Royal Society A: Mathematical, Physical and Engineering Sciences*, *377*(2139), 20180015. https://doi.org/10.1098/rsta.2018.0015

Melt Inclusion Study of the Embryonic Porphyry Copper System at White Island, New Zealand. (2005). In S. F. Simmons & I. Graham, *Volcanic, Geothermal, and Ore-Forming Fluids* (pp. 41–59). Society of Economic Geologists. https://doi.org/10.5382/SP.10.03

Moore, L. R., & Bodnar, R. J. (2019). A pedagogical approach to estimating the CO_2 budget of magmas. *Journal of the Geological Society*, *176*(2), 398–407. https://doi.org/10.1144/jgs2018-094

Moore, L. R., Gazel, E., Tuohy, R., Lloyd, A. S., Esposito, R., Steele-MacInnis, M., Hauri, E. H., Wallace, P. J., Plank, T., & Bodnar, R. J. (2015). Bubbles matter: An assessment of the contribution of vapor bubbles to melt inclusion volatile budgets. *American Mineralogist*, *100*(4), 806–823. https://doi.org/10.2138/am-2015-5036

Mourey, A. J., & Shea, T. (2019). Forming Olivine Phenocrysts in Basalt: A 3D Characterization of Growth Rates in Laboratory Experiments. *Frontiers in Earth Science*, *7*, 300. https://doi.org/10.3389/feart.2019.00300

Moussallam, Y., Rose-Koga, E. F., Koga, K. T., Médard, E., Bani, P., Devidal, J.-L., & Tari, D. (2019). Fast ascent rate during the 2017–2018 Plinian eruption of Ambae (Aoba) volcano: A petrological investigation. *Contributions to Mineralogy and Petrology*, *174*(11), 90. https://doi.org/10.1007/s00410-019-1625-z

Newcombe, M. E., Fabbrizio, A., Zhang, Y., Ma, C., Le Voyer, M., Guan, Y., Eiler, J. M., Saal, A. E., & Stolper, E. M. (2014). Chemical zonation in olivine-hosted melt inclusions. *Contributions to Mineralogy and Petrology*, *168*(1), 1030. https://doi.org/10.1007/s00410-014-1030-6

Newcombe, M. E., Plank, T., Barth, A., Asimow, P. D., & Hauri, E. (2020). Water-in-olivine magma ascent chronometry: Every crystal is a clock. *Journal of Volcanology and Geothermal Research*, *398*, 106872. https://doi.org/10.1016/j.jvolgeores.2020.106872

Oeser, M., Ruprecht, P., & Weyer, S. (2018). Combined Fe-Mg chemical and isotopic zoning in olivine constraining magma mixing-to-eruption timescales for the continental arc volcano Irazú (Costa Rica) and Cr diffusion in olivine. *American Mineralogist*, *103*(4), 582–599. https://doi.org/10.2138/am-2018-6258

Pesicek, J. D., Wellik, J. J., Prejean, S. G., & Ogburn, S. E. (2018). Prevalence of Seismic Rate Anomalies Preceding Volcanic Eruptions in Alaska. *Frontiers in Earth Science*, *6*, 100. https://doi.org/10.3389/feart.2018.00100

Plank, T. (2005). Constraints from Thorium/Lanthanum on Sediment Recycling at Subduction Zones and the Evolution of the Continents. *Journal of Petrology*, *46*(5), 921–944. https://doi.org/10.1093/petrology/egi005

Plank, T., Kelley, K. A., Zimmer, M. M., Hauri, E. H., & Wallace, P. J. (2013). Why do mafic arc magmas contain ~4wt% water on average? *Earth and Planetary Science Letters*, *364*, 168–179. https://doi.org/10.1016/j.epsl.2012.11.044

Portnyagin, M., Almeev, R., Matveev, S., & Holtz, F. (2008). Experimental evidence for rapid water exchange between melt inclusions in olivine and host magma. *Earth and Planetary Science Letters*, *272*(3–4), 541–552. https://doi.org/10.1016/j.epsl.2008.05.020

Portnyagin, M., Mironov, N., Botcharnikov, R., Gurenko, A., Almeev, R. R., Luft, C., & Holtz, F. (2019). Dehydration of melt inclusions in olivine and implications for the origin of silica-undersaturated island-arc melts. *Earth and Planetary Science Letters*, *517*, 95–105. https://doi.org/10.1016/j.epsl.2019.04.021

Putirka, K. D. (2008). Thermometers and Barometers for Volcanic Systems. *Reviews in Mineralogy and Geochemistry*, *69*(1), 61–120. https://doi.org/10.2138/rmg.2008.69.3

Qin, Z., Fangqiong, L., & Anderson, A. (1992). Diffusive reequilibration of melt and fluid inclusions. *American Mineralogist*, *77*(5–6), 565–576.

Rasmussen, D. J., Plank, T. A., Roman, D. C., & Zimmer, M. M. (2022). Magmatic water content controls the pre-eruptive depth of arc magmas. *Science*, *375*(6585), 1169–1172. https://doi.org/10.1126/science.abm5174

Rasmussen, D. J., Plank, T. A., Wallace, P. J., Newcombe, M. E., & Lowenstern, J. B. (2020). Vapor-bubble growth in olivine-hosted melt inclusions. *American Mineralogist*, *105*(12), 1898–1919. https://doi.org/10.2138/am-2020-7377

Roeder, E. (1979). Origin and significance of magmatic inclusions. Bulletin de Mineralogie. *Bulletin de Mineralogie*, *102*(5), 487–510.

Rose-Koga, E. F., Bouvier, A.-S., Gaetani, G. A., Wallace, P. J., Allison, C. M., Andrys, J. A., Angeles De La Torre, C. A., Barth, A., Bodnar, R. J., Bracco Gartner, A. J. J., Butters, D., Castillejo, A., Chilson-Parks, B., Choudhary, B. R., Cluzel, N., Cole, M., Cottrell, E., Daly, A., Danyushevsky, L. V., … Zhou, T. (2021). Silicate melt inclusions in the new millennium: A review of recommended practices for preparation, analysis, and data presentation. *Chemical Geology*, *570*, 120145. https://doi.org/10.1016/j.chemgeo.2021.120145

Ruprecht, P., & Plank, T. (2013). Feeding andesitic eruptions with a high-speed connection from the mantle. *Nature*, *500*(7460), 68–72. https://doi.org/10.1038/nature12342

Ruprecht, P., & Welsch, B. (2023). Olivine Exit Interviews—Piecing Together Magmatic Puzzles. *Elements*, *19*(3), 158–164. https://doi.org/10.2138/gselements.19.3.158

Rutherford, M. J. (2008). Magma Ascent Rates. *Reviews in Mineralogy and Geochemistry*, *69*(1), 241–271. https://doi.org/10.2138/rmg.2008.69.7

Rutherford, M. J., & Hill, P. M. (1993). Magma ascent rates from amphibole breakdown: An experimental study applied to the 1980–1986 Mount St. Helens eruptions. *Journal of Geophysical Research: Solid Earth*, *98*(B11), 19667–19685. https://doi.org/10.1029/93JB01613

Ryan, H. F., von Huene, R. E., Wells, R. E., Scholl, D. W., Kirby, S., & Draut, A. E. (2012). *History of earthquakes and tsunamis along the eastern Aleutian-Alaska megathrust, with implications for tsunami hazards in the California Continental Borderland* (Report 1795A; Professional Paper, pp. i–31). USGS Publications Warehouse. https://doi.org/10.3133/pp1795A

Saalfeld, M. A., Myers, M. L., deGraffenried, R., Shea, T., & Waelkens, C. M. (2022). On the rise: Using reentrants to extract magma ascent rates in the Bandelier Tuff caldera complex, New Mexico, USA. *Bulletin of Volcanology*, *84*(1), 4. https://doi.org/10.1007/s00445-021-01518-4

Salas, P., Ruprecht, P., Hernández, L., & Rabbia, O. (2021). Out-of-sequence skeletal growth causing oscillatory zoning in arc olivines. *Nature Communications*, *12*(1), 4069. https://doi.org/10.1038/s41467-021-24275-6

Schwindinger, K. R., & Anderson, A. T. (1989). Synneusis of Kilauea Iki olivines. *Contributions to Mineralogy and Petrology*, *103*(2), 187–198. https://doi.org/10.1007/BF00378504

Shea, T. (2017). Bubble nucleation in magmas: A dominantly heterogeneous process? *Journal of Volcanology and Geothermal Research*, *343*, 155–170. https://doi.org/10.1016/j.jvolgeores.2017.06.025

Shea, T., Costa, F., Krimer, D., & Hammer, J. E. (2015). Accuracy of timescales retrieved from diffusion modeling in olivine: A 3D perspective. *American Mineralogist*, *100*(10), 2026–2042. https://doi.org/10.2138/am-2015-5163

Shea, T., Hammer, J. E., Hellebrand, E., Mourey, A. J., Costa, F., First, E. C., Lynn, K. J., & Melnik, O. (2019). Phosphorus and aluminum zoning in olivine: Contrasting behavior of two nominally incompatible trace elements. *Contributions to Mineralogy and Petrology*, *174*(10), 85. https://doi.org/10.1007/s00410-019-1618-y

Shillington, D. J., Bécel, A., Nedimović, M. R., Kuehn, H., Webb, S. C., Abers, G. A., Keranen, K. M., Li, J., Delescluse, M., & Mattei-Salicrup, G. A. (2015). Link between plate fabric, hydration and subduction zone seismicity in Alaska. *Nature Geoscience*, *8*(12), 961–964. https://doi.org/10.1038/ngeo2586

Singer, B. S., Jicha, B. R., Leeman, W. P., Rogers, N. W., Thirlwall, M. F., Ryan, J., & Nicolaysen, K. E. (2007). Along-strike trace element and isotopic variation in Aleutian Island arc basalt: Subduction melts sediments and dehydrates serpentine. *Journal of Geophysical Research*, *112*(B6), B06206. https://doi.org/10.1029/2006JB004897

Steinberg, G. S., & Babenko, J. I. (1978). Experimental velocity and density determination of volcanic gases during eruption. *Journal of Volcanology and Geothermal Research*, *3*(1–2), 89–98. https://doi.org/10.1016/0377-0273(78)90005-7

Streck, M. J., & Wacaster, S. (2006). Plagioclase and pyroxene hosted melt inclusions in basaltic andesites of the current eruption of Arenal volcano, Costa Rica. *Journal of Volcanology and Geothermal Research*, *157*(1–3), 236–253. https://doi.org/10.1016/j.jvolgeores.2006.03.040

Su, Y., & Huber, C. (2017). The effect of nonlinear decompression history on H_2O/CO_2 vesiculation in rhyolitic magmas. *Journal of Geophysical Research: Solid Earth*, *122*(4), 2712–2723. https://doi.org/10.1002/2016JB013812

Wallace, K. L., Cameron, C. E., Waythomas, C. F., & Perreault, J. M. (2020). *Major-oxide and trace-element geochemical data from the tephra collected on Veniaminof volcano, Alaska* (RDF 2020-17; p. RDF 2020-17). Alaska Division of Geological & Geophysical Surveys. https://doi.org/10.14509/30578

Wallace, P. J., Plank, T., Bodnar, R. J., Gaetani, G. A., & Shea, T. (2021). Olivine-Hosted Melt Inclusions: A Microscopic Perspective on a Complex Magmatic World. *Annual Review of Earth and Planetary Sciences*, *49*(1), 465–494. https://doi.org/10.1146/annurev-earth-082420-060506

Waythomas, C. F., Dietterich, H. R., Tepp, G., Lopez, T. M., & Loewen, M. W. (2022). *The 2018 eruption of Mount Veniaminof, Alaska: U.S. Geological Survey Scientific Investigations Report* (Scientific Investigations Report 2022–5075; The 2018 Eruption of Mount Veniaminof, Alaska, p. 32).

Wei, S. S., Ruprecht, P., Gable, S. L., Huggins, E. G., Ruppert, N., Gao, L., & Zhang, H. (2021). Along-strike variations in intermediate-depth seismicity and arc magmatism along the Alaska Peninsula. *Earth and Planetary Science Letters*, *563*, 116878. https://doi.org/10.1016/j.epsl.2021.116878

Welsch, B., Faure, F., Famin, V., Baronnet, A., & Bachèlery, P. (2013). Dendritic Crystallization: A Single Process for all the Textures of Olivine in Basalts? *Journal of Petrology*, *54*(3), 539–574. https://doi.org/10.1093/petrology/egs077

Welsch, B., Hammer, J., & Hellebrand, E. (2014). Phosphorus zoning reveals dendritic architecture of olivine. *Geology*, *42*(10), 867–870. https://doi.org/10.1130/G35691.1

Wieser, P. E., Vukmanovic, Z., Kilian, R., Ringe, E., Holness, M. B., Maclennan, J., & Edmonds, M. (2019). To sink, swim, twin, or nucleate: A critical appraisal of crystal aggregation processes. *Geology*, *47*(10), 948–952. https://doi.org/10.1130/G46660.1

Winslow, H., Ruprecht, P., Stelten, M., & Amigo, A. (2020). Evidence for primitive magma storage and eruption following prolonged equilibration in thickened crust. *Bulletin of Volcanology*, *82*(11), 69. https://doi.org/10.1007/s00445-020-01406-3

Yogodzinski, G. M., Brown, S. T., Kelemen, P. B., Vervoort, J. D., Portnyagin, M., Sims, K. W. W., Hoernle, K., Jicha, B. R., & Werner, R. (2015). The Role of Subducted Basalt in the Source of Island Arc Magmas: Evidence from Seafloor Lavas of the Western Aleutians. *Journal of Petrology*, *56*(3), 441–492. https://doi.org/10.1093/petrology/egv006

Zimmer, M. M., Plank, T., Hauri, E. H., Yogodzinski, G. M., Stelling, P., Larsen, J., Singer, B., Jicha, B., Mandeville, C., & Nye, C. J. (2010). The Role of Water in Generating the Calc-alkaline Trend: New Volatile Data for Aleutian Magmas and a New Tholeiitic Index. *Journal of Petrology*, *51*(12), 2411–2444. https://doi.org/10.1093/petrology/egq062

Zuccarello, F., Schiavi, F., & Viccaro, M. (2022). The eruption run-up at Mt. Etna volcano: Constraining magma decompression rates and their relationships with

the final eruptive energy. *Earth and Planetary Science Letters*, *597*, 117821. https://doi.org/10.1016/j.epsl.2022.117821

Zhu, L., Kolesov, I., Gao, Y., Kikinis, R., & Tannenbaum, A. (2014, September). An effective interactive medical image segmentation method using fast growcut. In *MICCAI workshop on interactive medical image computing*.